



HAL
open science

Phenomenology of active particles with finite and discrete internal states : an individual and collective study

Luis Alberto Gómez Nava

► **To cite this version:**

Luis Alberto Gómez Nava. Phenomenology of active particles with finite and discrete internal states : an individual and collective study. Physics [physics]. COMUE Université Côte d'Azur (2015 - 2019), 2018. English. NNT : 2018AZUR4080 . tel-02070937

HAL Id: tel-02070937

<https://theses.hal.science/tel-02070937>

Submitted on 18 Mar 2019

HAL is a multi-disciplinary open access archive for the deposit and dissemination of scientific research documents, whether they are published or not. The documents may come from teaching and research institutions in France or abroad, or from public or private research centers.

L'archive ouverte pluridisciplinaire **HAL**, est destinée au dépôt et à la diffusion de documents scientifiques de niveau recherche, publiés ou non, émanant des établissements d'enseignement et de recherche français ou étrangers, des laboratoires publics ou privés.

THÈSE DE DOCTORAT

Phénoménologie de particules
actives à états internes finis et
discrets : une étude individuelle et
collective

Luis Alberto GÓMEZ NAVA

Laboratoire Jean Alexandre Dieudonné

**Présentée en vue de l'obtention
du grade de docteur en physique
d'Université Côte d'Azur.**

Dirigée par : Fernando PERUANI.
Soutenue le : 5 novembre 2018.

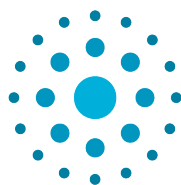


CONACYT

Consejo Nacional de Ciencia y Tecnología

Devant le jury, composé de :

- Richard BON, Maître de Conférences, Université Toulouse III, Paul Sabatier.
- Richard FOURNIER, Professeur, Université Toulouse III, Paul Sabatier.
- Thierry GOUDON, Directeur de recherche, Université Côte d'Azur.
- José HALLOY, Professeur, Université Paris Diderot.
- Fernando PERUANI, Maître de Conférences, Université Côte d'Azur.



École Doctorale Sciences Fondamentales et Appliquées
Laboratoire Jean Alexandre Dieudonné

Thèse de doctorat

Présentée en vue de l'obtention du
grade de docteur en Physique
de
Université Côte d'Azur

par

Luis Alberto GÓMEZ NAVA

PHÉNOMÉNOLOGIE DE PARTICULES ACTIVES À ÉTATS
INTERNES FINIS ET DISCRETS : UNE ÉTUDE INDIVIDUELLE ET
COLLECTIVE

PHENOMENOLOGY OF ACTIVE PARTICLES WITH FINITE AND
DISCRETE INTERNAL STATES : AN INDIVIDUAL AND
COLLECTIVE STUDY

Dirigée par Fernando PERUANI, Maître de conférences, Université Côte d'Azur.

Soutenue le 5 novembre 2018.

Devant le jury composé de :

Richard BON	Maître de conférences, Université Toulouse III, Paul Sabatier	Examineur
Richard FOURNIER	Professeur, Université Toulouse III, Paul Sabatier	Rapporteur
Thierry GOUDON	Directeur de recherche, Université Côte d'Azur	Examineur
José HALLOY	Professeur, Université Paris Diderot	Rapporteur
Fernando PERUANI	Maître de conférences, Université Côte d'Azur	Directeur de thèse

Résumé. Dans cette thèse, nous présentons un cadre théorique pour étudier les systèmes de particules actives fonctionnant avec une quantité discrète d'états internes qui contrôlent le comportement externe de ces objets. Les concepts théoriques développés dans cette thèse sont introduits afin de comprendre un grand nombre de systèmes biologiques multi-agents dont les individus présentent différents types de comportements se succédant au cours du temps. Par construction, le modèle théorique suppose que l'observateur extérieur a accès uniquement au comportement visible des individus, et non pas à leurs états internes. C'est seulement après une étude détaillée de la dynamique comportementale que l'existence de ces états internes devient évidente. Cette analyse est cruciale pour pouvoir associer les comportements observés expérimentalement avec un ou plusieurs états internes du modèle. Cette association entre les états et les comportements doit être faite selon les observations et la phénoménologie du système biologique faisant l'objet de l'étude. Les scénarios qui peuvent être observés en utilisant notre modèle théorique sont déterminés par la conception du mécanisme interne des individus (nombre d'états internes, taux de transition, etc...) et seront de nature markovienne par construction. Tous les travaux expérimentaux et théoriques contenus dans cette thèse démontrent que notre modèle est approprié pour décrire des systèmes réels montrant des comportements intermittents individuels ou collectifs. Ce nouveau cadre théorique pour des particules actives avec états internes, introduit ici, est encore en développement et nous sommes convaincus qu'il peut potentiellement ouvrir de nouvelles branches de recherche à l'interface entre la physique, la biologie et les mathématiques.

Mots-clés: matière active, comportements intermittents, états internes, systèmes biologiques, processus markoviens, phénomènes collectifs, systèmes synchronisés.

Abstract. In this thesis we introduce a theoretical framework to understand collections of active particles that operate with a finite number of discrete internal states that control the external behavior of these entities. The theoretical concepts developed in this thesis are conceived to understand the large number of existing multiagent biological systems where the individuals display distinct behavioral phases that alternate with each other. By construction, the premise of our theoretical model is that an external observer has access only to the external behavior of the individuals, but not to their internal state. It is only after careful examination of the behavioral dynamics that the existence of these internal states becomes evident. This analysis is key to be able to associate the experimentally observed behaviors of individuals with one or many internal states of the model. This association between states and behaviors should be done accordingly to the observations and the phenomenology displayed by the biological system that is being the subject of study. The possible scenarios that can be observed using our theoretical model are determined by the design of the internal mechanism of the individuals (number of internal states, transition rates, etc...) and will be of markovian nature by construction. All the experimental and theoretical work contained in this thesis is evidence that our model is suitable to be used to describe real-life systems showing individual or collective intermittent behaviors. This here-introduced new framework of active particles with internal states is still in development and we are convinced that it can potentially open new branches of research at the interface between physics, biology and mathematics.

Keywords: active matter, intermittent behaviors, internal states, biological systems, markov processes, collective phenomena, synchronized systems.

*“Los relojes no se inventaron para dar la hora,
para empezar, porque las horas se inventaron
después que los relojes, y porque la gente en la
historia no le interesa saber qué horas son, ya
que no estaban contratados por horas ni tenían
que producir a contrareloj ni andar apurados.”*

La Forma de los Miércoles
Pablo Fernández Christlieb

Acknowledgements

First of all, I would like to thank my PhD advisor Fernando Peruani: your unique way of perceiving science and life in general has been a constant motivation for me. Your wisdom and advice have helped me to build solid foundations for my academic career and will certainly guide me in the future. Having chosen to come to Nice to make the PhD thesis has been one of the best decisions I have made in my life. Thank you for being a leading example and the best advisor. ¡Hasta la victoria siempre!

I would also like to thank the members of my jury: Richard Bon, Richard Fournier, Thierry Goudon and José Halloy. Your comments and questions helped me to improve the present work and clarify the concepts in this thesis.

Very special thanks to the members of my working team (known as “the ducklings”): Robert Großmann, Emiliano Perez Ipiña, Stefan Otte, Hadrien Gascuel, Diego Bengochea and Vincent Ravera. Thank you for sharing lunch-time, dinners (at Borriglione or Tapa Loca), barbecues, ski trips, bike rides, conferences, etc . . . I always found support, advice and a lot of help with each one of you. Robert: thank you very much for your patience, for being always in the mood to help me (even if the questions were very simple) and for your friendship. Emiliano: thank you also for the help and the good mood. You are amazing at programming and a very good teacher regarding mate preparation. Stefan: thank you for being there for me at the beginning of the PhD. I hope some day I’ll follow your advice and learn Python and then conquer the world with that. Hadrien: thank you for your good humor and your help with French translations. I hope one day we can share a cup of coffee or a beer. Diego: thank you very much for your help and trust. I loved when you shared me your stories of your trip in Mexico because I perceived that you love many things of my country and it made me very happy. I hope to visit Uruguay one day. Vincent: thank you for your help to improve my French and for being a good friend.

I would also like to acknowledge my former advisors and collaborators in Mexico, Francisco Javier Sevilla and Eugenio Ley Koo from the Physics Institute of the Universidad Nacional Autónoma de México. You helped me in several ways in the early stages of my academic training and guided me wisely.

I would also like to thank my family: Mireya, Matilde and Luis Manuel. Thank you for always being there for me, in good and in bad times. Your advice and your ability to listen give me the strength to follow my dreams. I hope to return one day to our beloved Milpa Alta and see how much it has changed. I’ll love you three forever. Thank you for supporting me. A very big “thank you” to the other members of my Gómez and

Nava families: abuelita Lucha, abuelito Carlos, abuelita Pachita, abuelito Bulmaro, tías Rosita, Conchita, Mai, Rosalba, Lucy, tíos Santiago, Arturo, Andrés, my cousins Adriana, Quecha, Kika, Fernando, Vladimir, Marco, Nancy and Andy. Thank you all for all that you have done for me.

I want to thank also my Italian family: Francesca, Giuliana, Alberto, Letizia, Sara, Sabrina, Marcello, Noemi, Emanuele, Celestina, Caterina, Gianni and Ettore. You welcomed me everytime I visited you in the beautiful Esenta and made me feel loved and part of your family. I'll always be thankful for that.

I would also like to thank “the old” PhD friends for offering me your friendship and a warm welcome when I arrived to the lab, without speaking any French at all. Nathalie: ¡muchas gracias por todo mi amiga Nathalie! ¡Tienes una familia muy bonita! Espero que Maeva, Thibaut y tú sean muy felices. Mélisande: thank you for welcoming me to the lab from the very beginning. Thank you also for introducing us to the crossword tradition. Always remember: “nosotros nos vámonos a trabajar a nuestros trabajos”. Julien: thank you for your friendship, advice and help. I always remember how thoughtfully you taught me to improve my French. Don't tell anybody, but you are still le plus beaugosse du monde ♡♡!!. David Métivier: thanks for being the best office mate (together with Samira). I enjoyed to play freezbee with you and football also. I'll never forget your birthday, because is the same as mine!! ☺ ¡Muchas gracias compa por la ayuda y tu gran amistad! Te quiero mucho. Charles: amigo Charles, muchas gracias por ser un increíble coloque. I enjoyed organizing nice parties at the villa (in the garden), playing bubble foot, watching movies in my room with the projector, having dinner at the beach and also I enjoyed how we shared our love to music. You are a very good friend that helped me a lot. You were there in good times and bad times. ¡Muchas gracias por toda la ayuda! Eduard: thank you a lot for your help and advice, and for bringing the lab some of your style. Kate: thank you for your friendship and for the nice coffee cup with sheep. I use it often because I like it a lot.

Many thanks also to “the new” PhD friends. Pupi: you are a very special person for me, thank you for being one of my best friends in Nice, for the support, the laughs, the dinners, the trips, and above all for sharing with me politically incorrect memes. Thank you for welcoming us always at your place and for being that person in which I could trust no matter what, and also eat some 100% tacos. ¡Gaviota! Victor: thank you a lot for the support with French translations, with the organization of several things, for the many trips, dinners, and for being one of the most polite, caring and good persons I know. Thank you for your trust my friend. You are an amazing volleyball player, scientist and person. I will miss supporting you in your volleyball matches. Laurence: thank you for all the nice moments, and also for your friendship. I loved when we spent time together and the parties we shared. In particular Samira's party at your place and the 90's party at my place. Your costume of the ninja turtles was amazing!! Reine: thanks for being a very good friend. I enjoyed a lot when you brought your karaoke to my place and we sang for long time. I will always remember with joy the basketball matches you organized. Samira & Ludo: thank you guys for all the laughs, for the jokes and above all for introducing me to the legendary “l'homme chèvre”. My life changed for good after that. I'll always remember the very nice cake we did together based on the movie “IT”

(Georgie!!!). I'll miss you a lot. I MUST highlight that Ludo is the person with the best musical taste I know. I hope one day we can go together to a concert of The Offspring, Blink 182 or another nice band. And Samira, thanks for teaching me the best French expression I know: "J'ai les dents du fond qui baignent". Byron: thank you very much for your friendship. Marcella and me spent several good moments with you and Cata. Thanks for being there. I hope one day we will visit Costa Rica and meet again. Julie: thank you for your disposition to answer all my questions, even if they were very stupid ones. You helped me and all the others all the time, I appreciate that a lot. I wish all the best for you in your new job. Alexis Gilles and Mehdi (my dear roommates): it has been a pleasure to share with you our amazing villa (even if crazy almighty Desmet believes everything belongs to him). Every day when I arrived home, it was very nice to know that you were there. You gave a nice spark of energy to the ambience at our place. I had also the chance to meet your families, and they are amazing. Thank you for all the nice moments. Alexis Loyer: thank you for being always there for me when I required any kind of help. You are an amazing cook, I'll miss to taste all the dishes you make. Huda: thanks for being a very kind person with me, always very polite and nice office neighbour. Eliot: thanks for teaching us how people dance here in France. I enjoyed to make jokes with you and also to be (for short time) window neighbours. Armand: thank you for your patience when teaching me to play card and video games. I enjoyed learning from you. Jonathan: thanks for sharing many lunch times with me, as well as some parties. You have a beautiful family.

During this time in France, I had also a lot of support of my dear Mexican friends. Corro: thank you for being such a nice and good friend. I loved the times you visited me in Nice and I deeply regret not being able to be at your thesis defense. We have shared a lot of stories together since we met in the first semesters at the Science Faculty. I treasure you as one of my favourite persons in the world. We still have many more things to share my friend. Rebeca: my dear "mana". Thanks for always being such a good friend. Also, as I said before with Corro, I loved when you visited me in Nice. I will always thank you for preparing me the most tasty frijoles ever!! I really missed them. ¡Te quiero mucho mana! Iker: although being far away, I always felt that I could trust you in good and bad times. Thanks for the help, your advice (including the thesis comments) and the jokes. Also, thanks for the nice trip to Italy and the many adventures we have had since long time. I love you my friend. Citlali: ¡muchas gracias compañera! Thanks for the dances, the support and for having shared with me a lot of incredible moments. I will remember particularly our trip to Iceland. What an amazing trip!! One of the best I've had. Arturo: "¡Muchas gracias mano por el apoyo y por los consejos!". I hope we can meet soon so I can continue to teach you and Omar how to play Fifa. I miss you my friend. Omar and Talia (not Thalia): thank you for visiting me in Nice and for hosting me in Dresden. I enjoyed assisting to your presentations at the DPG 2018 of Berlin. I hope that in the future we can return to the amazing "Fonda las Carmelitas" together with Arturo and Rebe. David Bernal: thanks for receiving us at your place in Amsterdam. You are a very special person for me and I always enjoyed when we lost control and began to say nonsense (like when we talked about "tabiques"). I miss you a lot my friend. Corinto: thanks for visiting me in Nice and for your support. You are always a very relaxed person and I enjoy to spend time with you. I hope to visit you in London soon. Irene: thanks for hosting me at your place in Bonn. I enjoyed a lot that time when I visited you, specially

when we visited the Tim Burton exposition. You are a very nice person with me, always with a smile and good mood. Lau: I enjoyed a lot when I saw you in Amsterdam, at your son's house (David). I remember always our stories when we were young at the Facultad de Ciencias with our friends at "el pulpo". ¡¡Te quiero mucho Laurita!!

A very special and huge "thank you" to my friends at the RU (university restaurant), particularly to my dear friend Éric. You welcomed us most of the days with a smile and feeded our bodies with such an amazing food. Without any doubt, the best restaurant in the whole France!!

I would like also to thank the people that help us everyday at the lab with small or big problems, especially to Julia Blondel, Jean-Marc Lacroix, Roland, Clara and Valerie.

Finally, I would like to dedicate my thesis to the most important person to me: Marcella. Thank you for being there by my side everyday, day and night. I found in you my biggest support of all, my pilar to continue and my motivation to become a better person. There is no other place where I feel better at home than by your side. Thank you for changing my life since the first day that I met you, in front of the door of our lab in Nice. I love you.

Contents

1	The idea of individual internal states	13
1.1	Internal Control System (ICS)	13
2	Experimental evidence of internal states in biological systems: from bacteria to sheep	19
2.1	<i>Pseudomonas Putida</i>	20
2.1.1	Using a model of two internal states	20
2.2	Small groups of gregarious animals	22
2.2.1	Analysis of individual signals	23
2.2.2	Individual characteristic times	24
2.2.3	Interpretation of the three states	26
2.2.4	Functional form of the transition rates	27
2.3	Summary & perspectives	30
3	Individual Navigation Strategies	31
3.1	Introducing the Markovian robots	32
3.2	Markovian robots with different NCS's	35
3.2.1	Spatial dynamics	35
3.2.2	A didactic introduction	36
3.2.3	Effective Langevin dynamics	36
3.2.4	NCS motif 1: up- & downgradient motion	38
3.2.5	NCS motif 2: adaptation	40
3.3	Performing complex tasks	41
3.4	Two & three-dimensional systems	43
3.5	Tests with a real robot	49
3.6	Summary & perspectives	52
4	Intermittent Collective Behavior: a three state story	53
4.1	The three state model	54
4.2	Mean field	55
4.2.1	Recruiting term	55
4.2.2	Inhibitory term	59
4.2.3	Parameter diagram using both terms	62
4.3	Stochastic system	64
4.3.1	The Collective Clock Approximation	66
4.3.2	The Metaparticle Clock Approximation	68
4.4	Numerical comparison of CCA and MCA with IBM simulations	70

4.5	Summary & perspectives	71
5	Collective transport of particles with three internal states	73
5.1	Average transport properties	75
5.1.1	Average mean squared displacement $\langle \mathbf{x}_{cm}^2(t) \rangle$	75
5.1.2	Average dispersion around the center of mass $\langle \sigma_g^2 \rangle$	78
5.2	Discussion and results	81
5.3	Summary & perspectives	84
6	Conclusions	85
A	Experimental Methods	87
A.1	<i>Pseudomonas Putida</i>	87
A.1.1	Microfluidics and imaging	87
A.1.2	Filtering and smoothing	88
A.1.3	Run-and-tumble recognition	88
A.2	Merino sheep	88
A.2.1	Data collection	88
B	Markovian robots	91
B.1	Individual-based model (IBM) simulations	91
B.2	Numerical solution of master equations	91
B.3	Drift-diffusion approximation in 1D	92
B.4	Drift-diffusion approximation in 2D	94
B.5	Drift-diffusion approximation in 3D	97
C	Intermittent Collective Behavior	101
C.1	Parameter diagrams using different parameter values	101
C.2	General solution of the period distribution $P(T)$ for the CCA.	101
C.2.1	Case with different rates ($R_i \neq R_j, \forall i \neq j$).	103
C.2.2	Case with repeating rates.	103
D	Group of N particles with internal clock	105
D.0.1	Transport properties of a single particle with internal clock.	105
D.0.2	Transport properties of N independent particles with internal clock.	106

Chapter 1

The idea of individual internal states

In the present thesis we present a model inspired in biological systems where the individuals adopt different behaviors in an intermittent way and is conceived to describe the dynamics of a system of N of such particles in a simple way. Real-life examples that show this phenomenology are presented in Figure 1.1. Here, we introduce a model of active particles with a finite number of internal states. We analyse the spatial and temporal dynamics of N of such particles and show that this seemingly simple system exhibits intriguing phenomenology at the individual and collective levels. We present strong experimental evidence that suggests the existence of real biological and artificial systems at different scales where the above-described behavioral mechanism is at work. We analyse experimental data and explain how to reproduce qualitatively and quantitatively the experimental observations using our model and discuss the implications and validity of the results. We highlight the advantages of using the idea of internal states when modeling and describing real-life systems. This first chapter is devoted to present the main concept in the most general scenario and we use the following chapters to study these ideas in more concrete contexts.

1.1 The general scenario: introducing the Internal Control System (ICS)

Our subject of interest is a system of N active particles, each one with a discrete and finite number of internal states. These self-propelled particles are autonomous agents that convert energy from their environment into directed or persistent motion in space. Each particle has the capacity to interact with the surroundings (external signals) or with other particles according to various social or physical rules. In our model we assume that each one of the particles has some internal dynamics encoded in a variable called $q(t)$ that adopts only discrete values. The time dynamics of $q(t)$ is determined by a set of internal states and transition rates (as shown in the general scheme in Figure 1.1) that we call **Internal Control System (ICS)**. Technically, these states form a finite Markov chain with a continuous time dynamics.

Generally speaking, the dynamics of $q(t)$ is a stochastic process that satisfies the Markov property. Therefore, the predictions of the future values of $q(t)$ are based solely on its present value. In this sense, we can interpret the internal dynamics of $q(t)$ of each particle as a random walk through the different available internal states of the ICS.

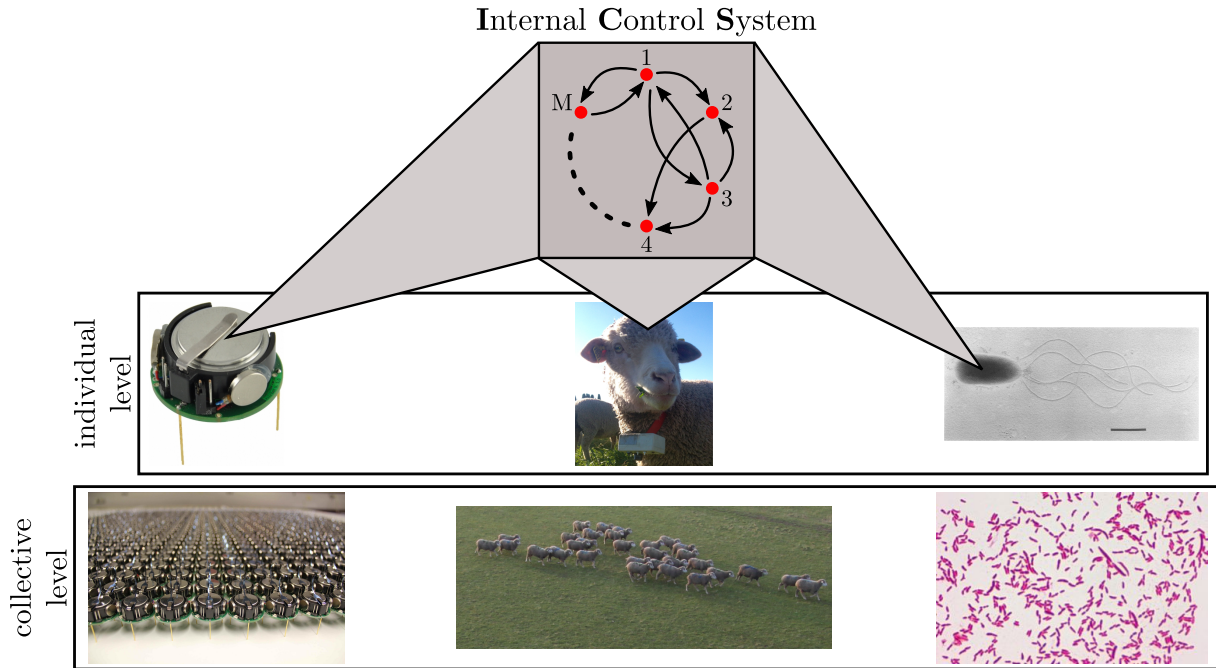


Figure 1.1 – Top: small scheme of the **Internal Control System**. Since there is a finite number of states (red dots), all of them can be labeled with numbers or letters. The black arrows represent the transition rates that link the states. Middle row: three individuals from real-life systems; a Kilobot¹, a merino sheep [1] and a bacterium called *Pseudomonas putida* [2]. Bottom row: the multiagent systems correspondent to the individuals in the middle row. These are examples of biological and artificial systems at macroscopical and microscopical scales that can be well described using our idea of the ICS.

This kind of processes are often referred as “memoryless processes” and is an important property that we discuss in Chapters 3, 4, and 5 in more concrete scenarios.

The complete spatial and temporal dynamics of one particle of the system is given by three quantities: the position $\mathbf{x}_i(t)$, the direction of motion $\boldsymbol{\theta}_i(t)$ and the internal variable $q_i(t)$. The transition rates of the ICS can, in general, depend on local values of external signals as well as the time evolution of the other particles of the system. Thus, if we call $R_{A \rightarrow B}^i$ the transition rate from an arbitrary internal state A to another arbitrary internal state B of particle i , then we have in general that this rate is function of:

$$R_{A \rightarrow B}^i = R_{A \rightarrow B}^i \left(\mathbf{x}_1(t), \boldsymbol{\theta}_1(t), q_1(t); \dots; \mathbf{x}_i(t), \boldsymbol{\theta}_i(t), q_i(t); \dots; \mathbf{x}_N(t), \boldsymbol{\theta}_N(t), q_N(t) \right), \quad (1.1)$$

with $\mathbf{x}_i(t)$, $\boldsymbol{\theta}_i(t)$ and $q_i(t)$ the variables of particle i evaluated at time t . We want to highlight that the dynamics of the ICS might seem very complicated, but the transitions between two arbitrary states are not. In fact – and regardless of the functional form of the involved rate – the stochastic process between two arbitrary states results to be a Poisson process.

In this model we also assume that the transitions between internal states of each particle are capable of directly affecting its spatial motion by activating or triggering actions like the stop of the particle’s motion or the reversal of its displacement. In other

¹Self-Organizing Systems Research Group. <https://ssr.seas.harvard.edu/kilobots>

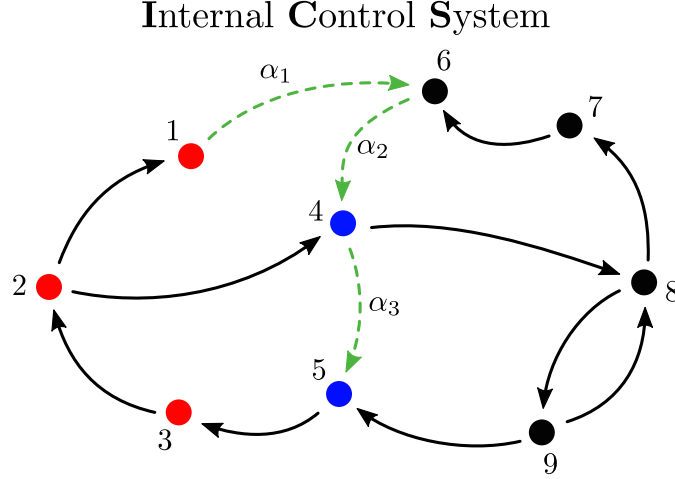


Figure 1.2 – Scheme of an example of the **Internal Control System** of an active particle. In this case, there are nine internal states depicted with solid-colored circles. The transition rates between the states are represented by arrows (solid or dashed). The colors of the dots indicate the subsets of states that have the same equation of motion, i.e. all the red-colored states have the same equation of motion, all the blue-colored also and the black-colored as well.

words, we assume that the particle obeys one different equation of motion depending on the value of its internal variable $q_i(t)$. The equations of motion might depend on the variables of the particle ($\mathbf{x}_i(t)$, $\boldsymbol{\theta}_i(t)$, and $q_i(t)$) and also on the variables of its neighbours. This can be expressed by the set of equations for one arbitrary particle i with M internal states:

$$\left. \begin{aligned} \dot{\mathbf{x}}_i(t) &= \mathbf{f}_1(\mathbf{x}_i, \boldsymbol{\theta}_i) + \mathbf{g}_1(\mathbf{x}_1, \boldsymbol{\theta}_1, q_1; \dots; \mathbf{x}_N, \boldsymbol{\theta}_N, q_N) + \boldsymbol{\xi}_1(t) \\ \dot{\boldsymbol{\theta}}_i(t) &= \mathbf{h}_1(\mathbf{x}_i, \boldsymbol{\theta}_i) + \mathbf{w}_1(\mathbf{x}_1, \boldsymbol{\theta}_1, q_1; \dots; \mathbf{x}_N, \boldsymbol{\theta}_N, q_N) + \boldsymbol{\eta}_1(t) \end{aligned} \right\} \text{if } \boxed{q_i = 1} \quad (1.2)$$

$$\left. \begin{aligned} \dot{\mathbf{x}}_i(t) &= \mathbf{f}_2(\mathbf{x}_i, \boldsymbol{\theta}_i) + \mathbf{g}_2(\mathbf{x}_1, \boldsymbol{\theta}_1, q_1; \dots; \mathbf{x}_N, \boldsymbol{\theta}_N, q_N) + \boldsymbol{\xi}_2(t) \\ \dot{\boldsymbol{\theta}}_i(t) &= \mathbf{h}_2(\mathbf{x}_i, \boldsymbol{\theta}_i) + \mathbf{w}_2(\mathbf{x}_1, \boldsymbol{\theta}_1, q_1; \dots; \mathbf{x}_N, \boldsymbol{\theta}_N, q_N) + \boldsymbol{\eta}_2(t) \end{aligned} \right\} \text{if } \boxed{q_i = 2} \quad (1.3)$$

$$\begin{array}{ccccccc} \vdots & \vdots & \vdots & \vdots & \vdots & \vdots & \vdots \end{array}$$

$$\left. \begin{aligned} \dot{\mathbf{x}}_i(t) &= \mathbf{f}_M(\mathbf{x}_i, \boldsymbol{\theta}_i) + \mathbf{g}_M(\mathbf{x}_1, \boldsymbol{\theta}_1, q_1; \dots; \mathbf{x}_N, \boldsymbol{\theta}_N, q_N) + \boldsymbol{\xi}_M(t) \\ \dot{\boldsymbol{\theta}}_i(t) &= \mathbf{h}_M(\mathbf{x}_i, \boldsymbol{\theta}_i) + \mathbf{w}_M(\mathbf{x}_1, \boldsymbol{\theta}_1, q_1; \dots; \mathbf{x}_N, \boldsymbol{\theta}_N, q_N) + \boldsymbol{\eta}_M(t) \end{aligned} \right\} \text{if } \boxed{q_i = M} \quad (1.4)$$

where $\mathbf{f}_j(\mathbf{x}_i, \boldsymbol{\theta}_i)$ represents the self-propelling drift – for example the local interaction of the particle i with external signals –, $\mathbf{g}_j(\mathbf{x}_1, \boldsymbol{\theta}_1, q_1; \dots; \mathbf{x}_N, \boldsymbol{\theta}_N, q_N)$ represents the interaction of the particle i with its neighbours and $\boldsymbol{\xi}_j(t)$ is a stochastic variable that can be of different kinds: white noise, coloured noise, etc ... Analogously, $\mathbf{h}_j(\mathbf{x}_i, \boldsymbol{\theta}_i)$ contains the local effects on the time evolution of the direction of motion, $\mathbf{w}_j(\mathbf{x}_1, \boldsymbol{\theta}_1, q_1; \dots; \mathbf{x}_N, \boldsymbol{\theta}_N, q_N)$ contains the effects that the neighbors have on the evolution of $\boldsymbol{\theta}_i(t)$ and $\boldsymbol{\eta}_j(t)$ is stochastic noise. Notice that the dimensions of \mathbf{f}_j and \mathbf{g}_j are different from those of \mathbf{h}_j and \mathbf{w}_j . If we have an n -dimensional spatial equation of motion for $\mathbf{x}_i(t)$, then we will have an $(n - 1)$ -dimensional equation for $\boldsymbol{\theta}_i(t)$.

We are particularly interested in cases where there are subsets of states where the corresponding equations of motion are equal. To fix ideas, let us do an example. We can

imagine that we have a particle with nine internal states. In this example, the equations of states 1, 2, and 3 are equal, the equations of states 4 and 5 also, and the equations of states 6, 7, 8, and 9 as well. This is depicted in a scheme with colors in Figure 1.2. The corresponding set of equations for this particle results to be:

$$\left. \begin{aligned} \dot{\mathbf{x}}_i(t) &= \mathbf{f}_{\text{red}} + \mathbf{g}_{\text{red}} + \boldsymbol{\xi}_{\text{red}} \\ \dot{\boldsymbol{\theta}}_i(t) &= \mathbf{h}_{\text{red}} + \mathbf{w}_{\text{red}} + \boldsymbol{\eta}_{\text{red}} \end{aligned} \right\} \quad \text{if } q_i = 1, 2, 3 \quad (1.5)$$

$$\left. \begin{aligned} \dot{\mathbf{x}}_i(t) &= \mathbf{f}_{\text{blue}} + \mathbf{g}_{\text{blue}} + \boldsymbol{\xi}_{\text{blue}} \\ \dot{\boldsymbol{\theta}}_i(t) &= \mathbf{h}_{\text{blue}} + \mathbf{w}_{\text{blue}} + \boldsymbol{\eta}_{\text{blue}} \end{aligned} \right\} \quad \text{if } q_i = 4, 5 \quad (1.6)$$

$$\left. \begin{aligned} \dot{\mathbf{x}}_i(t) &= \mathbf{f}_{\text{black}} + \mathbf{g}_{\text{black}} + \boldsymbol{\xi}_{\text{black}} \\ \dot{\boldsymbol{\theta}}_i(t) &= \mathbf{h}_{\text{black}} + \mathbf{w}_{\text{black}} + \boldsymbol{\eta}_{\text{black}} \end{aligned} \right\} \quad \text{if } q_i = 6, 7, 8, 9 \quad (1.7)$$

where the dependencies of the functions have been omitted and we used the color associated to each subset of states as subindex. In this case, we have nine internal states but only three equations of motion. In this scenario, our main interest is to study how and when does the particle change its equation of motion or, differently stated, **how and when does the particle change its behavior**.

The numerical implementation of the spatial evolution of the particle should be done by intercalating the equations of motion as dictated by the time evolution of the internal variable $q_i(t)$. To understand this, let us make another example using the path marked with green arrows in the ICS of Figure 1.2.

Suppose that at time $t = 0$, the value of the internal variable is $q_i(t = 0) = 1$. After some time, the dynamics is such that the transition labeled as α_1 (represented with a green-dashed arrow in Figure 1.2) takes place at time t_1 and, thus, the value of the internal variable is then $q_i(t_1) = 6$. Some time after this, at time $t_2 > t_1$, the transition labeled as α_2 happens and the value of the internal variable changes again taking the value $q_i(t_2) = 4$. Shortly after, at time $t_3 > t_2$, the transition α_3 takes place and thus $q_i(t_3) = 5$.

To compute the spatial evolution of the particle, we have to numerically integrate the “red” equations (1.5) from time $t = 0$ until time $t = t_1$. The values $\mathbf{x}_i(t_1)$ and $\boldsymbol{\theta}_i(t_1)$ become then the initial conditions for the evolution of $\mathbf{x}_i(t)$ and $\boldsymbol{\theta}_i(t)$ respectively in the time interval $t_1 \leq t \leq t_2$, which must be performed using the “black” equations (1.7). Analogously, the values $\mathbf{x}_i(t_2)$ and $\boldsymbol{\theta}_i(t_2)$ become the initial conditions for the evolution in the interval $t_2 \leq t \leq t_3$, performed with the “blue” equations (1.6). This is visually depicted in Figure 1.3. Notice that the design of the ICS will determine entirely the spatio-temporal individual and collective dynamics of the system of N active particles.

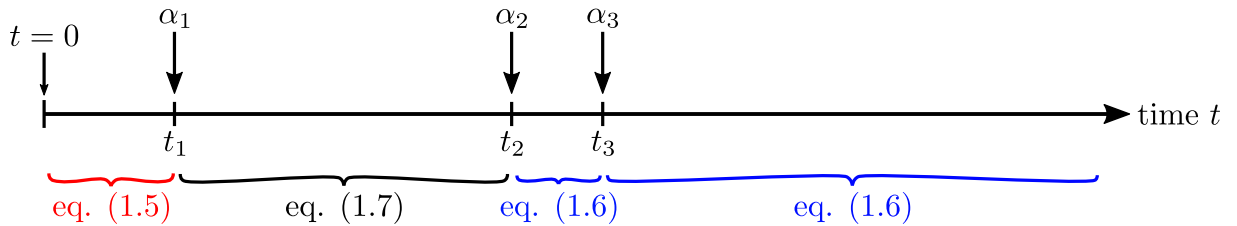


Figure 1.3 – Small scheme to understand the numerical implementation of the spatial evolution of particle i .

Although here we presented the idea of internal states and the ICS as general as possible, we will deal with simple cases of two or three states in the next chapters. We will show that these “simple” cases result to be capable of reproducing qualitatively and quantitatively diverse experimental observations of the dynamics of multiagent real-life systems, like the ones depicted in the middle and bottom rows in Figure 1.1.

The main goal of this thesis is to develop a powerful and general theoretical framework to study and describe diverse intermittent individual and collective phenomena of interacting and non-interacting multiagent systems at several scales.

We highlight that our model allows to implement the interactions between the particles at two different levels. The first one is at the internal level via the transition rates of equation (1.1). These rates regulate the characteristic times at which the internal variable $q_i(t)$ of a particle makes the transitions between states and may depend, for example, on the number of neighbors that are in the same state. The second level corresponds to the spatial interactions or spatial forces of equations like (1.2). At this level we can implement metric or topological interactions like spatial alignment with a given number of neighbors.

The present thesis is organized as follows. In the second chapter we present real biological systems at the microscopical and macroscopical scales that can be modeled using active particles with discrete internal states. We show how experimental data and measurements suggest that the observed phenomena can be described qualitatively and quantitatively using the idea of the ICS and we explain how to infer the corresponding model parameters using these data. By performing statistical analysis on the experiment measurements we are able to associate the different behaviors of individuals with one or many of the internal states of the model.

In Chapter 3 we study in detail one of the simplest scenarios of our model: non-interacting active particles that move in space with constant speed with an ICS consisting of only two states. In this case, the transition rates between the two states are regulated by the local value of a given external signal $c(\mathbf{x}, t)$. We show how in this seemingly simple case there is a wide variety of interesting behaviors like pattern formation or the following of travelling external signals. In this chapter we argue why the case of an ICS with only one internal state does not show any biased behavior and is just until having an ICS with two internal states when the particles can perform complex tasks. Since these navigation strategies are inspired in intermittent microscopical systems of bacteria like *E. coli* or *P. putida*, we discuss the similarities and differences of our model with previous works like the models for bacterial chemotaxis. In this discussion we highlight that by construction, the particles in our model do not require memory to still show non-homogeneous pattern formation. Our statements and algorithms are supported by experiments that we performed using a real robot.

In Chapter 4 we study a scenario motivated by the observed intermittent collective behavior of small groups of gregarious animals. We focus on the internal temporal dynamics of a group of N active particles that have an ICS that consists of three internal states and three transition rates that depend on the number of particles in each one of the states. This results to be the simplest case where the system displays a synchronized collective dynamics. First, we study the temporal dynamics of this system at the mean field level to have some intuition on the observed collective dynamics. We introduce two new concepts that we call the **C**ollective **C**lock **A**pproximation (CCA) and the **M**etaparticle **C**lock **A**pproximation (MCA) that allow us to give analytical expressions for observables like the average period. We test the accuracy of the CCA and the MCA with **I**ndividual **B**ased

Model (IBM) simulations and we relate the results with the mean field study. We observe that the CCA and the MCA result to be accurate approximations in the case where the system shows a high degree of synchronization of the particles. We argue why the case of an ICS of two states does not show any intermittent collective behavior independently on the functional form of the transition rates between the states.

In Chapter 5 we study the spatial dynamics of the model studied in detail in Chapter 4. Particularly, we show how the two previously introduced concepts of the CCA and the MCA result to be very useful to give analytical expressions for the collective transport properties of the whole group of N active particles that explore the space. We argue why the concepts of the **C**ollective **C**lock and the **M**etaparticle **C**lock are general for any highly synchronized system and will always give accurate results. We test the obtained analytical expressions with IBM simulations.

This thesis contains solid experimental and theoretical evidence that our model of active particles with a finite number of internal states describes real-life systems that show individual or collective spatio-temporal intermittency at different scales. We also show that the diverse phenomenology contained in the here-presented model is completely determined by the design of the **I**nternal **C**ontrol **S**ystem. In summary, our model has been developed to understand the large number of existing real systems displaying intermittent behaviors at the individual and collective levels and can potentially link physical, biological and mathematical aspects of the system.

Chapter 2

Experimental evidence of internal states in biological systems: from bacteria to sheep

Contents

2.1	<i>Pseudomonas Putida</i>	20
2.1.1	Using a model of two internal states	20
2.2	Small groups of gregarious animals	22
2.2.1	Analysis of individual signals	23
2.2.2	Individual characteristic times	24
2.2.3	Interpretation of the three states	26
2.2.4	Functional form of the transition rates	27
2.3	Summary & perspectives	30

This chapter is devoted to analyse experimental data that suggest the existence of real intermittent biological systems at different scales that can be described using internal states of individuals. First, we present a system at the microscopical scale: a bacterium called *Pseudomonas putida*. This soil bacterium is able to perform a biased motion called chemotaxis [3] and, like other prokaryotic swimmers, *P. putida* exhibits a motion pattern dominated by persistent runs that are interrupted by turning events. The majority of the turning events is characterized by an angle of 180° [4] and thus are called reversals. This is one example of a biological system where individuals are able to sense external information locally and perform a biased motion in space by changing their direction of motion in an intermittent way. Second, we study the intermittent collective behavior of small groups of merino sheep. These gregarious animals show a periodic behavior when left unperturbed in a confined area, where the individuals alternate between phases of rest and phases of activity in an intermittent way. They form compact cohesive groups that perform collective displacements triggered by any of the individuals of the group. For both cases, we show how to perform the corresponding data analysis of the experimental measurements to associate the observed behaviors of individuals with one or many of the internal states of the model. Details on the experimental methods and data acquisition for both systems can be found in Appendix A.

2.1 *Pseudomonas Putida*

Bacterial systems have been of high interest for scientists (physicists, biologists, chemists) and medical doctors for long time [5,6]. The characterization and modeling of bacteria can help to understand the infection process and might be one path to find new and less invasive cures for infections [7]. The majority of bacteria are motile thanks to one (or many) lash-like appendages that protrude from the cell body called flagella. The single flagellum is connected via a hook to a rotary motor embedded in the cell wall that drives the rotation of the filament. The swimming pattern depends on the number of flagella and their position on the bacterium body [8].

The most studied prototypical example of a bacterial swimmer is the enteric bacterium *Escherichia coli* [5]. The swimming pattern performed by *E. coli* is called run-and-tumble (RT) and is characterized by straight runs followed by short stops, often involving a change of direction. The canonical picture of bacteria with RT motility such as *Escherichia coli* or *Salmonella* [5,9] states that bacteria display exponentially distributed run-times (despite recent findings that suggest the possibility of noise-induced fat-tailed distributions [10,11]) and perform a biased motion called chemotaxis by regulating the associated tumbling frequency. By measuring the chemical concentration through clustered arrays of membrane receptors [12] and subsequent signal processing via a complex biochemical cascade [13] that leads to an effective memory [13–16], the bacterium is able to compute an external concentration gradient. It extends the duration of runs and, thus, decreases the number of tumbles when heading in the direction of the attractant gradient. This dynamics leads to biased motion toward the attractant source.

Notably, in *Pseudomonas putida* the distribution of run-times is non-exponential and exhibits a refractory period as shown in Figure 2.1a. Its motion is dominated by persistent runs that are interrupted by turning events characterized by an angle of 180° [4] called reversals. Thus, we will refer to the swimming pattern of *P. putida* as run-and-reverse (RR). Similar bell-shaped run-time distributions were reported for *Myxococcus xanthus* [17] and *Paenibacillus dendritiformis* [18] which display RR-motility as well. By adapting the reversal statistics in response to an external chemical signal $c(\mathbf{x})$, *P. putida* is able to perform chemotaxis. This becomes clear when we distinguish the run-times in the direction of the chemical source (that we call up-gradient) and the opposite direction (that we call down-gradient). We notice an asymmetry in the cumulative distribution functions of the run-times, as indicated in Fig. 2.1b. The non-exponential run-time distributions suggest that chemotaxis in *P. putida*, and potentially other bacterial species, may involve a novel taxis mechanism that is fundamentally different from the one reported for RT bacteria. Notice that if we distinguish between runs performed up or down-gradient, we get also two gamma-shaped run-time distributions (Figure 2.1b), suggesting that none of the processes can be modelled with a simple Poisson process.

2.1.1 Using a model of two internal states

One simple way to obtain qualitatively and quantitatively the same results as the experiments is to use a model of two internal states. In this scenario, there are also two possible transition rates between the internal states of the bacterium: α and β , as shown in the right plot of Figure 2.2. We assume also that the transition from state 2 to state 1 triggers a reversal of the direction of motion. These rates can be in general functions of

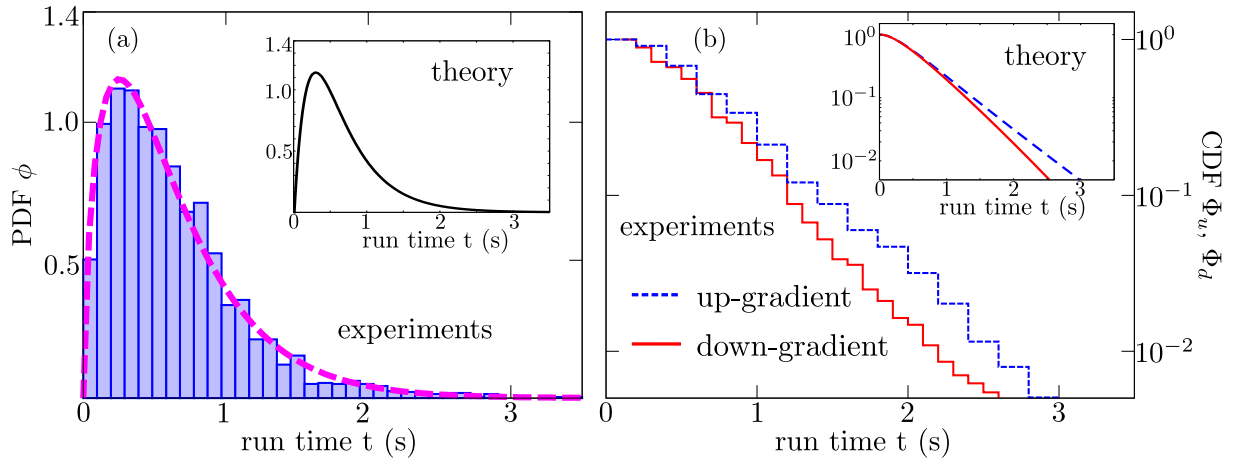


Figure 2.1 – Run-time distribution and chemotactic response of *P. putida*. Left: probability distribution function (PDF) ϕ of the run-times. Right: cumulative distribution function (CDF) of run-times discriminating between up-gradient (Φ_u) and down-gradient (Φ_d) runs. The pink-dashed curve in the left panel corresponds to a fit with a γ -PDF. The insets show that the same qualitative behavior is obtained in simulations with a two state model shown in the right plot in Figure 2.2. For the insets of this figure we used following parameters: $\alpha = 5 \text{ s}^{-1}$, $\beta(x) = c(x)^{-1} \text{ s}^{-1}$, $c(x) = 0.75(x/L) + 0.1$, $L = 750 \mu\text{m}$ and $v_0 = 30 \mu\text{m/s}$. The experimental curves were obtained from data acquired by our collaborator Carsten Beta and his group at the University of Potsdam. Details on data collection available in Appendix A.

the external signal $c(\mathbf{x})$ since experimental evidence shows that this external information influences the running times. The way to fit the parameters of the model is simple. First, experiments should be performed using a known external concentration $c(\mathbf{x})$ in order to be able to differentiate the direction of the bacterium with respect to the gradient of $c(\mathbf{x})$.

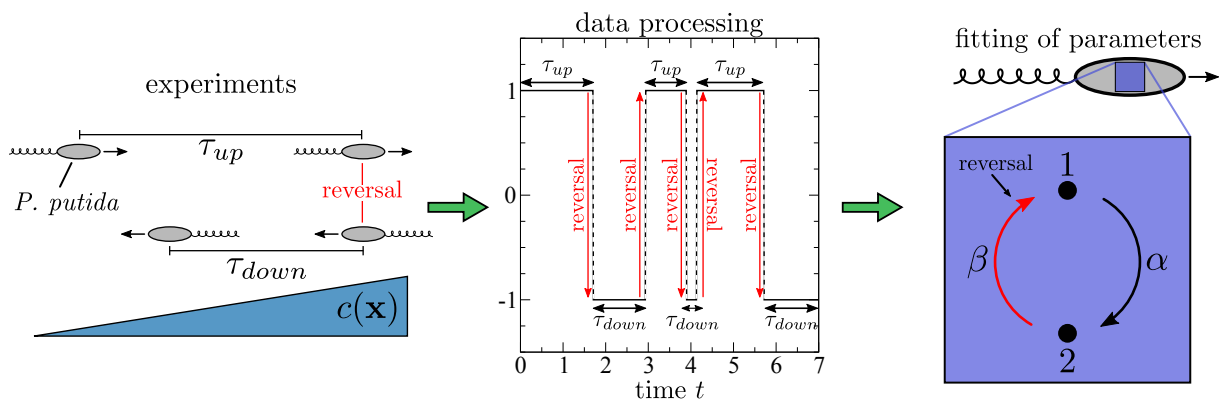


Figure 2.2 – Scheme on how to model the chemotactical behavior of *P. putida*. Left: the schematic setup of the experiments using a given external concentration $c(\mathbf{x})$ that helps to distinguish the motion of the bacteria. Center: the tracking of individual bacteria can be translated into a dicotomic individual signal, from which information on the running times τ_{up} and τ_{down} can be measured. Right: scheme of a simple two state model that can be used to reproduce the experimental results as shown in the insets of Figure 2.1.

Then, and with the help of a proper tracking of individual bacteria, a dicotomic signal can be generated in order to measure the running times τ_{up} and τ_{down} correspondingly, like the middle plot in Figure 2.2. By obtaining the probability distributions $P(\tau_{up})$ and $P(\tau_{down})$ for both times, one can fit the two rates using the first and second moments of the distributions.

The internal states mimic the fact that a taxis response of a microorganism to an external signal or field, such as a chemical concentration or temperature gradient, requires to sense this signal, internalize and process it (presumably involving cascades of biochemical events) and execute a behavioral response (e.g. a reversal), after which the microorganism continues sensing, processing and responding to the signal. The main assumption is that this complex cycle can be reduced to a series of stochastic checkpoints or steps inside the organism, where some or all of them depend on the external signal. The internal dynamics is, by definition, Markovian: it does not incorporate or presuppose memory in any manner.

2.2 Small groups of gregarious animals

In nature, many species of animals live in large and small groups [19, 20]. The scientific community believes that this aggregation in groups is the result of a balance between benefits, like protection or high probability to find a mate partner, and costs, like reduction of resources. Although the study of several animal groups suggests this is true, a lack of quantitative studies aiming to understand the collective phenomena makes it difficult for scientists to make predictions of the several properties of the groups. Recent exceptions are [21, 22].

For the detailed study of multiagent biological systems, the data acquisition plays a fundamental role. In the past decade, there has been an important development in the quality and methods for acquiring data from the experiments [23, 24]. This serves to compare the proposed models and the dynamics of real systems, fundamental aspect in science. Although the obtaining of proper data in big groups of animals can be unrealistic, this is not the case for small groups.

In this section we aim to understand the spatio-temporal dynamics of small groups of merino sheep, which are gregarious animals. For that, we performed a series of experiments with groups of $N = 2, 3,$ and 4 individuals. Each group was freed in an arena of size $80\text{m} \times 80\text{m}$ and left there for 30 minutes. We noticed that the groups presented collective displacements followed by intervals of no motion, as depicted in Figure 2.3a for a group size $N = 4$. Based on experimental observations, we noticed that the triggering of the collective motion of the group could be started by any of the individuals. Thus, any individual can become what we will call “incidental leader”. The collective displacements of the group are characterized by the formation of files or rows – i.e. individuals place themselves in a line, one after the other, see Figure 2.3a – with the incidental leader at the front. Despite the complex dynamics of the group, the observation at the long term for all group sizes is that individuals tend to stay together forming a cohesive group.

To study the spatial and temporal dynamics of the system, we used a specialized software to obtain information of the individuals. We obtained the position $\mathbf{r}_i(t)$, the orientation $\theta_i(t)$ and the velocity $\mathbf{v}_i(t)$ for each sheep. Details on data acquisition are available in Appendix A.

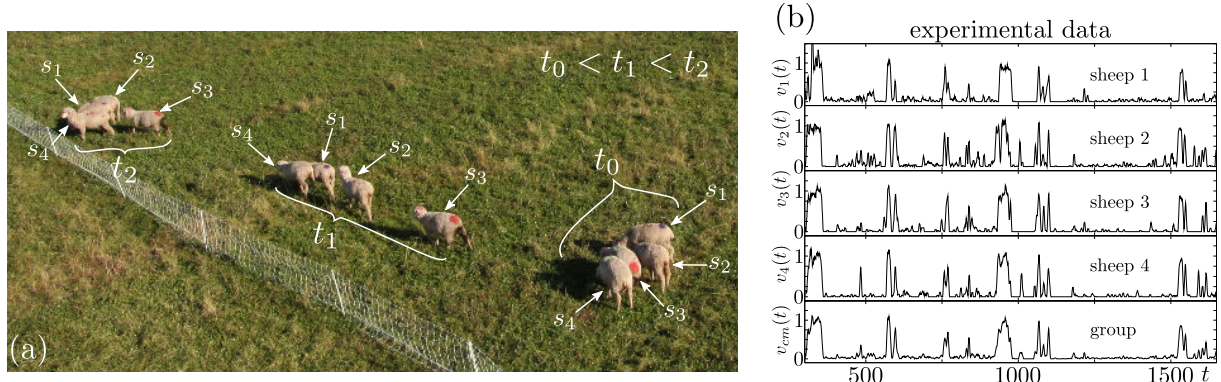


Figure 2.3 – (a) Snapshot of an experiment with a group of size $N = 4$ sheep. We can distinguish the existence of a collective motion between phases where the group does not move. We use the nomenclature: $s_1 = \text{sheep 1}$, $s_2 = \text{sheep 2}$, \dots , $s_i = \text{sheep } i$. (b) Raw data of the individual speeds $v_i(t) = |\mathbf{v}_i(t)|$ as a function of time for a group of $N = 4$ sheep, as well as the speed of the center of mass of the group $v_{cm}(t)$.

2.2.1 Analysis of individual signals

When observing the temporal dynamics of the speeds $v_i(t) = |\mathbf{v}_i(t)|$, we notice a high degree of synchronization between the individual signals, as shown in Figure 2.3b. When plotting a collective observable like the speed of the center of mass $v_{cm}(t) = |\mathbf{v}_{cm}(t)|$, with

$$\mathbf{v}_{cm}(t) = \dot{\mathbf{x}}_{cm}(t) = \frac{1}{N} \sum_{i=0}^N \dot{\mathbf{x}}_i(t), \quad (2.1)$$

we notice that the resulting collective signal is strongly correlated with the individual signals. This makes us think that in such a highly synchronized system, any individual is a good representant of the whole group.

To be able to study the temporal dynamics of the system, we need first to find a threshold value of the individual speeds that allow us to declare when an individual is “moving” and when it is “at rest”. In order to find this threshold speed v_{th} , we study the normalized distribution $P(v)$ of the individual speeds of sheep. After plotting this distribution we notice that it results to be bimodal and it can be seen as the sum of two separate distributions, one associated to slow moving sheep and one associated to fast moving sheep. Following the same procedure as [25], we fit a Poissonian function

$$F_1(v) = a_0 v \exp\left(-\frac{v}{a_1}\right) \quad (2.2)$$

for the slow moving sheep and a skewed gaussian

$$F_2(v) = b_0 v \exp\left(-\frac{(v - b_1)^2}{2b_2^2}\right) \quad (2.3)$$

for the fast moving sheep, with a_0 , a_1 , b_0 , b_1 and b_2 fitting parameters. The values obtained for both distributions (2.2) and (2.3) for $N = 4$ are $a_0 = 94.37$, $a_1 = 11.84$, $b_0 = 0.72$,

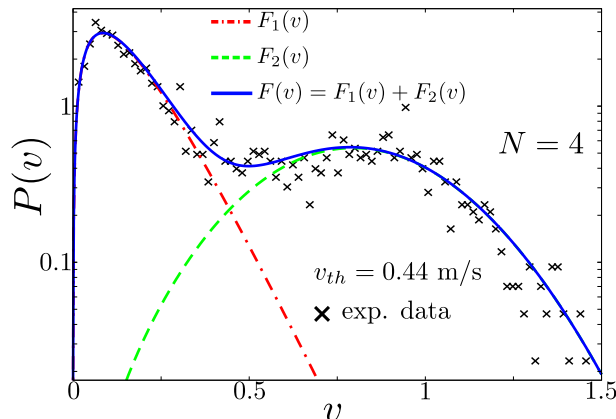


Figure 2.4 – Threshold determination with experimental data. A poissonian $F_1(v)$ (red dot-dashed line) and a skewed gaussian $F_2(v)$ (green dashed line) were fitted to the experimental data. The sum of both functions $F_1(v) + F_2(v)$ is plotted with a solid blue line. The intersection of $F_1(v)$ and $F_2(v)$ defines the threshold speed we need, resulting $v_{th} = 0.44$ m/s in the case of group size $N = 4$. The procedure was analogous to the one used in [25].

$b_1 = 0.69$ and $b_2 = 0.28$. We can define a speed threshold v_{th} separating high from low speeds by the condition:

$$F_1(v_{th}) = F_2(v_{th}), \quad (2.4)$$

which gives $v_{th} = 0.44$ m/s. The analysis of the data and the fitting functions are presented in Figure 2.4. Performing the same data analysis for the other group sizes $N = 2, 3$ gives similar values: $v_{th} = 0.464$ m/s for $N = 2$ and $v_{th} = 0.445$ m/s for $N = 3$. Since all of this values are very similar, we use the average of the four values, hence $v_{th} = 0.4496$ m/s ≈ 0.45 m/s.

2.2.2 Individual characteristic times

Using the obtained value for the threshold speed v_{th} , we can now translate the information of the individual speeds $v_i(t)$ into individual dicotomic signals that tell us when an individual is moving and when it is not, as shown in Figure 2.5b. Having the processed signal helps us to define without ambiguity two individual characteristic times: the time of motion τ_m and the time of no motion τ_{nm} as shown in the zoom of Figure 2.5b. Now, we can perform a statistical analysis to both characteristic times. We can compute the corresponding probability distributions $P(\tau_m)$ and $P(\tau_{nm})$. By doing so, we notice that the two probability distributions are qualitatively different, as shown in Figure 2.5c and Figure 2.5d. On the one hand, $P(\tau_m)$ results to be monotonically decreasing, whereas $P(\tau_{nm})$ results to be rather gamma-shaped. A χ^2 -test tells us that the functional form of $P(\tau_m)$ is consistent with an exponential of the form:

$$P(\tau_m) = c_1 e^{-c_1 \tau_m}. \quad (2.5)$$

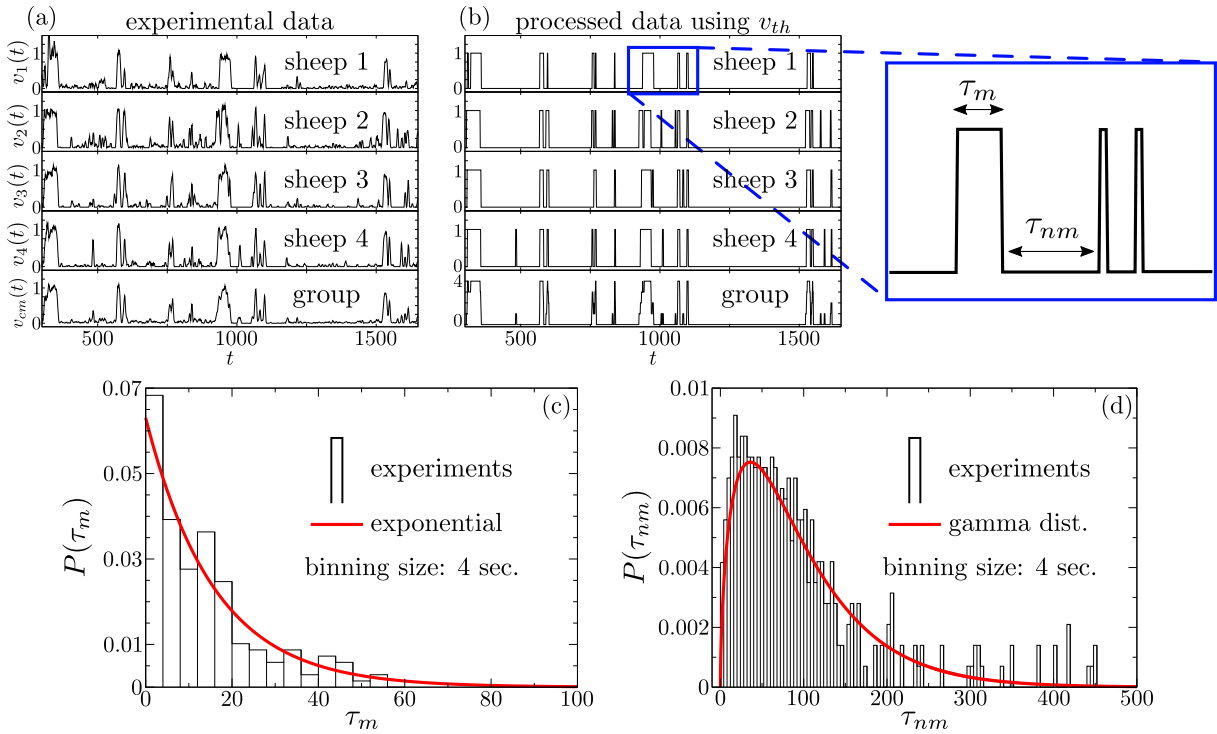


Figure 2.5 – (a) and (b) With the threshold speed v_{th} , we can translate the individual speed signals $v_i(t)$ into individual dicotomic signals to define the characteristic individual times. We can define the times of motion τ_m and the times of no motion τ_{nm} , as shown in the highlighted zoom of (b). (c) and (d) The experimental probability distribution functions $P(\tau_m)$ and $P(\tau_{nm})$ are presented, as well as the theoretical fits (2.5) and (2.6). All plots in this figure are done for group size $N = 4$ and using the same binning of 4 seconds for (c) and (d).

Analogously, the corresponding χ^2 -test tells us that the functional form of $P(\tau_{nm})$ is rather a gamma-shaped distribution of the form:

$$P(\tau_{nm}) = \frac{\kappa^M \tau_{nm}^{M-1}}{(M-1)!} e^{-\kappa \tau_{nm}} \quad (2.6)$$

The corresponding p-values, as well as the parameters of equations (2.5) and (2.6) are given in Table 2.1 and Table 2.2.

N	c_1	p-value	sign. level
2	14.1	0.034	5%
3	24.02	0.016	5%
4	25.8	0.014	5%

Table 2.1 – Parameters and p-values for the $P(\tau_m)$ distribution.

N	κ	M	p-value	sign. level
2	0.021	1.35	0.031	5%
3	0.016	1.45	0.023	5%
4	0.017	1.60	0.036	5%

Table 2.2 – Parameters and p-values for the $P(\tau_{nm})$ distribution.

Notice that the main difference between the two distributions is that

$$\lim_{\tau_{nm} \rightarrow 0} P(\tau_{nm}) = 0, \quad \text{whereas} \quad \lim_{\tau_m \rightarrow 0} P(\tau_m) \neq 0.$$

This is telling us that the probability that one individual (that was previously running) stops and immediately begins to run again is almost zero. Technically, we can say that there exists a refractory period associated to the no motion times.

These statistical tests tell us that the motion times τ_m can be associated to a Poisson process. On the other hand, the no motion times τ_{nm} can not. The simplest situation to be able to reproduce the experimental observations is to use a three state model at the individual level. Within the three states, two of them should be associated to the no motion individual times, and one to the motion times. Hence, for simplicity, we call the first two no motion states S_1 and S_2 , and we call M to the motion state, as shown in Figure 2.6. In general, we have six possible transition rates between the states, highlighted in with red and blue arrows in Figure 2.6.

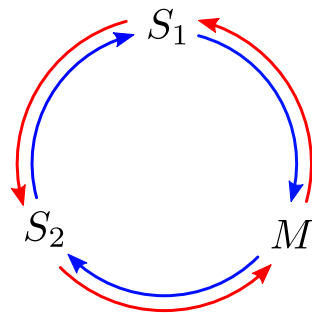


Figure 2.6 – The states S_1 and S_2 are associated to the no motion of individuals, while state M is associated to the motion phase. In general, there are six possible transitions between the three states, plotted with red and blue arrows.

2.2.3 Interpretation of the three states

In the past section, arguments were given to support that a three state model can potentially describe the dynamics of the small groups of sheep. In this section, we are going to discuss how to differentiate these states in the experimental data. Using the threshold speed v_{th} we can differentiate if the individual is moving or not and, thus, know if it is either in state M or in one of the no motion states S_1 or S_2 . By taking a closer look at the experimental videos we identified two clearly distinguishable behaviors of the individuals during the time of no motion. While not moving, sheep spent the time either having the head close to the grass (mainly eating) or having the head up looking around, most probably looking for potential threats or observing the behavior of the group. This results to be a key observation in order to be able to associate the two no motion states S_1 and S_2 with two individual behaviors that are complementary to each other. In easy terms: in the no motion phase, individuals have either the head down or the head up. This allows us to name the state S_1 as the “grazing” state and the state S_2 as the “head up” state. By adding this information to the tracking of individuals we can determine its state univocally for all times. In this way, we can quantify how often do the transition rates between the states happen. After analysing the transition rates for all group sizes we noticed that out of the six possible transition rates, there are only three that are the most frequent. They are the transition $S_1 \rightarrow M$, $M \rightarrow S_2$ and $S_2 \rightarrow S_1$, as shown in Figure 2.7. This suggests that although the six rates are present in the experiments, the dynamics can be described by three effective rates, as shown in the left plot of Figure 2.8.

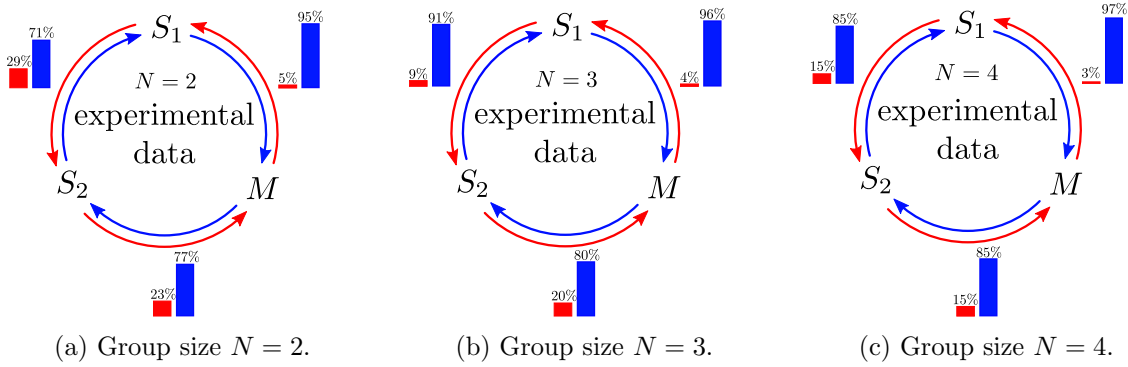


Figure 2.7 – Using the interpretation of the three states and the tracking done in experiments we calculated the percentage of each of the transitions.

2.2.4 Functional form of the transition rates

Having already fixed the number of states and the number of possible transitions, we have now to define the transition rates. The question now would be: which effects do we observe in the experiments and how are we going to model or represent them? In the past, there have been some works dedicated to study this collective effect between sheep. Toulet et. al [1] performed experiments to understand the influence of a leader inside the group of merino sheep. Experimental data suggest that individuals face a problem of a dicotomic decision-making. It seems that all is reduced to two possible scenarios: either following the incidental leader or staying with the rest of the group. A scheme that explains this decision-making can be found in the right plot of Figure 2.8.

Regarding the effect of incidental leadership, we observed that it is of stochastic nature but also dependent on the group size, something not reported up to date to our knowledge. For instance, the triggering of collective displacements is more frequent in groups of $N = 2$ sheep than groups of $N = 3$ or $N = 4$ sheep. In order to take all these observations and

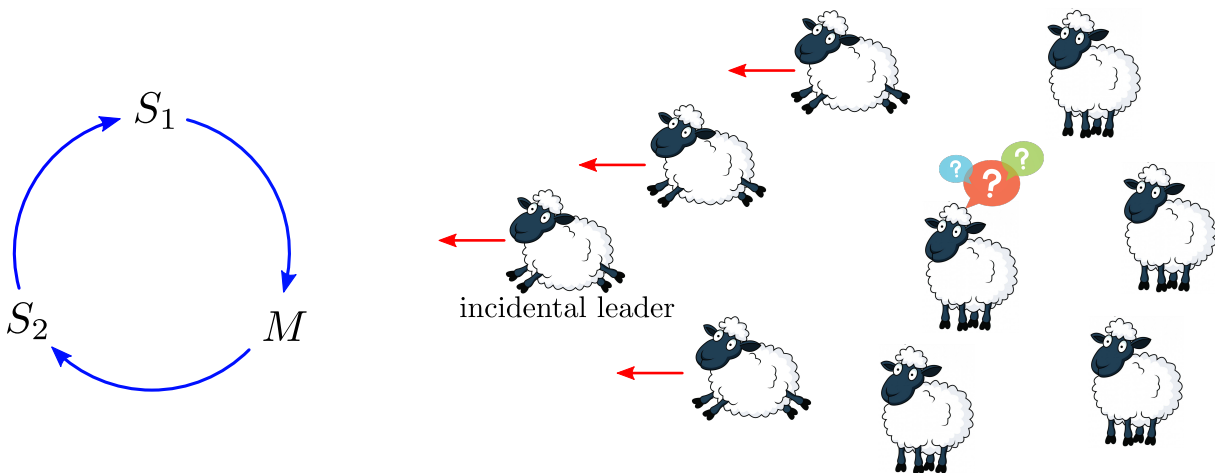


Figure 2.8 – Left: the three state scheme that is suggested by the analysis of experimental data with only three effective transition rates. Right: scheme of the decision making of individual sheep in a group.

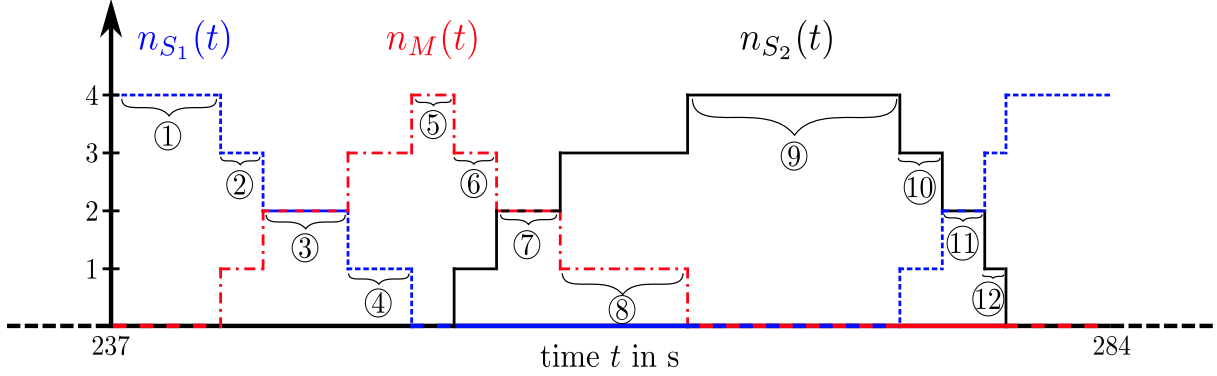


Figure 2.9 – Experimental data are presented for a group of $N = 4$ sheep. The labels serve to associate the measurements of these collective signals with the data shown in Figure 2.10.

effects into account, we use the following form for the individual transition rate from an arbitrary state i to another state j :

$$R_{i \rightarrow j}(n_i, n_j) = \underbrace{\frac{\mu_{i \rightarrow j} n_j^{\beta_{i \rightarrow j}}}{n_i^{\gamma_{i \rightarrow j}}}}_{\text{interaction with neighbours}} + \underbrace{\frac{\omega_{i \rightarrow j}}{n_i^{\delta_{i \rightarrow j}}}}_{\text{incidental leadership}}, \quad (2.7)$$

where $\mu_{i \rightarrow j}$, $\beta_{i \rightarrow j}$, $\gamma_{i \rightarrow j}$, $\omega_{i \rightarrow j}$ and $\delta_{i \rightarrow j}$ in equation (2.7) are constant parameters for each transition and they should be fixed using the experimental data. The first term in (2.7) models the interaction with the neighbours and depends on the number of individuals in each state, defined as:

$$n_{S_1}(t) = \sum_{i=1}^N \delta_{q_i(t), S_1}, \quad n_M(t) = \sum_{i=1}^N \delta_{q_i(t), M}, \quad n_{S_2}(t) = \sum_{i=1}^N \delta_{q_i(t), S_2}. \quad (2.8)$$

The second term in (2.7) models the rate associated to the spontaneous triggering of the collective change of states. If we plot these functions, we can find a behavior like the one plotted in Figure 2.9, where data is shown for an experiment of $N = 4$ sheep. Using this three functions with all the data we have, we are able to make an average of the times marked with circled numbers in Figure 2.9. Each one of this values can be linked with the transition rates of the three state theory in (2.7). Having all this average values makes it possible to select the set of parameters through a minimization process. This involved the calculation of all the errors between the experimental data and the expected theoretical value of the transition. The selection of the parameters was made in such a way that the total error (the sum of all errors of all group sizes) was minimized. The functional form of the rates in equation (2.7) as well as the obtained experimental values are plotted in Figure 2.10.

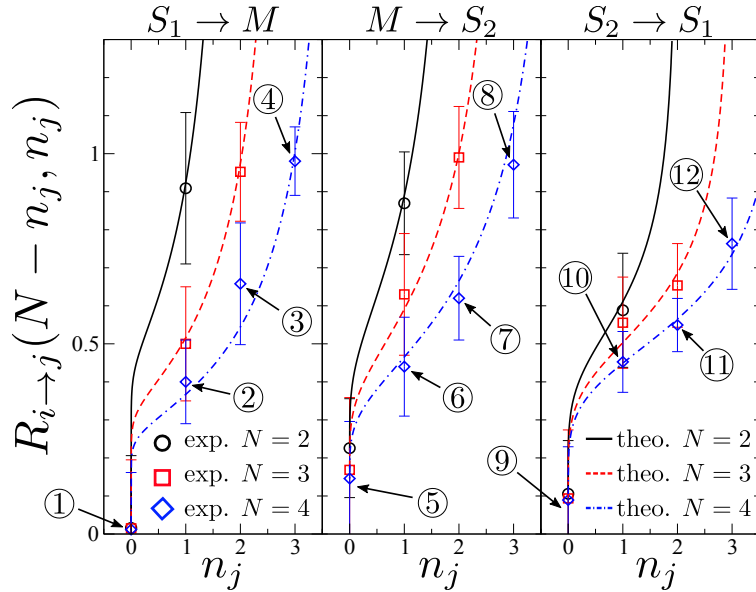


Figure 2.10 – In this figure, the functional form of the transition rates (2.7), as well as the experimental measurements are presented for the three transitions: from $S_1 \rightarrow M$, from $M \rightarrow S_2$ and from $S_2 \rightarrow S_1$.

We noticed, however, that the value of parameters $\gamma_{i \rightarrow j}$ and $\delta_{i \rightarrow j}$ resulted to be very similar. In the case of transition $S_1 \rightarrow M$, the values are $\gamma_{S_1} = 1.84$ and $\delta_{S_1} = 1.82$. For transition $M \rightarrow S_2$, the values are $\gamma_M = 1.59$ and $\delta_M = 1.61$. For the third transition from $S_2 \rightarrow M$, the values are $\gamma_{S_2} = 1.28$ and $\delta_{S_2} = 1.27$. Thus, we can simplify the originally proposed transition rates in equation (2.7) by using $\delta_{i \rightarrow j} \approx \gamma_{i \rightarrow j}$ and propose:

$$R_{i \rightarrow j}(n_i, n_j) = \frac{\mu_{i \rightarrow j} n_j^{\beta_{i \rightarrow j}} + \omega_{i \rightarrow j}}{n_i^{\gamma_{i \rightarrow j}}}. \quad (2.9)$$

The complete table of fitted parameters is given in Table 2.3. The fact that the spontaneous rate depends on the system size has not been reported to our knowledge. It results that it decreases with the number of individuals N , which means that in average an observer has to wait longer to see a collective displacement in groups of four individuals than in groups of two.

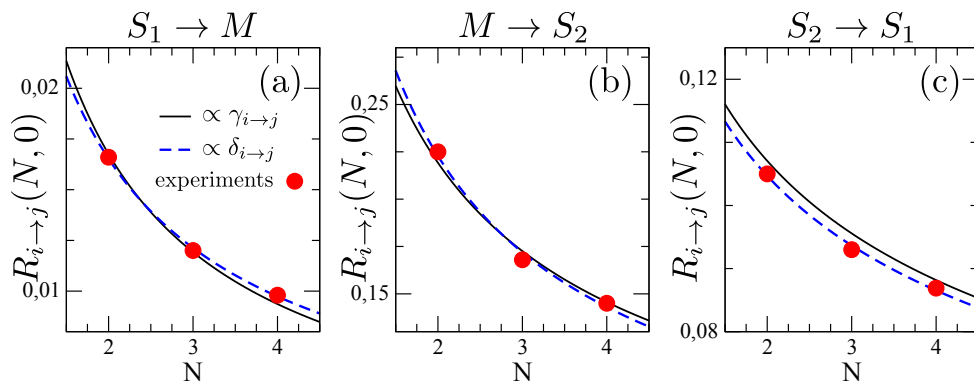


Figure 2.11 – Plotting of the spontaneous rates for all three transitions, as well as two theoretical curves proportional to parameter $\gamma_{i \rightarrow j}$ and $\delta_{i \rightarrow j}$.

$S_1 \rightarrow M$	$M \rightarrow S_2$	$S_2 \rightarrow S_1$
$\mu_{S_1 \rightarrow S_2} = 0.89 \pm 0.13$	$\mu_{M \rightarrow S_2} = 0.56 \pm 0.22$	$\mu_{S_2 \rightarrow S_1} = 0.48 \pm 0.16$
$\beta_{S_1 \rightarrow S_2} = 0.07 \pm 0.06$	$\beta_{M \rightarrow S_2} = 0.26 \pm 0.11$	$\beta_{S_2 \rightarrow S_1} = 0.21 \pm 0.08$
$\gamma_{S_1 \rightarrow S_2} = 1.84 \pm 0.17$	$\gamma_{M \rightarrow S_2} = 1.59 \pm 0.12$	$\gamma_{S_2 \rightarrow S_1} = 1.28 \pm 0.30$
$\omega_{S_1 \rightarrow S_2} = 0.03 \pm 0.09$	$\omega_{M \rightarrow S_2} = 0.33 \pm 0.14$	$\omega_{S_2 \rightarrow S_1} = 0.13 \pm 0.11$

Table 2.3 – Parameters of the model fitted with experimental data. This set of parameters fits the experimental values for all group sizes $N = 2, 3$, and 4, as shown in Figure 2.10.

2.3 Summary & perspectives

In this chapter we analyzed two different biological systems looking for clues and hints that suggest that the observed intermittent phenomenology can be explained using models of active particles with a finite number of discrete internal states. Most importantly, we show how to extract vital information from the experimental data to be able to associate the individual behaviors with one or many of the internal states of our theoretical framework. First, we discussed the main features of the spatio-temporal dynamics of bacteria called *Pseudomonas putida*. We explain the process that leads to the mining of valuable information from the experiments and explain how to relate this experimental measures with the parameters of our model. This analysis will serve as a motivation for the whole development of what we will call navigation strategies and that will be discussed in detail in the next chapter.

Second, we studied the temporal collective dynamics observed in small groups of gregarious animals. Using the experimental observations, we deduce the minimal model that we should use to describe the collective phenomena. Therefore, the resulting model is completely data driven. We used a mixture of previous studies [1] with new discoveries – like the dependency of the spontaneous rate on the group size – to deduce the appropriate model. We will study separately the spatial and the temporal dynamics of this model in Chapter 4 and Chapter 5.

Notice that in this chapter, one of the most important aspects is the fact that performing statistical analysis on the experimental measurements allows us to relate the behaviors of individuals with the internal states of our model in both cases.

Chapter 3

Individual Navigation Strategies

Contents

3.1	Introducing the Markovian robots	32
3.2	Markovian robots with different NCS's	35
3.2.1	Spatial dynamics	35
3.2.2	A didactic introduction	36
3.2.3	Effective Langevin dynamics	36
3.2.4	NCS motif 1: up- & downgradient motion	38
3.2.5	NCS motif 2: adaptation	40
3.3	Performing complex tasks	41
3.4	Two & three-dimensional systems	43
3.5	Tests with a real robot	49
3.6	Summary & perspectives	52

In this chapter we study in full detail the spatio-temporal dynamics of non-interacting active particles with internal states and transition rates that depend on local measurements of a given external signal $c(\mathbf{x}, t)$. The particles move with constant speed v_0 in space.

We study the long-time behavior of a system of N of these particles and obtain the stationary probability distribution function $P(\mathbf{x})$ of finding one at position \mathbf{x} . We show that the simplest case where the system shows a non-trivial distribution is the case where individual particles have two internal states and the two transition rates between them are different. In this scenario we demonstrate that these particles can be designed to perform complex tasks such as adaptive chemotaxis, detection of maxima or minima, or selection of a desired value in a dynamical, external field $c(\mathbf{x}, t)$.

In this chapter we refer to these active particles as *Markovian robots* (MR). We provide experimental evidence that suggests that our model (and algorithms within) is robust enough to external fluctuations. This minimalistic model results to be a theoretical toolbox to engineer autonomous agents that require very small computation capacity (and thus very “cheap”) that are able to perform several complex tasks in fluctuating environments. We are convinced that these ideas will pave the way toward a novel quantitative modeling of phenomena like bacterial chemotaxis in a (near) future. Since in this chapter

we introduce novel navigation strategies for active particles, we will refer as **Navigation Control System (NCS)** to what we defined in Chapter 1 as the **Internal Control System (ICS)**. All the navigation strategies introduced in this chapter are motivated by the behaviors observed in microscale bacterial systems, like the ones discussed in Chapter 2. All the results presented in this chapter have been published in Physical Review E [26].

3.1 Introducing the Markovian robots

As early as 1959, Feynman discussed the technology transfer from the macro- to the microscale, a highly relevant field of research nowadays in terms of medical applications such as targeted drug-delivery and microsurgery [27]. In recent years, the remarkable advance of nanoscience has made the fabrication of synthetic and molecular machines such as sensors and actuators possible [28–30]. Moreover, micrometer-sized devices capable of moving autonomously in a fluid are already a reality. We refer to these microdevices as microrobots. Microrobots can transport cargo and invade cells; healthcare applications for early diagnosis, targeted drug delivery or nano-surgery appear therefore realizable in the not too distant future [31–34]. There exists a large variety of microrobots, rigid and soft ones, whose self-propulsion can be achieved via electrical, chemical or optical stimulation [31–34]. The direction of navigation of these devices can be controlled remotely, for instance via a magnetic field in chemically-driven nanorods [30]. However, the ultimate goal is to design and fabricate microrobots with a programmable, autonomous navigation system on board integrating both, sensors, an energy source and actuators. At present, the miniaturization of autonomous robots has advanced up to the millimeter scale [35,36]. Further progress along these lines requires the development of minimalistic, yet robust algorithms in the sense that they should work reliably in the presence of noise.

Physical properties of small size objects, e.g. at the micro-scale, impose technical constraints on the design of microrobots: viscous forces dominate over inertial ones, fluctuations of thermal origin are not negligible and the instantaneous sensing of external signals can only involve local values, but never gradients [9, 12, 37]. For this reason, here we consider a class of autonomous, self-propelled particles, which we refer to as *Markovian robots* (MR), that move at constant speed, are subject to fluctuations, and can only sense external local values of an external field (see Figure 3.1). Notice that we adopt the same constraints small objects are subjected to, but we do not need to assume necessarily that we work at microscopic scales: the proposed navigation strategies are also of interest for macroscopic robots exposed to weakly modulated signals with respect to their characteristic spatial variation. Nevertheless, the long-term motivation of this study is to pave the way for the engineering, in a near future, of tiny, autonomous robots. With this intention in mind, we aim at conceiving simple machines that are able to navigate across a complex field – providing valuable information clues – in an autonomous way with a minimum of information storage capacity. Specifically, we equip these machines with a navigation control system (NCS) that triggers random changes in the self-propulsion direction of the robots. An essential aspect of the NCS is that it exhibits only two internal states, meaning that the NCS state can be stored in a single internal Boolean variable that adopts two values. Transitions between these Boolean values are determined by a closed Markov chain, with transition rates that may depend on the instantaneous local value of the external field; see Figure 3.1 for sketches of the two relevant NCS discussed in this work. Only one

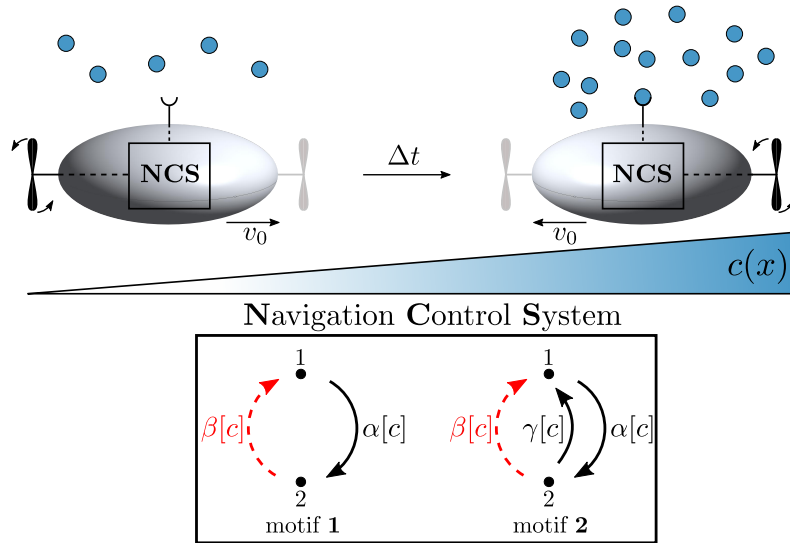


Figure 3.1 – Illustration of the general dynamics of Markovian robots. A robot that had initially moved from left to right in an external field $c(x)$ changed its direction of active motion after some time Δt . The navigation control system (NCS) controls the moving direction of the robot, by triggering reorientation events. It is connected to a sensor which measures the local field values. The internal state of the NCS is given by a single Boolean variable adopting the values 1 or 2. The NCS dynamics obeys a closed Markov chain, with transition rates that may depend on the value of the external field as measured by the sensor. The red arrow corresponds to the transition that triggers a reorientation event.

of the transition pathways in the closed two-state Markov chain triggers random reorientation in the moving direction. It is worth noticing that the closed-loop nature of the investigated Markov chains ensures the constant resetting of the internal Boolean variable, preventing the presence of fixed points in the dynamics of this variable. Importantly, the NCS does not store previous measurements in the form of internal continuous variables, preventing a priori any mathematical operation to estimate the gradient of the external field. We show that, despite the strong requested constraints, it is possible to conceive closed Markov chain motifs that lead to non-trivial motility behaviors. By analytically reducing the complexity in the NCS dynamics, we obtain an effective description of the long-time motility behavior of the MR that allows us to identify the minimum requirements in the design of NCS motifs and transition rates to perform complex navigation tasks such as adaptive gradient following, detection of minima or maxima, or selection of a desired value in a dynamical, external field. We show that MR having a NCS with at least two states exhibit non-trivial motility behaviors in one, two and three dimensions.

We put these concepts in practice by assembling a macroscopic robot that operates by the proposed NCS and is subjected to the constraints indicated above. A series of statistical tests allows us to assess the robustness of the proposed minimalistic navigation algorithms. The performance of the robot provides solid evidence in favor of the practical interest of these ideas as well as a proof-of-concept that is possible to navigate through a complex information landscape with only 1-bit of memory. These ideas may prove of help in the engineering of miniature robots.

The minimalistic navigation strategies discussed here are fundamentally different from

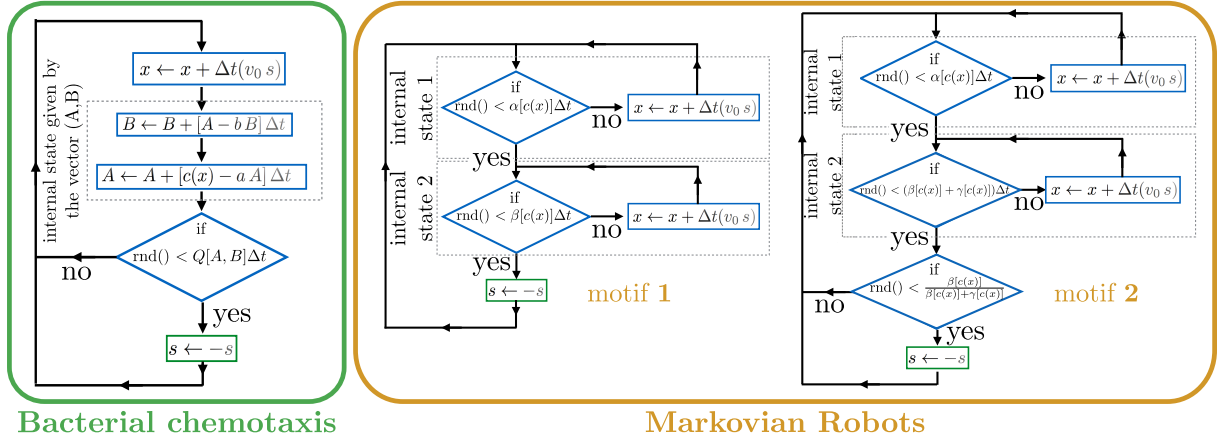


Figure 3.2 – Flowcharts of the algorithms for bacterial chemotaxis, according to [13], and Markovian robots (MR), motif 1 and motif 2. The initial condition is not explicitly shown. Notice the presence of two continuous variables, A and B , for bacterial chemotaxis, which are absent for MRs. Further, we point out that the dynamics of A and B evolves toward a fixed point for constant $c(x)$, implying that the internal state in the bacterial chemotaxis model reaches a steady state. In MR, on the other hand, the internal state always oscillates. The symbols Q , α , β , and γ refer to transition rates, Δt to the time step, $c(x)$ to the value of the external field at position x , v_0 to the speed, and s the moving direction (+1 or -1) in one dimension; $\text{rnd}()$ is a uniformly distributed, random number between 0 and 1. The definition of α , β , and γ are provided in the main text; notice that these rates do only depend on $c(x)$. On the other hand, $Q(A, B)$ is a function of the internal state itself, $Q(A, B) = d_1 A - d_2 B$, where d_1 and d_2 as well as a and b are constant; for details on the bacterial chemotaxis algorithm see [13].

bacterial chemotactic strategies [9, 12–16, 38–40] as explained in the following. In [13], Celani and Vergassola have cleverly shown that bacterial chemotaxis can be described in a Markovian way by enlarging the space of variables, beyond position and velocity variables, to include continuous (as opposed to Boolean) internal variables. The temporal dynamics of these continuous variables obeys a chain of ordinary differential equations, where the first of them depends on the external field. The frequency of changes in the moving direction of the bacterium is a function of these variables. According to [13], chemotactic behavior is already obtained by keeping the first two of these internal continuous variables. The past measurements are encoded by these continuous variables [13], that, from an algorithmic point of view, need to be constantly updated, see Figure 3.2. These dynamical variables are somehow connected to cellular chemical species, see [41] for more details. It is worth mentioning that similar mathematical procedures to the ones utilized here have also been used in the context of bacterial chemotaxis, namely a reduction of a complex internal dynamics in order to obtain the effective long-time motility behavior, see e.g. [13, 14, 42]. However, we stress that the analogy between bacterial chemotaxis and here-discussed navigation strategies is limited to the observation that both strategies are Markovian and make use of internal states. Notably, there is no direct link between them; see Figure 3.2 for a comparison at the algorithmic level. Looking in detail, the differences become evident: here, we discuss navigation strategies that make use of a single internal

Boolean variable to describe the internal state of the moving entity, while in [13] the internal state of the bacterium is described by (a minimum of) two continuous variables. From this, it is evident that MR have only two possible internal states, while in [13] the internal state of a bacterium is given by vector $\mathbf{q} = (A, B)$, with $A \geq 0$ and $B \geq 0$ two internal continuous variables, implying that there is an infinite (or at least a very large) number of potential internal states. Furthermore, the temporal evolution of the continuous variables A and B is given, as indicated above, by a hierarchy of ordinary differential equation, while in MR the temporal evolution of the Boolean variable is given by a closed Markov chain. The differences between both strategies are evident even for a trivial scenario where the external field is constant. The internal variables A and B would converge in this scenario to a fixed point and, thus, the internal state reaches a stationary state. In contrast, the internal state of MR never converges to a stationary value but oscillates ad infinitum. Another indication, how different these strategies are, is the following: the frequency at which the direction of motion changes in the model [13] is a function of the value of internal state, i.e. $Q(A, B)$ in Figure 3.2, while that is not the case for MR. In summary, the mathematical structure of both strategies are, analytically and algorithmically, fundamentally different.

3.2 Markovian robots with different NCS's

In this section, several variants of MR are introduced with a particular focus on their capability of responding to a static, external (scalar) field. At first, the general dynamics in space – equal for all model variants – is formulated. Subsequently, several examples of increasing complexity of the internal robot dynamics, which controls the occurrence of reorientation events, are studied. In particular, an effective Langevin dynamics is derived analytically for each case, which reveals the large-scale robot dynamics in the diffusive limit. These concepts are illustrated within a didactic introduction first by means of a simplified version of the model where the reorientation rate is directly a function of the external field.

3.2.1 Spatial dynamics

Throughout, individual robots are assumed to move at constant speed v_0 by means of an active self-propulsion mechanism. For simplicity, we focus on one-dimensional systems of linear size L – generalizations to higher dimensions are commented on in Section 3.4. In one dimension, the dynamics of the robot is given by

$$\dot{x}(t) = v_0 s(t) + \sqrt{2D_0} \xi(t), \quad (3.1)$$

where $x(t)$ is the position of the robot at time t , v_0 denotes its active speed, D_0 is the bare diffusivity in the absence of active motion ($v_0 = 0$), $\xi(t)$ abbreviates white Gaussian noise and $s(t) \in \{-1, 1\}$ indicates the direction of active motion at time t . The temporal dynamics of $s(t)$ is controlled by a *navigation control system* (abbreviated NCS for short in the following), which we consider to operate with one internal Boolean variable that adopts two values. The dynamics of this internal Boolean variable is dictated by a closed Markov chain, see Figure 3.1 that illustrates several NCS motifs and the robot dynamics. Notice that the dynamics of the NCS is affected by the external field $c(x)$ via the c -dependency

of the transition rates. In all of these motifs, there is one particular transition leading to state 1 (depicted by a red, dashed arrow in Figure 3.1), which triggers a reversal of the driving engine and, thus, induces the inversion of the direction of active motion of the robot: $s(t) \rightarrow -s(t)$. Given a certain NCS motif, we want to understand the motility response of the robot to an external field $c(x)$. This is addressed in the following.

3.2.2 A didactic introduction

We start by studying the long-time behavior of the simplest possible scenario where the reorientation rate depends directly on the external field, i.e. there is no internal dynamics. Let us stress that we use this case as a didactic introduction to illustrate a series of fundamental concepts that will allow us to obtain a simplified long-time dynamics of NCS motifs of higher complexity (NCS motifs 1 and 2). Here, reversal events occur at a rate $\alpha[c]$, which depends on the external signal $c(x)$. The temporal evolution of the system can be expressed in terms of the probabilities $P^+(x, t)$ and $P^-(x, t)$ to find a robot at position x at time t moving to the right and to the left, respectively. The associated master equation [43] reads:

$$\partial_t P^+ = -v_0 \partial_x P^+ - \alpha[c] P^+ + \alpha[c] P^- + D_0 \partial_x^2 P^+, \quad (3.2a)$$

$$\partial_t P^- = v_0 \partial_x P^- - \alpha[c] P^- + \alpha[c] P^+ + D_0 \partial_x^2 P^-. \quad (3.2b)$$

By introducing the new variables $P(x, t) = P^+(x, t) + P^-(x, t)$ and $m(x, t) = P^+(x, t) - P^-(x, t)$, we recast equation (3.2) into

$$\partial_t P = -v_0 \partial_x m + D_0 \partial_x^2 P, \quad (3.3a)$$

$$\partial_t m = -v_0 \partial_x P + D_0 \partial_x^2 m - 2\alpha[c] m. \quad (3.3b)$$

The variable of interest is $P(x, t)$ representing the probability to find the robot at position x at time t . Since the local dynamics of $m(x, t)$ [equation (3.3b)] is faster than $P(x, t)$ [equation (3.3a)] and we are interested in the long-time behavior of the latter, we approximately set $\partial_t m \approx 0$, enabling us to express $m \approx -\frac{v_0}{2\alpha} \partial_x P$ to lowest order in spatial gradients. Inserting this expression into equation (3.3a) yields the following effective equation for the density:

$$\partial_t P = \partial_x \left[\left(D_0 + \frac{v_0^2}{2\alpha[c]} \right) \partial_x P \right] = -\partial_x \left[P \partial_x \left(\frac{v_0^2}{2\alpha[c]} \right) \right] + \partial_x^2 \left[P \left(D_0 + \frac{v_0^2}{2\alpha[c]} \right) \right]. \quad (3.4)$$

All details related to the reorientation dynamics were coarse-grained by deriving the effective scalar equation (3.4) for $P(x, t)$. This approach is valid as long as the mean distance traversed by a robot in between two transitions is shorter than the characteristic scales at which the external field varies.

3.2.3 Effective Langevin dynamics

Now we consider the inverse problem: starting with equation (3.4) for the density $P(x, t)$, we aim at finding a suitable Langevin equation in Ito's interpretation [43, 44] of the form

$$\dot{x} = f(x) + \sqrt{2D(x)} \xi(t), \quad (3.5)$$

whose associated Fokker-Planck equation

$$\partial_t P = -\partial_x [P f(x)] + \partial_x^2 [P D(x)] \quad (3.6)$$

for the evolution of the density $P(x, t)$ is structurally identical to equation (3.4)¹. This approach is advantageous in several regards. By obtaining an effective drift term $f(x)$ and an effective diffusion coefficient $D(x)$, we characterize the transport properties of the MR, encoding the details of the NCS in $f(x)$ and $D(x)$. The physical interpretation of $f(x)$ and $D(x)$ as drift and dispersion, respectively, results from the short-time solution of equation (3.6) for the propagator [45]

$$P(x, t+\tau | x', t) \simeq \frac{1}{\sqrt{4\pi D(x')\tau}} \exp\left\{-\frac{[x-x'-\tau f(x')]^2}{4D(x')\tau}\right\}$$

which determines the probability to find a robot at position x after a *short* observation time τ given that it was observed at position x' at time t . Notably, the propagator provides a direct way how to measure the mean local drift or bias $f(x)$ as well as the position dependent dispersion $D(x)$.

Knowing drift and diffusion coefficient, we can further determine whether a NCS motif lets the MR display a long-time motility response to the external field as follows. The steady state solution $P_s(x)$ of equation (3.6) for no-flux boundary conditions takes the form

$$P_s(x) = \frac{\mathcal{N}}{D(x)} \exp\left[\int_0^x dx' \frac{f(x')}{D(x')}\right] \quad (3.7)$$

with a normalization coefficient \mathcal{N} . In general, a MR is said *not* to exhibit a long-term response to a non-constant external field $c(x)$ if the stationary density *is constant*, i.e., $P_s(x) = P_0 = \text{const}$. Otherwise, the motif under consideration induces a response in the sense that the coupling to the external field increases or decreases the probability to find a robot in certain areas in space. The sign of the derivative of the stationary density distribution is determined by the simple criterion

$$\partial_x P_s(x) \gtrless 0 \quad \Leftrightarrow \quad f(x) \gtrless \partial_x D(x), \quad (3.8)$$

which follows directly from equation (3.7). A constant density $P_s(x)$ requires all x -dependencies in equation (3.7) to compensate each other. This implies the specific relation $f(x) = \partial_x D(x)$ between drift and diffusion. The nature and form of the response depends on the topology of the motif and the functional form of the rates; this is addressed further below.

Notice that it is possible to obtain a motility response to an external field $c(x)$ without involving biased motion. This is evident from equation (3.7): if $f(x) = 0$ and $D(x)$ is still a function of x , a nontrivial, stationary density profile will emerge. This kind of motility response is known in biology as *chemokinesis*. In contrast, directed motion requires a non-vanishing $f(x)$. In biology, a motility response involving a bias is known as *chemotaxis*.

¹The use of Stratonovich's interpretation leads to a different Fokker-Planck equation [44].

For the introductory example considered above, the comparison of equation (3.4) and equation (3.6) reveals

$$f(x) = \partial_x \left[\frac{v_0^2}{2\alpha[c(x)]} \right], \quad D(x) = D_0 + \frac{v_0^2}{2\alpha[c(x)]}, \quad (3.9)$$

which satisfies the above-mentioned relation, i.e. $f(x) = \partial_x D(x)$, implying $P_s(x) = P_0 = \text{const.}$ We observe that though the diffusion depends on x and the local drift $f(x)$ is nonzero and varies over space, there is no long-time motility response. Hence, the long-time density distribution is flat as noticed when memory kernels were introduced [9, 14]. Using the terminology of chemotaxis, one can summarize that chemotactic and chemokinetic part compensate each other in this case.

In the following, the powerful approach outlined above is used to express the motility response of MR in the form of equation (3.5) for each motif illustrated in Figure 3.1, where the specific form of $f(x)$ and $D(x)$ depends on the motif under consideration.

3.2.4 NCS motif 1: up- & downgradient motion

Now, we focus on a more complex scenario where the state of the navigation control system is given by an internal Boolean variable that adopts two values: 1 and 2. The possible transitions are $1 \rightarrow 2$ with rate $\alpha = \alpha[c]$ and $2 \rightarrow 1$ with rate $\beta = \beta[c]$. The latter transition triggers a reversal of the direction of active motion. This is motif 1 in Figure 3.1. Due to the presence of two internal states, we introduce four fields $P_i^+(x, t)$ and $P_i^-(x, t)$ with $i = \{1, 2\}$, which denote the probability to find a robot at position x at time t with internal state i moving to the right (+) and to the left (−), respectively. The temporal evolution of these fields is determined by the following master equation:

$$\partial_t P_1^+ = -v_0 \partial_x P_1^+ - \alpha[c] P_1^+ + \beta[c] P_2^- + D_0 \partial_x^2 P_1^+, \quad (3.10a)$$

$$\partial_t P_1^- = v_0 \partial_x P_1^- - \alpha[c] P_1^- + \beta[c] P_2^+ + D_0 \partial_x^2 P_1^-, \quad (3.10b)$$

$$\partial_t P_2^+ = -v_0 \partial_x P_2^+ - \beta[c] P_2^+ + \alpha[c] P_1^+ + D_0 \partial_x^2 P_2^+, \quad (3.10c)$$

$$\partial_t P_2^- = v_0 \partial_x P_2^- - \beta[c] P_2^- + \alpha[c] P_1^- + D_0 \partial_x^2 P_2^-. \quad (3.10d)$$

By introducing the change of variables $P_i = P_i^+ + P_i^-$ and $m_i = P_i^+ - P_i^-$, we recast equation (3.10) into two groups of equations for the densities $P_i(x, t)$,

$$\partial_t P_1 = -v_0 \partial_x m_1 - \alpha[c] P_1 + \beta[c] P_2 + D_0 \partial_x^2 P_1, \quad (3.11a)$$

$$\partial_t P_2 = -v_0 \partial_x m_2 + \alpha[c] P_1 - \beta[c] P_2 + D_0 \partial_x^2 P_2,$$

and for the differences $m_i(x, t)$,

$$\partial_t m_1 = -v_0 \partial_x P_1 - \alpha[c] m_1 - \beta[c] m_2 + D_0 \partial_x^2 m_1, \quad (3.11b)$$

$$\partial_t m_2 = -v_0 \partial_x P_2 + \alpha[c] m_1 - \beta[c] m_2 + D_0 \partial_x^2 m_2.$$

This seemingly innocent change of variables simplifies the problem substantially. If spatial derivatives in equations (3.11) were absent, equations (3.11a) would decouple completely from equations (3.11b). Further, we note that the eigenvalues associated to the local dynamics of equations (3.11a) are $\lambda_1 = 0$ and $\lambda_2 = -(\alpha + \beta)$, while the real parts of those associated to equations (3.11b) are both negative, i.e. $\Re[\lambda_3], \Re[\lambda_4] < 0$. The lesson

is: in the long-wavelength limit, there is one eigenvector whose temporal evolution is slow while the other three are fast. Accordingly, we can define a new set of four fields by linear combination of those in equations (3.11) in such a way that only one of those fields is slow. Due to number conservation, the total density $P = P_1 + P_2$, which is the primary quantity of interest, is the slow field ($\lambda_1 = 0$). In order to reduce equations (3.11) to the density dynamics, we request local equilibrium and take $\partial_t m_1 = \partial_t m_2 = 0$, allowing us to express all fields as function of P and spatial derivatives of it (see Appendix B.3 for further details). By keeping all terms up to second order spatial derivatives of the density P , we obtain an effective Fokker-Planck equation, cf. equation (3.6), where $f(x)$ and $D(x)$ adopt the form

$$f(x) = \frac{v_0^2}{2(\alpha + \beta)} \left[(\beta - \alpha) \partial_x \left(\frac{1}{\alpha} \right) + (\beta + \alpha) \partial_x \left(\frac{1}{\beta} \right) \right], \quad (3.12a)$$

$$D(x) = D_0 + \frac{v_0^2}{2} \cdot \frac{\alpha^2 + \beta^2}{\alpha\beta(\alpha + \beta)}. \quad (3.12b)$$

We highlight that $\alpha[c] = \beta[c]$ yields the relation $f(x) = \partial_x D(x)$ and, thus, the stationary density $P_s(x)$ would be a constant according to equation (3.7). In other words, we learn that we need to require $\alpha[c] \neq \beta[c]$ and at least one of the rates should depend on $c(x)$ in a nontrivial way in order to design robots that respond to the external field $c(x)$. In the spatially homogeneous case, the diffusion coefficient [equation (3.12b)] reduces to the expression, which was derived in Ref. [46].

The potentially simplest example that leads to upgradient motion of MR is $\alpha[c] \propto c(x)$ and $\beta[c] = \beta_0$, where β_0 is a constant, see Figure 3.3. It is interesting to observe that the robots move downgradient if we make the opposite choice, namely $\alpha = \text{const.}$ and $\beta \propto c(x)$. Thus, the previous discussion reveals how the field-dependence of the transition rates controls whether robots tend to move up- or downgradient.

Notably, both types of robots are entirely indistinguishable in spatially homogeneous environments; it is therefore *a priori* impossible to infer information on the type of response on the basis of measurements, which are performed in spatially homogeneous external fields, i.e. $c(x) = c_0 = \text{const.}$ at different levels of c_0 . To be concrete, consider the following gedankenexperiment: two types of robots, robots of type *A* with $\alpha[c] = 9c + 1$ and $\beta = 5$ and robots of type *B* with $\alpha = 5$ and $\beta[c] = 9c + 1$ exposed to the same external field $c(x)$; the scenario is depicted in Figure 3.3. If $c(x)$ corresponds to an homogeneous environment such that $c(x) = c_0$, with c_0 a constant, the diffusion coefficient and the mean rate of reversals are identical for both robot types; notice that the latter increases with the field value c_0 . One could easily be misled to think that robots tend to accumulate in those regions in space where the reversal rate is high, leading to an effective “trapping” of the robots in those regions. However, the distinct long-time behaviors of robots of type *A* and *B* provide clear evidence against this simplified picture. While robots of type *A* tend to move upgradient and accumulate close to $x = L$, robots of type *B* tend to move downgradient and accumulate close to $x = 0$, see Figure 3.3. Despite of this evident qualitative difference, both types exhibit a higher reversal rate close to $x = L$. This finding, i.e. the existence of the difference motility response for robots of type *A* and *B*, highlights how subtle and non-trivial is the impact of the NCS design on the long-time motility response of robots: by exchanging the functional form of the transitions from $1 \rightarrow 2$ and $2 \rightarrow 1$, we switch from up- to downgradient motion.

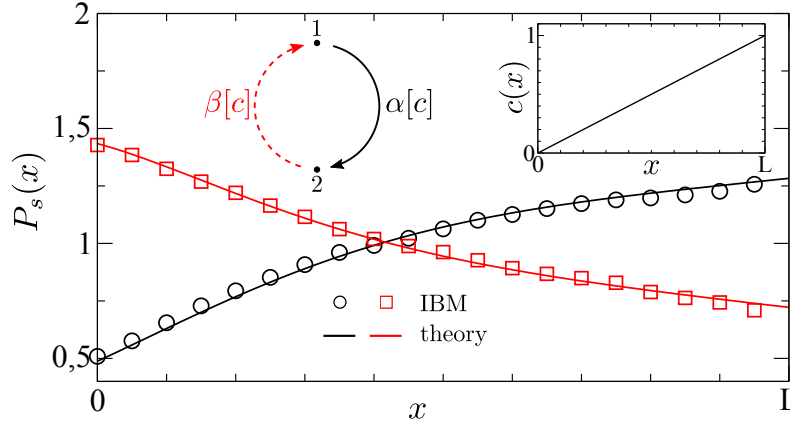


Figure 3.3 – The motility response of MR – controlled by NCS motif 1 as shown, cf. Figure 3.1 – to an external field $c(x) = x/L$ (see inset). The main figure illustrates the stationary probability distributions $P_s(x)$ for two variants of the internal robot dynamics. In the first case ($\alpha[c] = 9c + 1$, $\beta[c] = 5$), robots tend to accumulate upgradient in the long-time limit (circles). In contrast, robots accumulate on the opposite side if the two transitions are interchanged ($\alpha[c] = 5$, $\beta[c] = 9c + 1$) as shown by squares. Points denote **I**ndividual **B**ased **M**odel simulations (robot number $N = 10^4$). Lines correspond to the approximative analytical solution [equation (3.7)] where the respective functional forms of $f(x)$ and $D(x)$ were inserted [equations (3.12)]. Further parameters: $L = 1$, $v_0 = 0.01$, $D_0 = 0$; reflecting boundary conditions were implemented.

In addition, the previous analysis reveals that robots navigating by NCS motif 1 exhibit a motility response that involves both, directed motion and position dependent diffusion, i.e. it is neither purely chemotactic nor purely chemokinetic, but involves a combination of both, in the sense that the force $f(x)$ and the diffusion coefficient $D(x)$ are non-vanishing functions, which depend on the position via $c(x)$.

3.2.5 NCS motif 2: adaptation

We introduce NCS motif 2 (cf. Figure 3.1) to obtain robots whose motility response is purely chemotactic, with a bias resulting from $f(x)$ only. Adopting the terminology of bacterial chemotaxis, we call robots whose diffusion coefficient possesses an explicit dependency on $c(x)$, and thus on x *nonadaptive*, while those with a constant diffusion coefficient are referred to as *adaptive* robots. Following this nomenclature, we seek to create chemotactic, adaptive robots. Adaptive MR are characterized by the independence of their motility pattern from the intensity of external stimuli in spatially homogeneous environments – the diffusion coefficient, for example, is independent of the basis level of the external field. We insist that only NCS motif 2 can yield adaptive robots; motif 1 leads always to nonadaptive motility responses.

Motif 2 differs from motif 1 by the existence of a backward transition from state 2 to 1, which does not activate a reversal, and whose associated transition rate is $\gamma[c]$. Following the analytical procedure outline before, we first write the equations for P_i^\pm and perform the change of variables $P_i = P_i^+ + P_i^-$ and $m_i = P_i^+ - P_i^-$ for all i . Again, the dynamics of the m_i 's is fast and, furthermore, the system of equations for the P_i 's contains one fast and one slow mode allowing, eventually, to reduce the 4-dimensional system to the slow

dynamics of the density $P = P_1 + P_2$. Keeping derivatives up to second order, we obtain a Fokker-Planck equation of the form given by equation (3.6) where

$$f(x) = \frac{v_0^2}{2} \left[\partial_x \left(\frac{\alpha + \gamma}{\alpha\beta} \right) + \frac{(\beta + \gamma - \alpha)}{(\alpha + \beta + \gamma)} \partial_x \left(\frac{1}{\alpha} \right) \right], \quad (3.13a)$$

$$D(x) = D_0 + \frac{v_0^2}{2} \cdot \frac{\alpha^2 + (\beta + \gamma)^2 + 2\alpha\gamma}{\alpha\beta(\alpha + \beta + \gamma)}. \quad (3.13b)$$

In the limit $\gamma \rightarrow 0$, equations (3.12) are recovered. Again, if all rates are equal, $\alpha[c] = \beta[c] = \gamma[c]$, chemotactic and chemokinetic part are related by $f(x) = \partial_x D(x)$ and, thus, the stationary density $P_s(x)$ is constant.

So far, no restrictions have been imposed on the rates α , β , and γ . Consequently, the terms $f(x)$ and $D(x)$ given by equations (3.13) are generic for motif 2. In order to obtain adaptive robots, we want to choose these rates in such a way that $D(x)$ becomes independent of $c(x)$, while $f(x)$ still depends on it. With this idea in mind, we define

$$\alpha[c] = \frac{\beta_+ \beta_-}{\beta[c]}, \quad (3.14a)$$

$$\gamma[c] = \beta_+ + \beta_- - (\alpha[c] + \beta[c]). \quad (3.14b)$$

In order to ensure all rates to be positive, we further choose $\beta_- < \beta[c] < \beta_+$, where β_- and β_+ are positive constants. By inserting these rates into equation (3.13), we find

$$f(x) = -\frac{v_0^2}{\beta_+ + \beta_-} \partial_x (\ln \beta[c]) = \mu[c] \partial_x c(x), \quad (3.15a)$$

$$D(x) = D_0 + \frac{v_0^2}{2} \cdot \frac{\beta_+^2 + \beta_-^2}{\beta_+ \beta_- (\beta_+ + \beta_-)}. \quad (3.15b)$$

Notably, equation (3.15b) is structurally identical to equation (3.12b) for motif 1, however, by definition it is independent of $c(x)$. Further, we defined the response function

$$\mu[c] = -\frac{v_0^2}{\beta_+ + \beta_-} \cdot \frac{\partial_c \beta[c]}{\beta[c]}. \quad (3.16)$$

Notice that any function restricting the values of $\beta[c]$ between β_- and β_+ serves our purpose. This freedom of choice may be used to design $\mu[c]$ according to the desired response.

With the above choice of rates, we obtain purely adaptive, chemotactic robots whose directed motion is controlled by $f(x)$ only [cf. equation (3.15)]. In the absence of an external field gradient, $\partial_x c(x) = 0$, robots diffuse with a constant diffusion coefficient given by equation (3.15b) that is independent of the external field value. We notice that requesting $D = \text{const.}$ is equivalent to fixing the average and variance of the run-time distribution of the robots; accordingly, their behavior in homogeneous environments of different (constant) field values is microscopically indistinguishable.

3.3 Performing complex tasks

In the following, we discuss the possibility of designing MR to perform multiple complex tasks by playing with the response function $\mu[c]$, cf. equation (3.16), on the basis of NCS

motif 2. If we define $\beta[c]$ such that $\mu[c] > 0$ in the interval of interest of field values, robots move upgradient. As a consequence, they accumulate around the maxima of $c(x)$ in a complex landscape as shown in Figures 3.4a and b. This requires $\beta[c]$ to be a decreasing function of c . In addition, we have to make sure that $\beta[c]$ is bounded by $\beta \in (\beta_-, \beta_+)$. As an example, we consider $\beta[c] = A + B \tanh[(c - c^*)/w]$ where A and B are chosen such that $\beta[c \rightarrow 0] = \beta^+$ and $\beta[c \rightarrow \infty] = \beta^-$, and where w and c^* are constants. On the other hand: if robots are supposed to move downgradient to accumulate in the minima of $c(x)$, the response function has to be a decreasing function of the signal, $\mu[c] < 0$, and, thus, $\beta[c]$ should be an increasing function of c . This can be achieved by using the same functional form as before, but requesting $\beta[c \rightarrow 0] = \beta^-$ and $\beta[c \rightarrow \infty] = \beta^+$, cf. Figures 3.4a and b.

We can further design robots to accumulate at a given value c^* of the external field as shown in Figures 3.4c and d. For this task, we need $\mu[c]$ to be positive for $c < c^*$ and negative for $c > c^*$. Figure 3.4c illustrates this type of robot design: $\beta[c] = A - B\mathcal{N}(c; c^*, w^2)$ where $\mathcal{N}(c; c^*, w^2)$ is a Gaussian distribution centered at c^* and of variance w^2 . The coefficients A and B are chosen such that $\beta[c \rightarrow c^*] = \beta_-$ and $\beta[c \rightarrow 0] = \beta_+$.

As a final example, we study how robots chase a signal that moves at speed v as shown in Figures 3.4e to i. The analyzed scenario is analogous to recent bacterial chemotactic experiments performed with a moving chemoattractant signal [47]. For this purpose, the MR design for the detection of maxima is used, cf. the discussion of Figures 3.4a and b. As a signal, we use a Gaussian distribution that moves at a constant speed v (remember that robots move at constant speed v_0). There is a critical signal speed v_c above which the robots become decreasingly responsive. In the limit of high signal speeds ($v \gg v_c$), robots just diffuse around as they would do in an homogeneous field. We quantify the efficiency of robots by the deviation from the homogeneous distribution $\Delta \propto \int_0^L dx |P_s(x) - P_0|$, see Figure 3.4e, which is large if robots follow the moving signal and decreases to zero for non-responsive MR. Considering a simplified scenario, we derive a rough estimate of the crossover speed beyond which robots cannot follow the moving signal. The estimation is based on the idea of a quasi-stationary situation: the density distribution of robots should have relaxed into the stationary state before the signal has moved to ensure that robots can follow a dynamic signal. Imagine first a static field $c(x) = \bar{c} \exp[-(x - x_0)^2/(2h^2)]$, where x_0 and h are constants such that $f(x) = -\mu[c]c(x)(x - x_0)/h^2 = -\kappa \cdot (x - x_0)$; notice that h is a length-scale that characterizes the spatial extent of the gradient. Assuming that we can linearize around x_0 , we approximate $\kappa \approx \mu[\bar{c}]\bar{c}/h^2$ yielding a linear restoring force $f(x)$ as if it was coming from a harmonic potential. The characteristic relaxation time for an harmonic potential is κ^{-1} . The critical speed is now given by the product of the relaxation rate and a characteristic size of the signal; therefore, we estimate that robots can follow any signal that travels at a speed less or equal to

$$v_c = h \cdot \kappa \simeq \frac{\mu[\bar{c}]\bar{c}}{h}. \quad (3.17)$$

For the parameters used in the simulations shown in Figure 3.4, the critical speed yields $v_c \approx 3 \cdot 10^{-4}$, indicated by a red (dashed) line in Figure 3.4e.

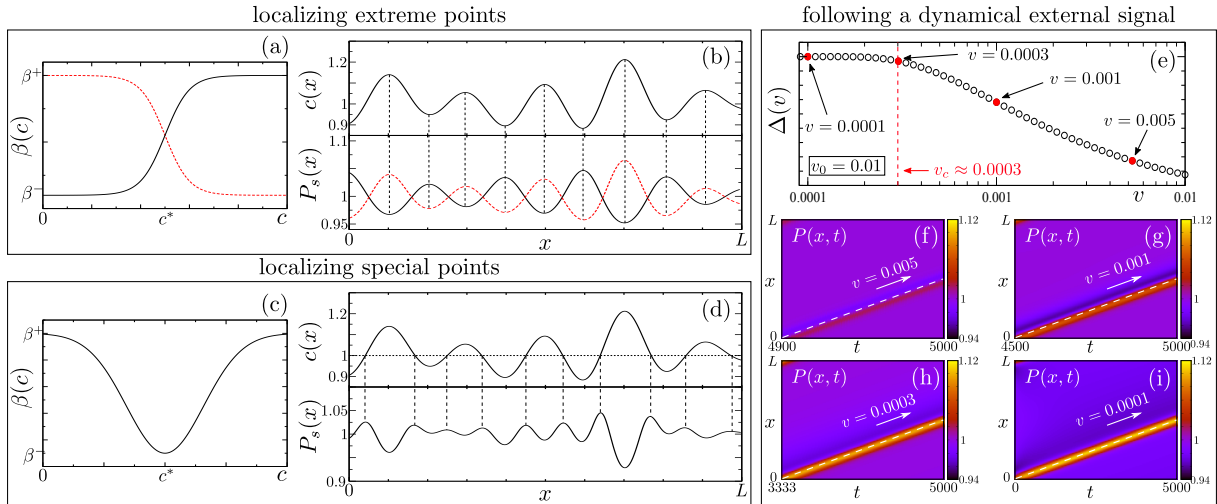


Figure 3.4 – Illustration of complex tasks performed by suitably tuned robots controlled by the adaptive NCS motif 2. The detection of maxima and minima in a complex landscape $c(x)$ is shown at the bottom of panel (b) [$c(x)$ is displayed at the top of panels (b) and (d)]. The corresponding functional dependencies of $\beta[c]$ are shown in (a): for increasing $\beta[c]$, minima are detected (black, solid curves) whereas robots accumulate around maxima for decreasing $\beta[c]$ (red, dashed lines). Moreover, the accumulation of robots around a preferred external field value [dotted line in (d)] is demonstrated for the functional dependence $\beta[c]$ shown in (c). As a third example, robots chasing for a moving signal (white, dashed line) are depicted in panels (e)-(i). Space-time plots (f)-(i) reveal that robots become less responsive to a moving signal above a critical speed v_c , estimated by equation (3.17), which is shown by a vertical red (dashed) line in (e). Further, the performance is quantified in (e) where Δ denotes the deviation of the robot density from the spatially homogeneous distribution. Parameters: $c^* = 1$, $w = 0.5$, $\beta^- = 1$, $\beta^+ = 10$, $v_0 = 0.01$, $L = 1$, $D_0 = 0$; see main text for the functional forms of the rate $\beta[c]$. Boundary conditions: reflecting in (b) and (d), periodic in (e)-(i).

3.4 Two & three-dimensional systems

The results obtained so far regarding the motility response of MR, based on a one-dimensional approach, hold true qualitatively in higher dimensions. Below, we briefly outline how biased motion of MR can be addressed in higher spatial dimensions within the same theoretical framework and provide a proof of principle. Technical details as well as a full account of the general dynamics in two as well as in three dimensions can be found in Appendix B.4 and Appendix B.5, respectively.

Two-dimensional case The equation of motion of a MR in two dimensions reads

$$\dot{\mathbf{r}}(t) = v_0 \hat{\mathbf{s}}[\varphi(t)] + \sqrt{2D_0} \boldsymbol{\xi}(t), \quad (3.18)$$

where $\mathbf{r}(t)$ is the position of a robot in two dimensions and $\hat{\mathbf{s}}[\varphi] = (\cos \varphi, \sin \varphi)$ is a unit vector pointing in the direction of motion parametrized by the polar angle φ . The polar angle may undergo a stochastic, rotational dynamics due to small-scale spatial heterogeneities, thermal fluctuations or temporal variations of the active driving force [48–

51]:

$$\dot{\varphi}(t) = \sqrt{2D_r} \eta(t). \quad (3.19)$$

The noise amplitude D_r parametrizes the persistence of trajectories during run phases, and $\eta(t)$ denotes white, Gaussian noise.

The internal robot dynamics, which controls abrupt changes of the direction of motion, is determined as before by a certain NCS. The reorientation of robots may be implemented in several ways: the new direction of active motion could be selected from a probability distribution of reorientation angles, representing, for example, a cone centered around the previous orientation or it could be chosen uncorrelated with respect to the previous direction of motion. The qualitative behavior is independent of this choice.

At first, we put forward a heuristic argument valid for low angular noise intensities to illustrate why the results derived so far based on one dimensional systems should hold in higher dimensions. Consider a robot equipped with some NCS, which controls the moments in time when the robot selects a new direction of motion from a certain probability distribution. The velocity of a robot may always be divided into its components parallel and perpendicular to the gradient orientation. The upgradient climbing speed v_{\perp} is a random variable, which changes at each reorientation event. Thus, the speed has to be rescaled to obtain an average climbing speed. Furthermore, not every reorientation inevitably leads to a reversal of the direction of active motion with respect to the gradient orientation. Upon reorientation, the projection of the new direction of active motion onto the gradient is positive or negative with equal probability ($p = 1/2$) if the direction of self-propulsion of a robot at each reorientation event is chosen randomly from the interval $[-\pi, \pi)$ in two dimensions; in general, there is a reversal probability p_r that the robot moves upgradient (downgradient) given that it was moving downgradient (upgradient) before the reorientation. These arguments indicate that it is always possible to come up with an effective one-dimensional description – in the sense of a projection – for the motion along the local gradient orientation, which is analogous to the problem considered in previous sections.

We now turn to a quantitative analysis of the problem in two dimensions. For the sake of concreteness, we formulate the problem for adaptive robots as discussed in Section 3.2, which are controlled by NCS motif 2, cf. Figure 3.1. In contrast to one dimension, where only two directions of motion (denoted by \pm) are possible, a continuum of orientations parametrized by the polar angle φ exists in two dimensions. Therefore, the probability densities $P_i^{(\pm)}(x, t)$ are replaced by the probability densities $\mathcal{P}_i(\mathbf{r}, \varphi, t)$ to find a robot at position \mathbf{r} in state i , moving into direction φ at time t . We introduced the new symbol $\mathcal{P}_i(\mathbf{r}, \varphi, t)$ in order to avoid confusion with the probability density

$$P_i(\mathbf{r}, t) = \int_{-\pi}^{\pi} d\varphi \mathcal{P}_i(\mathbf{r}, \varphi, t) \quad (3.20)$$

to find a robot at a certain position \mathbf{r} at time t in state i , independent of its direction of motion. Altogether, the full set of Master equations for robots controlled by NCS motif 2

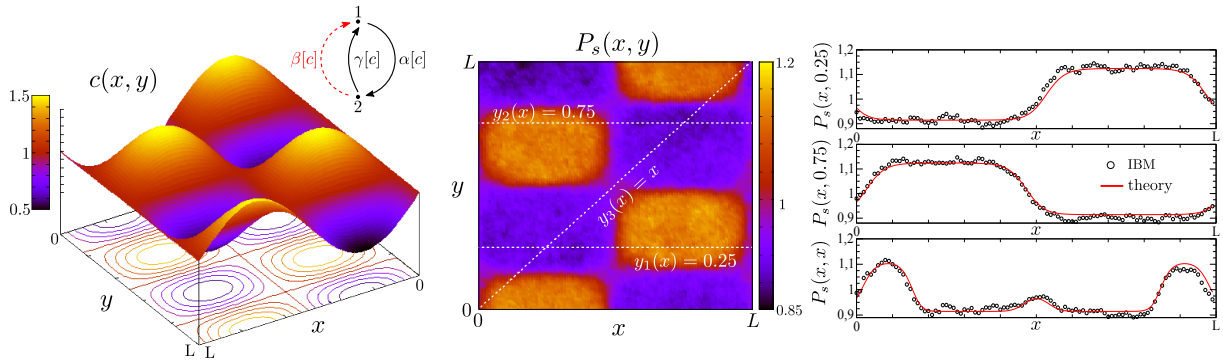


Figure 3.5 – Illustration of adaptive MR in two dimensions. In the left panel, the external field $c(\mathbf{r}) = 1 + 0.5 \sin(2\pi x) \cos(3\pi y)$ is shown. The middle panel represents the stationary probability density $P_s(\mathbf{r})$ obtained from **I**ndividual **B**ased **M**odel (IBM) simulations. On the right, several cross sections as indicated in the middle panel by white (dashed) lines are shown in comparison to predictions of the drift-diffusion approximation [equation (3.28)]. Model specification: upon reorientation, a robot chooses a new direction of motion from the uniform probability distribution $g(\varphi) = 1/(2\pi)$, such that $\mathcal{G} = 0$; adaptive NCS motif 2, cf. equations (3.14); $\beta[c]$ as shown in Figure 3.4 (red line) and the corresponding comments in the main text ($\beta_- = 1$, $\beta_+ = 10$). Other parameters: $L = 1$, $v_0 = 0.01$, $D_0 = 0$, $D_r = 0$, $N = 10^4$ robots in IBM simulations; reflecting boundary conditions were implemented.

in two dimensions reads

$$\begin{aligned} \partial_t \mathcal{P}_1(\mathbf{r}, \varphi, t) = & -v_0 \hat{\mathbf{s}}[\varphi] \cdot \nabla \mathcal{P}_1 + D_r \partial_\varphi^2 \mathcal{P}_1 + D_0 \Delta \mathcal{P}_1 - \alpha[c] \mathcal{P}_1 + \gamma[c] \mathcal{P}_2 \\ & + \beta[c] \int_{-\pi}^{\pi} d\varphi' g(\varphi - \varphi') \mathcal{P}_2(\mathbf{r}, \varphi', t), \end{aligned} \quad (3.21a)$$

$$\partial_t \mathcal{P}_2(\mathbf{r}, \varphi, t) = -v_0 \hat{\mathbf{s}}[\varphi] \cdot \nabla \mathcal{P}_2 + D_r \partial_\varphi^2 \mathcal{P}_2 + D_0 \Delta \mathcal{P}_2 - \left(\beta[c] + \gamma[c] \right) \mathcal{P}_2 + \alpha[c] \mathcal{P}_1. \quad (3.21b)$$

The details of the stochastic reorientation event, triggered by the NCS, are determined by the probability density function $g(\varphi)$. For unbiased reorientations, this function should be symmetric: $g(-\varphi) = g(\varphi)$.

Just as in one dimension, the total density dynamics is a slow quantity since it is locally conserved. It is therefore possible to reduce the set of Master equations to the Fokker-Planck equation

$$\partial_t P(\mathbf{r}, t) = -\nabla \cdot \left[\mathbf{f}(\mathbf{r}) P(\mathbf{r}, t) \right] + \Delta \left[D(\mathbf{r}) P(\mathbf{r}, t) \right] \quad (3.22)$$

for the density $P(\mathbf{r}, t) = \sum_i P_i(\mathbf{r}, t)$. Technically, the derivation follows the same logic as in one dimension. At first, the dynamics of the probability densities $P_i(\mathbf{r}, t)$, cf. equation (3.20), are derived by integration of equations (3.21) over the angular variable φ . Those equations are coupled to the flux, which is determined by the local order parameter

$$\mathbf{m}_i(\mathbf{r}, t) = \int d\varphi \hat{\mathbf{s}}[\varphi] \mathcal{P}_i(\mathbf{r}, \varphi, t) = \int d\varphi \begin{pmatrix} \cos \varphi \\ \sin \varphi \end{pmatrix} \mathcal{P}_i(\mathbf{r}, \varphi, t) \quad (3.23)$$

in two dimensions. The fields \mathbf{m}_i , which replace m_i from the one dimensional discussion, may again be adiabatically eliminated to obtain a reduced set of equations for the densities $P_i(\mathbf{r}, t)$. Finally, the density dynamics follows by assuming local equilibrium. Details on this derivation are summarized in Appendix B.4. For the example considered above, namely adaptive MR with NCS motif 2, one obtains the local drift

$$\mathbf{f}(\mathbf{r}) = -\Lambda_2 \cdot \nabla \left(\ln \beta[c] \right) \quad (3.24)$$

with the parameter-dependent prefactor

$$\Lambda_2 = \frac{v_0^2}{2} \cdot \frac{\beta_+ \beta_- (1 - \mathcal{G})}{(\beta_+ + \beta_-) \cdot \left[(\beta_+ + D_r) (\beta_- + D_r) - \beta_+ \beta_- \mathcal{G} \right]}. \quad (3.25)$$

Further, the constant diffusion coefficient reads

$$D = D_0 + \frac{v_0^2}{2} \cdot \frac{\beta_+^2 + \beta_-^2 + \beta_+ \beta_- (1 + \mathcal{G}) + D_r (\beta_+ + \beta_-)}{(\beta_+ + \beta_-) \cdot \left[(\beta_+ + D_r) (\beta_- + D_r) - \beta_+ \beta_- \mathcal{G} \right]}. \quad (3.26)$$

In these effective transport quantities, the mean cosine of the reorientation distribution $g(\varphi)$ was abbreviated by \mathcal{G} :

$$\mathcal{G} = \langle \cos \varphi \rangle = \int_{-\pi}^{\pi} d\varphi g(\varphi) \cos \varphi. \quad (3.27)$$

These results constitute a straightforward generalization of the results for the one-dimensional case, which can be seen by comparing the equations in question to equations (3.15) in the limit $D_r = 0$.

The stationary density distribution, i.e. the stationary solution of the Fokker-Planck equation (3.22), for adaptive MR in two dimensions reads

$$P_s(\mathbf{r}) = \frac{\mathcal{N}}{(\beta[c])^{\Lambda_2/D}}. \quad (3.28)$$

It is illustrated in Figure 3.5 together with a comparison to individual based model simulations.

Three-dimensional case For the sake of completeness, we finally consider MR in three spatial dimensions. Their transport characteristics turn out to be marginally different from those in two dimensions, as explained below. This implies in particular that all qualitative statements made above hold true in three dimensions as well. However, there are some technical complications as a consequence of the three dimensional motion regarding the implementation of angular fluctuations as well as the angular reorientation, which are explained below for this reason. Again, adaptive MR controlled by NCS motif 2 are considered for simplicity as an example. All details concerning the general dynamics of MR in three dimensions can be found in Appendix B.5. The dynamics in space for MR in three dimensions,

$$\dot{\mathbf{r}}(t) = v_0 \hat{\mathbf{s}} + \sqrt{2D_0} \boldsymbol{\xi}(t), \quad (3.29)$$

is unchanged with respect to previous cases. However, the orientation of the active driving force, determined by the unit vector $\hat{\mathbf{s}}$, has to be parametrized differently in three dimensions. One could, for example, use spherical coordinates $\hat{\mathbf{s}} = (\sin \theta \cos \varphi, \sin \theta \sin \varphi, \cos \theta)$, where $\theta \in [0, \pi]$ and $\varphi \in (-\pi, \pi)$. The angular dynamics for unbiased, orientational fluctuations reads then as follows:

$$\dot{\theta} = D_r \cot \theta + \sqrt{2D_r} \eta_\theta(t), \quad (3.30a)$$

$$\dot{\varphi} = \sqrt{2D_r} \csc \theta \eta_\varphi(t). \quad (3.30b)$$

For a derivation of these equations, see [52], and for a detailed discussion on Brownian motion in 3D we refer the reader to [53–57]. All interpretation of multiplicative noise terms in the angular dynamics [equation (3.30)] are equivalent in this particular case. From a technical point of view, it is, however, more convenient to use Cartesian coordinates for the director $\hat{\mathbf{s}} = (s_x, s_y, s_z)$, at least for analytical calculations.

Besides the continuous fluctuations of the direction of motion due to rotational diffusion [equation (3.30)], robots change the orientation of the active driving force in a discontinuous fashion each time that the NCS triggers one of this events: $\hat{\mathbf{s}}' \rightarrow \hat{\mathbf{s}}$. Given that the previous direction of motion was $\hat{\mathbf{s}}'$, a novel orientation $\hat{\mathbf{s}}$ is chosen from a transition probability density $g(\hat{\mathbf{s}}|\hat{\mathbf{s}}')$. Since reorientations are supposed to occur in an unbiased manner, the transition probability density $g(\hat{\mathbf{s}}|\hat{\mathbf{s}}')$ can only depend on the scalar product $\hat{\mathbf{s}} \cdot \hat{\mathbf{s}}'$. Further, the normalization of the director, $|\hat{\mathbf{s}}| = 1$, has to be preserved. One may, therefore, parametrize

$$g(\hat{\mathbf{s}}|\hat{\mathbf{s}}') = \frac{\delta(1 - |\hat{\mathbf{s}}|)}{2\pi} \mathcal{H}(\hat{\mathbf{s}} \cdot \hat{\mathbf{s}}'), \quad (3.31)$$

where $\mathcal{H}(\hat{\mathbf{s}} \cdot \hat{\mathbf{s}}')$ is the probability distribution function for the scalar product of the orientations just right before and after a reorientation event. Put differently, it denotes the probability density for the cosine of the angle ψ between the vectors $\hat{\mathbf{s}}$ and $\hat{\mathbf{s}}'$, i.e. $\cos \psi = \hat{\mathbf{s}} \cdot \hat{\mathbf{s}}'$.

The internal robot dynamics is independent of the spatial dimension. Therefore, the general structure of the Master equations, which describe the dynamics of MR, remains unchanged in three dimensions, but transport terms are adapted accordingly. For MR controlled by NCS motif 2, these Master equations are given by

$$\begin{aligned} \partial_t \mathcal{P}_1(\mathbf{r}, \hat{\mathbf{s}}, t) &= -v_0 \hat{\mathbf{s}} \cdot \nabla \mathcal{P}_1 + D_r \mathcal{L}[\mathcal{P}_1] + D_0 \Delta \mathcal{P}_1 - \alpha[c] \mathcal{P}_1 + \gamma[c] \mathcal{P}_2 \\ &\quad + \beta[c] \int d^3s g(\hat{\mathbf{s}}|\hat{\mathbf{s}}') \mathcal{P}_2(\mathbf{r}, \hat{\mathbf{s}}', t), \end{aligned} \quad (3.32a)$$

$$\partial_t \mathcal{P}_2(\mathbf{r}, \hat{\mathbf{s}}, t) = -v_0 \hat{\mathbf{s}} \cdot \nabla \mathcal{P}_2 + D_r \mathcal{L}[\mathcal{P}_2] + D_0 \Delta \mathcal{P}_2 - (\beta[c] + \gamma[c]) \mathcal{P}_2 + \alpha[c] \mathcal{P}_1, \quad (3.32b)$$

which is the analogue of equation (3.21) for the corresponding two-dimensional case: the convective term is replaced by its three dimensional equivalent, the reorientation distribution $g(\varphi)$ is replaced by $g(\hat{\mathbf{s}}|\hat{\mathbf{s}}')$ and the implementation of the director dynamics due to rotational noise has changed. The latter is determined in Cartesian coordinates by the operator

$$\mathcal{L}[\mathcal{P}_i] = \partial_{s_\mu} [2s_\mu \mathcal{P}_i] + \partial_{s_\mu} \partial_{s_\nu} [(\delta_{\mu\nu} - s_\mu s_\nu) \mathcal{P}_i], \quad (3.33)$$

where a sum over μ and ν is implicit. This parametrization is entirely equivalent to the angular representation [equations (3.30)], which can be verified by insertion of the parametrization of $\hat{\mathbf{s}}$ via spherical coordinates [52].

In the diffusive limit, i.e. if the external signal $c(\mathbf{r})$ varies weakly on spatial scales, which a robot traverses in between two reorientation events, a drift-diffusion approximation in the same spirit as in one and two spatial dimensions is feasible. The basic prerequisites of this derivation and its logic are analogous to the arguments put forward before; technical subtleties are summarized in Appendix B.5. It turns out that solely the speed and the angular noise intensity are rescaled by numerical factors, which depend on spatial dimensionality. The drift reads [cf. equation (3.24)]

$$\mathbf{f}(\mathbf{r}) = -\Lambda_3 \cdot \nabla \left(\ln \beta[c] \right) \quad (3.34)$$

in three dimensions, where the prefactor Λ_3 is structurally very similar to Λ_2 determined by equation (3.25) in two dimensions. Here, the prefactor Λ_3 is determined by

$$\Lambda_3 = \frac{v_0^2}{3} \cdot \frac{\beta_+ \beta_- (1 - \mathcal{G})}{(\beta_+ + \beta_-) \cdot \left[(\beta_+ + 2D_r) (\beta_- + 2D_r) - \beta_+ \beta_- \mathcal{G} \right]}. \quad (3.35)$$

Along similar lines, only a few numerical factors are replaced in the expression for the effective diffusion coefficient, which reads in three dimensions as follows:

$$D = D_0 + \frac{v_0^2}{3} \cdot \frac{\beta_+^2 + \beta_-^2 + \beta_+ \beta_- (1 + \mathcal{G}) + 2D_r (\beta_+ + \beta_-)}{(\beta_+ + \beta_-) \cdot \left[(\beta_+ + 2D_r) (\beta_- + 2D_r) - \beta_+ \beta_- \mathcal{G} \right]}. \quad (3.36)$$

Just as in two dimensions, the parameter \mathcal{G} denotes the mean cosine of the angle between the directors before and after the reorientation event. In three dimensions, it may be expressed by

$$\mathcal{G} = \langle \cos \psi \rangle = \int d^3s \hat{\mathbf{s}} \cdot \hat{\mathbf{s}}' g(\hat{\mathbf{s}}|\hat{\mathbf{s}}') = \int_{-1}^1 d(\cos \psi) h(\cos \psi). \quad (3.37)$$

The stationary probability density is thus determined by

$$P_s(\mathbf{r}) = \frac{\mathcal{N}}{(\beta[c])^{\Lambda_3/D}}. \quad (3.38)$$

for adaptive MR controlled by NCS motif 2.

Notably, the simple rescaling of speed and rotational diffusion described above is not a particularity of the example under consideration, but it is generally the only quantitative difference of the transport properties of MR in two and three dimensions. The proof of this result is sketched in Appendix B.5. In short, the behaviour of MR is qualitatively independent of the spatial dimension.

A comparison of **I**ndividual **B**ased **M**odel simulations and theoretical predictions in terms of the stationary probability density $P_s(\mathbf{r})$, as shown in Figure 3.6, serves as sanity check that the analytically obtained transport coefficients, drift [equation (3.34)] and diffusion [equation (3.36)], provide a reasonable description of the large-scale transport of MR in the diffusive limit.

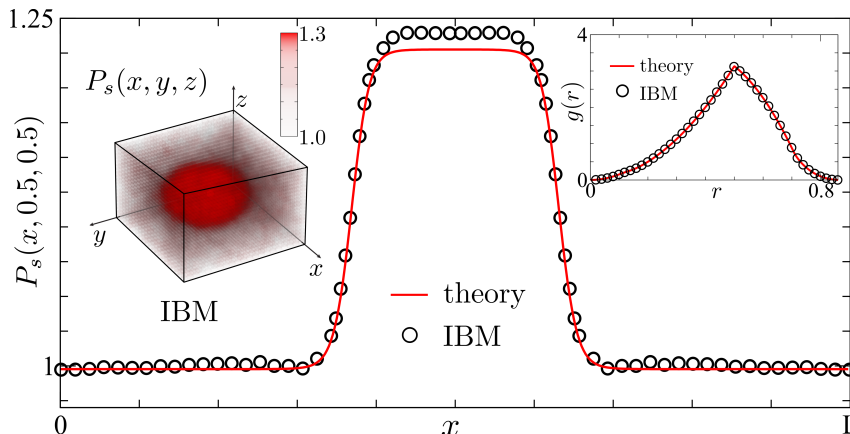


Figure 3.6 – Comparison of the stationary probability density $P_s(\mathbf{r})$ of MR controlled by NCS motif 2 as obtained from **I**ndividual **B**ased **M**odel (IBM) simulations and the corresponding drift-diffusion approximation, cf. equation (3.38), in three spatial dimensions. A Gaussian modulation is used as an external signal: $c(\mathbf{r}) = c_0 \left[1 + \varepsilon \exp\left(-\frac{|\mathbf{r}-\mathbf{r}_0|^2}{2\sigma^2}\right) \right]$. The data points in the main panel (IBM) were reconstructed from the radial distribution function $g(R) = \int d^3r P_s(\mathbf{r}) \delta(R - |\mathbf{r} - \mathbf{r}_0|)$ shown in the inset via division by the angular measure factor. The inset on the left represents a three-dimensional histogram of the position of MR, where the color code indicates the value of $P_s(\mathbf{r})$. The main panel is a cut of $P_s(\mathbf{r})$ along $\mathbf{r} = (x, 1/2, 1/2)^T$. Parameters: $c_0 = 1/2$, $\varepsilon = 2$, $\sigma = \sqrt{3/2}/10 \approx 0.12$, $\mathbf{r}_0 = (1/2, 1/2, 1/2)^T$. Further parameters as in Figure 3.5; reflecting boundary conditions have been used.

3.5 Tests with a real robot

We tested the concepts developed before in practice by assembling a macroscopic robot that operates with NCS motif 2 as defined above. The robot – a Lego Mindstorms EV3 shown in Figure 3.7a – was equipped with a single light sensor capable of reading light intensities, providing a signal \mathcal{S} in arbitrary units between 0 and 100 at the current position. A gray scale from black to white printed on paper (total length: 81 cm) was utilized as an external field [cf. the top panel of Figure 3.7c]. The robot possesses two synchronously steered motors in the front, each of which are connected to one wheel. A metallic roller in the back of the robot serves as a stabilization. For simplicity, we focused on the one-dimensional scenario: the robot was attached to a metallic rail to prevent turns, thereby ensuring straight trajectories.

Being a real-world system, the robot is naturally subjected to a series of fluctuations. Vibrations of the arm that connects the light sensor to the robot and, moreover, imperfections in the printed gray scale itself result in noisy measurements of the signal intensity \mathcal{S} . Furthermore, imperfect rotations of the wheels imply varying step lengths and, hence, lead effectively to noise in the particle position.

The robot was programmed in the LabVIEW based Lego Mindstorms EV3-software. The basic flowchart of the algorithm is shown in Figure 3.2. The temporal update is composed of a streaming and a signal processing step that are repeated continuously. The length of one streaming step was fixed to be $2/3$ of the wheel perimeter resulting in a

step length of approximately 11.7 cm. Afterwards, the signal strength \mathcal{S} is read from the sensor. Based on this measurement, the internal state is updated and, possibly, a reversal of the direction of rotation of the wheels is triggered. The transition rates $\alpha[c]$, $\beta[c]$, and $\gamma[c]$ are translated into probabilities $P_\alpha(\mathcal{S}) = b_+b_-/P_\beta(\mathcal{S})$, $P_\beta(\mathcal{S}) = b_+(b_-/b_+)^{\mathcal{S}/100}$ and $P_\gamma(\mathcal{S}) = b_+ + b_- - P_\alpha - P_\beta$ for the corresponding transitions, where $b_+ = 1$ and $b_- = 0.8$ was used.

In the following, we aim at testing the theoretical predictions at the level of exit probabilities. For this purpose, a single experimental run proceeds as follows: it is monitored whether a robot which was initially placed in the middle of the experimental setup reaches the left (black) or right (white) boundary of the system first. Once the robot touched one of the boundaries, the experiment is stopped and repeated. In total, $N = 40$ realizations were recorded. In $n = 28$ cases, the robot left the system via the right boundary. A typical trajectory for an exit on the right boundary is displayed in Figure 3.7c. See also the Supplemental Material of our PRE publication online for a corresponding movie ².

Based on this experimental result, we first test the null hypothesis that the robot performed just an unbiased random walk. The exit probability on the right side of the system for a single experimental run should therefore be $\Gamma = 0.5$. The probability to observe n exits on the right, given N realizations in total, is determined by the Binomial distribution

$$B_N(n|\Gamma) = \binom{N}{n} \Gamma^n (1 - \Gamma)^{N-n}. \quad (3.39)$$

This distribution is shown for $N = 40$ and $\Gamma = 0.5$ in Figure 3.7b by black circles. The total probability to observe $n = 28$ exits to the right of the system or a more extreme result than this is determined by the tails of the Binomial distribution. It thereby constitutes the p -value under the null hypothesis *the robot performs an unbiased random walk* [58]. In the case under consideration, we obtain a p -value of approximately 0.017. Accordingly, the null hypothesis may be discarded based on the standard significance level $\alpha = 0.05$. In short, there is considerable statistical significance that the motion of the robot is biased due to the NCS at work.

The NCS was implemented such that the robot tends to move towards brighter areas in terms of the gray value and, thus, we expect the number of exits to the right to be larger than to the left. Simulations of the corresponding process provide the prediction that the probability to touch the right boundary first is $\Gamma = 0.65(1)$. The Binomial distribution $B_{40}(n|\Gamma)$ for this Γ -value is represented by red squares in Figure 3.7b. The experimentally observed result ($n = 28$) is indicated by a blue, vertical line. Apparently, the likelihood for the observed result given $\Gamma = 0.65$ is higher than for the random walk:

$$B_{40}(n = 28|\Gamma = 0.65) > B_{40}(n = 28|\Gamma = 0.5). \quad (3.40)$$

Based on the Akaike information criterion [59], we infer that the theoretically predicted value $\Gamma = 0.65$ is considerably more likely than the random walk hypothesis corresponding to $\Gamma = 0.5$.

Finally, we specify the last statements regarding the likelihood of certain Γ -values given the experimental observation. Using the Bayesian theorem [60], the following expression

²See Supplemental Material at <https://journals.aps.org/pre/supplemental/10.1103/PhysRevE.97.042604> for movies.

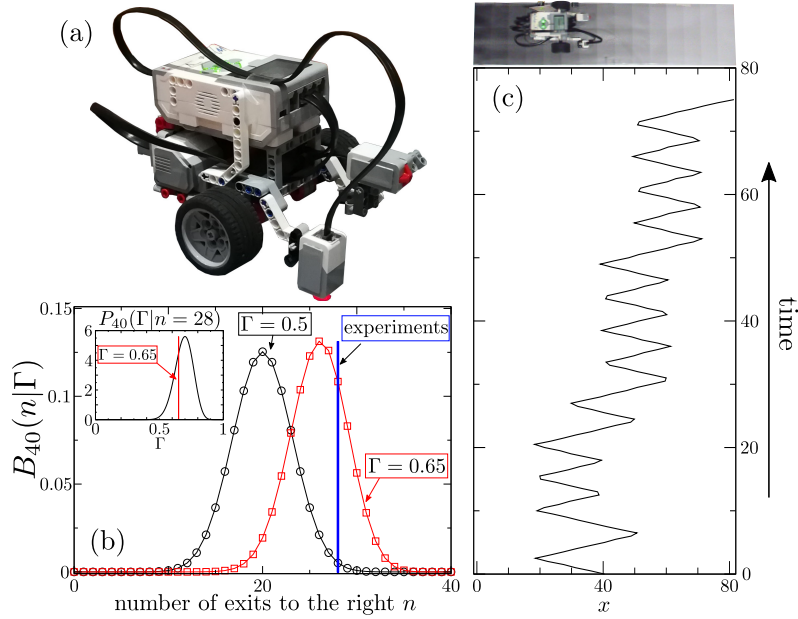


Figure 3.7 – (a) A photo of the robot, a Lego Mindstorms EV3. (b) Binomial distribution $B_{40}(n|\Gamma)$ determining the probability that the robot leaves the system n times via the right boundary in 40 realizations of the experiment, whereby the robot was initially placed at the center of the system, given that the probability for the same event in one realization is Γ , cf. equation (3.39). The black circles correspond to an unbiased random walker ($\Gamma = 0.5$), the red squares show the Binomial distribution for the theoretically predicted value ($\Gamma = 0.65$). The experimentally observed situation – in $n = 28$ cases the robot touched the right boundary first – is indicated by a vertical blue line. A representative trajectory is shown in panel (c), on top of which the robot is depicted moving on the printed gray scale. The probability distribution $P_{40}(\Gamma|n = 28)$ for Γ given the experimental result ($n = 28$), inferred from the Bayesian theorem [equation (3.41)], is shown as an inset of panel (b); the experimental observation is in line with the theoretical prediction.

for the probability distribution $P_N(\Gamma|n)$ for Γ given a certain number n of exits to the right out of N total experimental realizations is deduced:

$$P_N(\Gamma|n) = \frac{B_N(n|\Gamma) \mathcal{P}(\Gamma)}{\int_0^1 d\Gamma' B_N(n|\Gamma') \mathcal{P}(\Gamma')}. \quad (3.41)$$

In the equation above, $\mathcal{P}(\Gamma)$ determines the prior knowledge (before the experiment) about the probability distribution of Γ . Here, we assume a uniform prior, i.e. $\mathcal{P}(\Gamma) = 1$ for $\Gamma \in [0, 1]$ and zero otherwise. The probability distribution $P_{40}(\Gamma|n = 28)$, which is relevant for the experimental result, is shown as an inset in Figure 3.7. Apparently, the distribution is shifted towards the right implying that there is a drift towards the right boundary as expected. The resulting distribution $P_{40}(\Gamma|n = 28)$ possesses a mean and standard deviation of $\bar{\Gamma} = 0.69(7)$, which is well in line with the theoretical expectation.

In summary, the experimental results provide an empirical demonstration that the proposed navigation algorithm, which is simple to implement in a real robot, yields a

directed, nontrivial motility response as predicted by theoretical considerations, which is, notably, robust with respect to fluctuations.

3.6 Summary & perspectives

This study provides a solid proof-of-concept, including analytical derivations and a practical implementation, that it is possible to design particles that are capable of navigating through complex dynamical external fields in any spatial dimension – performing local measurements only – without making use of internal continuous variables to store previous measurements of the external field. The novel navigation strategies proposed and analyzed here are fundamentally different from previous bacterial chemotaxis models (see Sec. 3 for a detailed comparison). It requires that the robots possess a minimum of two internal states to exhibit non-trivial, persistent motility responses such as migration towards minima or maxima of the external field or even surfing at a desired field value in a complex, dynamical landscape. Transitions between these two internal states are dictated by a closed Markov chain, with transition rates that depend only on the local, instantaneous value of a given external field $c(\mathbf{x})$. This implies that the internal dynamics of the particles is such that fixed points are excluded. In summary, we have shown here that robots with such a minimal navigation control system, where the internal state can be stored in single Boolean variable, i.e. in 1 bit, are able to explore complex information landscapes.

Furthermore, we have shown that the proposed minimalistic navigation strategies can be efficiently implemented in real macroscopic robots. However, the main interest of conceiving navigation algorithms with limited memory storage capacity as the ones proposed here is to pave the way to engineer miniature, micrometer-size robots in a near future. Miniaturizing robotic systems as the one used in Sec. 3.5 is a major technological challenge [35, 36]. Our study does not provide a recipe how to combine the existing micrometer-size actuators, sensors, and switches to produce the proposed Markovian robots, which is certainly beyond the scope of this basically theoretical work. Nevertheless, the developed concepts may serve as guiding principles to design autonomous, tiny robots capable of displaying complex motility behaviors by identifying the minimum requirements to navigate with limited memory storage capacity.

Finally, extension of this initial study including more complex, biologically motivated motifs with a larger number of internal states may help to elucidate the navigation strategies of some microorganisms [61–64]. Studying ensembles of interacting robots as those studied in [65], operating with the here-proposed navigation algorithms is another promising research direction that may unveil cheap and efficient ways to obtain complex, self-organized collective behavior of autonomous, self-propelled agents.

Chapter 4

Intermittent Collective Behavior: a three state story

Contents

4.1	The three state model	54
4.2	Mean field	55
4.2.1	Recruiting term	55
4.2.2	Inhibitory term	59
4.2.3	Parameter diagram using both terms	62
4.3	Stochastic system	64
4.3.1	The Collective Clock Approximation	66
4.3.2	The Metaparticle Clock Approximation	68
4.4	Numerical comparison of CCA and MCA with IBM simulations	70
4.5	Summary & perspectives	71

In this chapter we study the three state model motivated by the experimental observations in the small groups of gregarious animals, presented in Chapter 2, Section 2.2, equation (2.9) in a slightly simplified way. To simplify the notation, we use generic names for the states, namely A , B and C . First, we focus on studying the time evolution of three collective variables. We call them $n_A(t)$, $n_B(t)$ and $n_C(t)$ and represent the number of particles in each of the three states. We study the dynamics at the mean field level and, thus, knowing the dynamics of the system means knowing the time evolution of $n_A(t)$, $n_B(t)$ and $n_C(t)$. Since particles are conserved, i.e.:

$$n_A(t) + n_B(t) + n_C(t) = N \quad \forall t \geq 0, \quad (4.1)$$

there are only two of these variables that are independent. Without loss of generality, we can assume that the independent variables are $n_A(t)$ and $n_B(t)$. If we plot $n_A(t)$ vs. $n_B(t)$, then the dynamics of the system is confined in a right-angled triangle with catheti of size N and hypotenuse of size $\sqrt{2}N$, as shown in Figure 4.1b.

This chapter is going to be organized as follows. In the first part we study the mean field dynamics of a system of N interacting particles by analyzing the temporal evolution

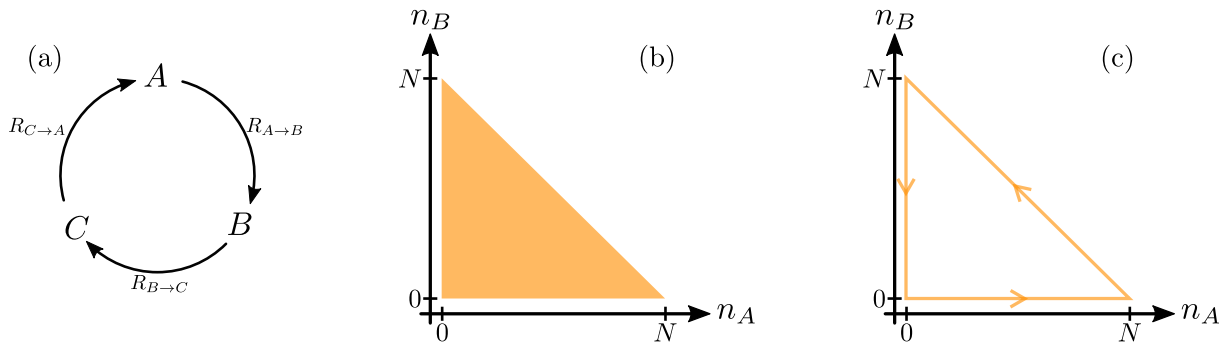


Figure 4.1 – (a) The three possible transition rates between the three states A , B and C . (b) Scheme to visualize the triangular region (highlighted in orange) that confines the dynamics of the system in the (n_A, n_B) space $\forall t \geq 0$. (c) Dynamics of a special case that is well described by the **Collective Clock Approximation** and **Metaparticle Clock Approximation**.

of $n_A(t)$ and $n_B(t)$. We show that Saddle Node and Hopf bifurcations appear when we vary the parameters of the system. We characterize these bifurcations in terms of the system parameters. This mean field study results to be vital to understand what happens in the complete stochastic system.

In the second part of this chapter we introduce two general concepts that we call **Collective Clock Approximation** (CCA) and **Metaparticle Clock Approximation** (MCA). We explain how to use these ideas to get analytical expressions that describe the temporal dynamics of the complete stochastic system. We study the accuracy of these two approximations by comparing the analytical expressions obtained using the CCA and MCA with **Individual Based Model** (IBM) simulations. By construction, the CCA and the MCA can be generalized to describe any kind of highly synchronized system of particles.

4.1 The three state model

In this case, the **Internal Control System** (ICS) of each particle has three states and three transition rates that define the time evolution of the internal variable $q_i(t)$ of each particle, as shown in Figure 4.1a. The three transition rates between the states are equal and of the form:

$$R_{i \rightarrow j}(n_i, n_j) = \frac{n_j^\beta + \omega}{n_i^\gamma}, \quad (4.2)$$

with $n_i(t)$ the number of particles in state $i \in [A, B, C]$. In (4.2), β , γ and ω are the system parameters that play a crucial role on the dynamics of the system. Notice that the interaction of particles is present only at the level of the transition rates (4.2). We assume that the particles have access to the values $n_A(t)$, $n_B(t)$ and $n_C(t)$ during the whole time evolution. In simpler words, “all particles see each other” and can identify the value of the internal variable of all their neighbours for all times. The master equation for the

probability $P(n_A, n_B, n_C; t)$ of finding a given configuration (n_A, n_B, n_C) at time t is:

$$\begin{aligned} \partial_t P(n_A, n_B, n_C; t) = & - \left(n_A R_{A \rightarrow B}(n_A, n_B) + n_B R_{B \rightarrow C}(n_B, n_C) \right. \\ & \left. + n_C R_{C \rightarrow A}(n_C, n_A) \right) P(n_A, n_B, n_C; t) \\ & + (n_A + 1) R_{A \rightarrow B}(n_A + 1, n_B - 1) P(n_A + 1, n_B - 1, n_C; t) \\ & + (n_B + 1) R_{B \rightarrow C}(n_B + 1, n_C - 1) P(n_A, n_B + 1, n_C - 1; t) \\ & + (n_C + 1) R_{C \rightarrow A}(n_C + 1, n_A - 1) P(n_A - 1, n_B, n_C + 1; t). \end{aligned} \quad (4.3)$$

The master equation (4.3) defines uniquely our stochastic system.

4.2 Mean field

First, we study what happens to the system at the mean field level. The analysis of the dynamics of the system is going to be performed in three steps. First, we analyze the role of parameter β alone and, thus, we study the limit case $\gamma \rightarrow 0$ that we call the *recruiting term* (RT):

$$\lim_{\gamma \rightarrow 0} R_{i \rightarrow j}(n_i, n_j) = (n_j^\beta + \omega). \quad (4.4)$$

Second, we analyze the role of γ and to do so we study the limit case $\beta \rightarrow 0$ that we call *inhibition term* (IT):

$$\lim_{\beta \rightarrow 0} R_{i \rightarrow j}(n_i, n_j) = \frac{1 + \omega}{n_i^\gamma} = \frac{\tilde{\omega}}{n_i^\gamma}, \quad (4.5)$$

where $\tilde{\omega} = 1 + \omega$. Last, we study both terms at the same time, i.e.: the whole dynamics given by rates of the form (4.2).

To obtain the mean field equations we have to use the master equation (4.3) to obtain the evolution equations for our average independent variables:

$$\langle n_A(t) \rangle = \int_0^\infty dn_C \int_0^\infty dn_B \int_0^\infty dn_A \left(n_A P(n_A, n_B, n_C; t) \right), \quad (4.6)$$

$$\langle n_B(t) \rangle = \int_0^\infty dn_C \int_0^\infty dn_B \int_0^\infty dn_A \left(n_B P(n_A, n_B, n_C; t) \right) \quad (4.7)$$

In the rest of this section we will abuse of the notation and we will call the average variables simply $\langle n_A(t) \rangle = n_A(t)$ and $\langle n_B(t) \rangle = n_B(t)$.

4.2.1 Recruiting term

In this case, the transition rates are of the form:

$$R_{i \rightarrow j}(n_i, n_j) = (n_j^\beta + \omega). \quad (4.8)$$

The mean field equations result to be:

$$\begin{aligned}\dot{n}_A(t) &= -\left(n_B^\beta(t) + \omega\right)n_A(t) + \left(n_A^\beta(t) + \omega\right)\left(N - n_A(t) - n_B(t)\right) \\ &= f_1(n_A, n_B) \\ \dot{n}_B(t) &= -\left((N - n_A(t) - n_B(t))^\beta + \omega\right)n_B(t) + \left(n_B^\beta(t) + \omega\right)n_A(t) \\ &= f_2(n_A, n_B)\end{aligned}\tag{4.9}$$

The only fixed point of (4.9) is $\hat{n}_A = \hat{n}_B = \hat{n} = N/3$ for all values of $\beta > 0$. To study the instabilities around this fixed point we make small perturbations of the form $n_A(t) = \hat{n} + \epsilon_A(t)$ and $n_B(t) = \hat{n} + \epsilon_B(t)$. To check the stability of the fixed point we can stay at first order of perturbations, which gives the following linear system:

$$\begin{aligned}\dot{\epsilon}_A(t) &= \left(\hat{n}^\beta(\beta - 2) - 2\omega\right)\epsilon_A(t) - \left(\hat{n}^\beta(\beta + 1) + \omega\right)\epsilon_B(t) \\ \dot{\epsilon}_B(t) &= \left(\hat{n}^\beta(\beta + 1) + \omega\right)\epsilon_A(t) + \left(\hat{n}^\beta(2\beta - 1) - \omega\right)\epsilon_B(t).\end{aligned}\tag{4.10}$$

To get (4.10) we used the binomial series:

$$(1 + x)^b = \sum_{k=0}^{\infty} \binom{b}{k} x^k = 1 + bx + \frac{b(b-1)}{2!}x^2 + \dots\tag{4.11}$$

The eigenvalues of (4.10) are:

$$\lambda_{1,2} = -\frac{3}{2}\left(\frac{\omega}{\hat{n}^\beta} - \beta + 1\right) \pm i\frac{\sqrt{3}}{2}\left(\frac{\omega}{\hat{n}^\beta} + \beta + 1\right)\tag{4.12}$$

Knowing that $\omega > 0$ and $\beta > 0$, then the sign of the real part of the eigenvalues $\lambda_{1,2}$ is determined only by the condition:

$$\Re(\lambda_{1,2}) \begin{matrix} \leq \\ \geq \end{matrix} 0 \quad \text{if} \quad 0 \begin{matrix} \leq \\ \geq \end{matrix} \frac{\omega}{\hat{n}^\beta} - \beta + 1.\tag{4.13}$$

Thus, the critical value of β for which the stability changes satisfies the condition:

$$\frac{\omega}{\hat{n}^{\beta_c}} - \beta_c + 1 = 0.\tag{4.14}$$

For $\omega \ll 1$ we get that $\beta_c \approx 1$. This result tells us that for values where $\beta < \beta_c$, the fixed point is stable and for $\beta > \beta_c$ the fixed point changes stability.

To get more information regarding the case $\beta > \beta_c$ we performed the numerical integration of (4.9) using a classical 4th order Runge-Kutta method. For values of $\beta > \beta_c$, we noticed that the dynamics of the system reaches a stable periodic solution known as limit cycle, as shown in the left panel of Figure 4.2 for $\beta = 1.2$. Thus, this tells us that we can pass from having one stable fixed point to one unstable fixed point and one stable limit cycle. In dynamical systems, this is called a supercritical Hopf bifurcation. To

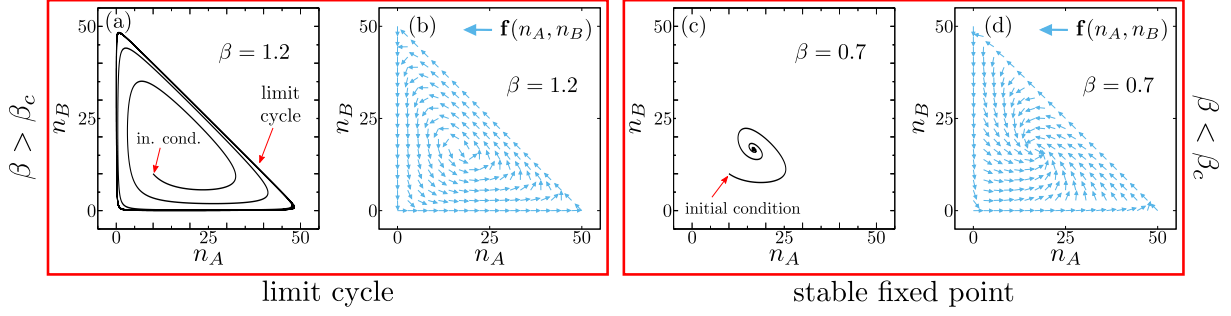


Figure 4.2 – The two qualitatively different behaviors of the recruiting term are shown. A limit cycle appears for values of $\beta > \beta_c$. (a) The dynamic evolution of the system is shown for $\beta = 1.2$ using as initial condition: $n_A(t = 0) = 10$ and $n_B(t = 0) = 10$. It reaches a limit cycle. (b) The drift $\mathbf{f}(n_A, n_B)$ given by the mean field equations in (4.9) is shown for the same value of β . (c) and (d) contain the same information but for the case $\beta < \beta_c$ where there exists only one stable fixed point. The system parameters are $N = 50$ and $\omega = 0.1$.

characterize this bifurcation, and particularly to characterize the limit cycle, we have to study the perturbations at higher orders. The resulting high order system is:

$$\begin{aligned}
\dot{\epsilon}_A(t) &= \left(\hat{n}^\beta (\beta - 2) - 2\omega \right) \epsilon_A(t) - \left(\hat{n}^\beta (\beta + 1) + \omega \right) \epsilon_B(t) + \left(\hat{n}^{\beta-1} \frac{\beta(\beta-3)}{2} \right) \epsilon_A^2(t) \\
&\quad - \left(\hat{n}^{\beta-1} \frac{(\beta-1)\beta}{2} \right) \epsilon_B^2(t) - \left(\hat{n}^{\beta-1} \beta(\beta-3) \right) \epsilon_A(t) \epsilon_B(t) \\
&\quad - \left(\hat{n}^{\beta-2} \frac{(\beta-1)\beta}{2} \right) \left(\epsilon_A^3(t) + \epsilon_A^2(t) \epsilon_B(t) + \epsilon_A(t) \epsilon_B^2(t) \right) \\
\dot{\epsilon}_B(t) &= \left(\hat{n}^\beta (\beta + 1) + \omega \right) \epsilon_A(t) + \left(\hat{n}^\beta (2\beta - 1) - \omega \right) \epsilon_B(t) \\
&\quad - \left(\hat{n}^{\beta-1} \frac{(\beta-1)\beta}{2} \right) \epsilon_A^2(t) + \left(\hat{n}^{\beta-1} \beta \right) \epsilon_B^2(t) - \left(\hat{n}^{\beta-1} \beta(\beta-3) \right) \epsilon_A(t) \epsilon_B(t) \\
&\quad - \left(\hat{n}^{\beta-2} \frac{(\beta-1)\beta}{2} \right) \left(\epsilon_A^2(t) \epsilon_B(t) + \epsilon_A(t) \epsilon_B^2(t) + \epsilon_B^3(t) \right).
\end{aligned} \tag{4.15}$$

To get (4.15) we used again the binomial series (4.11). The non-linear system (4.15) is complicated to study and one of the main causes is that the limit cycles are not perfect circles but ellipses, as observed in detail in Figure 4.3. To simplify this study, we make a change of our original variables $n_A(t)$ and $n_B(t)$ and get new variables $\tilde{n}_A(t)$ and $\tilde{n}_B(t)$ where the limit cycle is a perfect circle. To find the new variables, it suffices to make a rotation of $-\pi/4$ and multiply $n_B(t)$ by a factor of $\kappa_1 = 1/\sqrt{3}$. We can write the change of variables in matricial form as:

$$\begin{pmatrix} \tilde{n}_A(t) \\ \tilde{n}_B(t) \end{pmatrix} = \begin{pmatrix} \cos\left(\frac{\pi}{4}\right) & \kappa_1 \sin\left(\frac{\pi}{4}\right) \\ -\sin\left(\frac{\pi}{4}\right) & \kappa_1 \cos\left(\frac{\pi}{4}\right) \end{pmatrix} \begin{pmatrix} n_A(t) \\ n_B(t) \end{pmatrix} \tag{4.16}$$

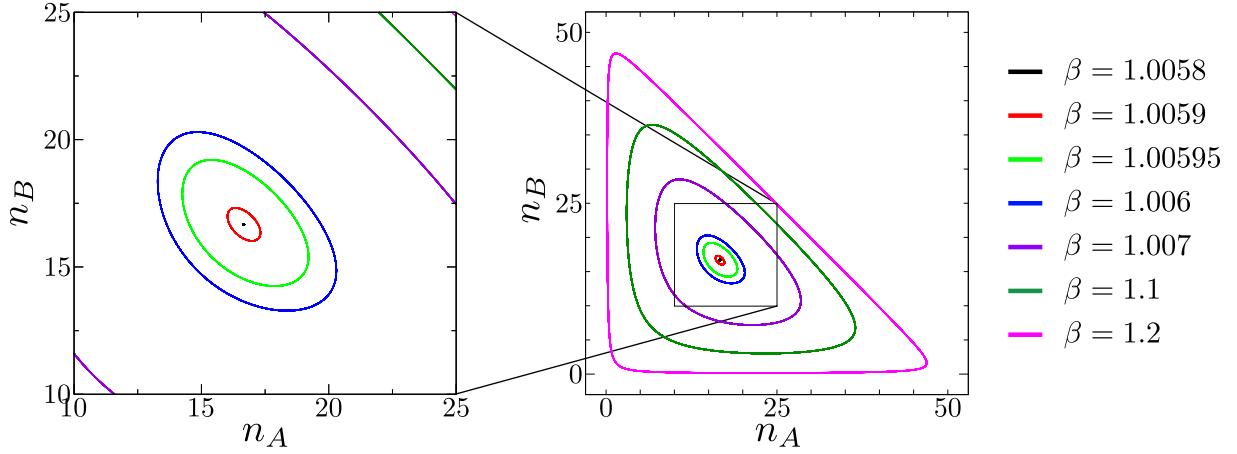


Figure 4.3 – Various limit cycles obtained by numerically integrating the equations in (4.9). For the integration, we used a classical 4th order Runge-Kutta method. We show the limit cycles for various values of parameter β . We notice that for small values of β the limit cycle is an ellipse, which is rotated with respect with the variables n_A and n_B . For increasing values of β , the radius also increases until (almost) reaching the borders of the triangle. The system parameters are in this case is $N = 50$ and $\omega = 0.1$.

Given that the time dynamics of the system is in the plane, we can suppose that the two new variables are the real and imaginary parts of a complex variable

$$z(t) = \tilde{n}_A(t) + i\tilde{n}_B(t) = r(t) e^{i\Phi(t)}. \quad (4.17)$$

The time derivative of the radial function $r(t)$ is:

$$\dot{r}(t) = \frac{1}{r} \Re\left(\dot{z}(t) \bar{z}(t)\right), \quad (4.18)$$

with $\bar{z}(t)$ the complex conjugate of $z(t)$ and $\Re(\cdot)$ the real part of (\cdot) . Using the new variables in (4.16) and substituting them in equation (4.15) to calculate (4.18), we obtain the normal form of the Hopf bifurcation:

$$\dot{r} = r \left[\frac{12}{9} \left(\hat{n}^2 - \frac{\omega}{\beta - 1} \hat{n}^{2-\beta} \right) - r^2 \right]. \quad (4.19)$$

The dependence of the radius R_0 of the limit cycle on parameters N , β and ω is then:

$$R_0(\beta, \omega, N) = \sqrt{\frac{12}{9} \left[\left(\frac{N}{3} \right)^2 - \left(\frac{N}{3} \right)^{2-\beta} \frac{\omega}{\beta - 1} \right]} \quad \text{for } \beta > \beta_c. \quad (4.20)$$

The frequency of rotation \mathcal{F} of the limit cycle is also known. It is in fact the imaginary part of the eigenvalues $\lambda_{1,2}$ given in (4.12):

$$\Im(\lambda_{1,2}) = \mathcal{F}(\beta, \omega, N) = \frac{\sqrt{3}}{2} \left(\frac{\omega}{(N/3)^\beta} + \beta + 1 \right) \quad \text{for } \beta > \beta_c, \quad (4.21)$$

with $\Im(\cdot)$ the imaginary part of (\cdot) . Plots of R_0 and \mathcal{F} are shown in Figure 4.4 and are valid for $\beta > \beta_c$.

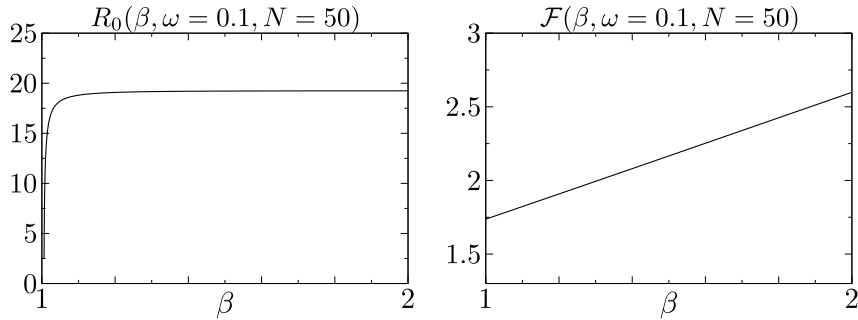


Figure 4.4 – Plots of $R_0(\beta, \omega, N)$ and $\mathcal{F}(\beta, \omega, N)$. The radius saturates until almost reaching the borders of the triangle. The frequency diverges. In this case $\beta_c = 1.0059$.

We notice that while the radius reaches a maximum value, the frequency diverges. This is telling us that limit cycles with small radius R_0 have a smaller angular velocity than the limit cycles with big radius.

This characterizes properly the only two possible scenarios when using the rates of the form (4.8): either a stable fixed point in the middle of the triangle or one stable limit cycle with a radius given in equation (4.20) and frequency given in equation (4.21).

4.2.2 Inhibitory term

In this section we want to study the dynamics of the system when the transition rates are of the form:

$$R_{i \rightarrow j}(n_i, n_j) = \frac{\tilde{\omega}}{n_i^\gamma}. \quad (4.22)$$

Here, we want also to know the dynamics of $n_A(t)$ and $n_B(t)$. Since we study the time evolution of the system at the mean field level, we have to introduce an auxiliary positive constant $\Delta > 0$ that helps us to have well defined rates (if $n_i = 0$, then equation (4.22) is indetermined). Thus, we change slightly and we use the following rates instead:

$$R_{i \rightarrow j}(n_i, n_j) = \lim_{\Delta \rightarrow 0} \left(\frac{\tilde{\omega}}{n_i^\gamma + \Delta} \right). \quad (4.23)$$

This small change does not affect the dynamics of the system because we take small values for Δ , i.e.: $\Delta \ll 1$. The mean field equations are then:

$$\begin{aligned} \dot{n}_A(t) &= \lim_{\Delta \rightarrow 0} \left(\frac{\tilde{\omega} (N - n_A(t) - n_B(t))}{(N - n_A(t) - n_B(t))^\gamma + \Delta} - \frac{\tilde{\omega} n_A(t)}{n_A^\gamma(t) + \Delta} \right) = g_1(n_A, n_B) \\ \dot{n}_B(t) &= \lim_{\Delta \rightarrow 0} \left(\frac{\tilde{\omega} n_A(t)}{n_A^\gamma(t) + \Delta} - \frac{\tilde{\omega} n_B(t)}{n_B^\gamma(t) + \Delta} \right) = g_2(n_A, n_B). \end{aligned} \quad (4.24)$$

Finding the fixed points and studying their stability in an analytical way is difficult for arbitrary values of γ , but a study of the nullclines of (4.24) gives a lot of information. We call nullcline 1 to the points that satisfy $g_1(\hat{n}_A, \hat{n}_B) = 0$. Analogously, for the nullcline 2 we look for the points satisfying $g_2(\hat{n}_A, \hat{n}_B) = 0$. In Figure 4.5, the two nullclines are plotted for several values of γ . The fixed points are located where the two nullclines cross,

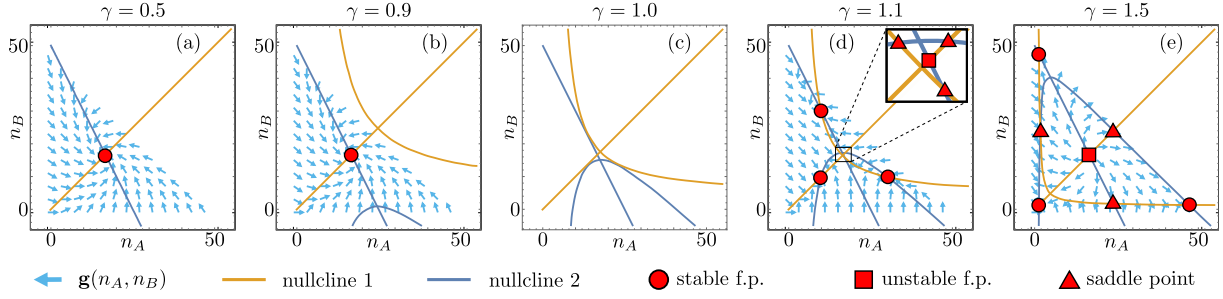


Figure 4.5 – Plot of the two nullclines, one in blue and one in yellow, for several values of γ . The fixed points are highlighted using a red geometrical figure, depending on the stability. Circles are stable ones, squares are unstable and triangles are saddle nodes. For values of $\gamma < 1$, there exists only one fixed point in the middle of the triangle, as shown in (a) and (b). For $\gamma = 1$ the two nullclines cross in three new points, depicted in (c). For values of $\gamma > 1$, the fixed point in the middle becomes unstable and six new fixed points appear. Three of them result to be stable, three result to be saddle nodes, as shown in (d) and (e). Notice that although the six new fixed points appear close to the center of the triangle, they move toward the corners and edges, as shown in (e). The used parameters are $N = 50$, $\tilde{\omega} = 1.1$ and $\Delta = 0.01$.

depicted with red symbols in Figure 4.5. Their stability can be studied by plotting the drift $\mathbf{g} = (g_1, g_2)$, given in (4.24). This drift is depicted with light-blue arrows in Figure 4.5. For values of $\gamma < 1$, there exists only one fixed point at $\hat{n}_A = \hat{n}_B = \hat{n} = N/3$, as shown in Figure 4.5a for $\gamma = 0.5$. For increasing values of γ , two hyperbolic branches appear and approach the fixed point in the middle of the triangle. The value $\gamma = 1$ results to be special because for this value the two hyperbolic branches of the nullclines collide or touch at three different points. For higher values ($\gamma > 1$), the three collisions give birth to six new fixed points. Out of these six points, three result to be stable and three result to be saddle nodes. Hence, here we have three saddle node bifurcations with the critical value of the parameter γ being $\gamma_c = 1$.

While on the one hand these six new points appear for values of $\gamma > \gamma_c$, on the other hand the fixed point in the middle of the triangle ($\hat{n}_A = \hat{n}_B = \hat{n} = N/3$) does not disappear, but it changes its stability. It becomes unstable. To confirm the change of stability of this particular point, we can analyse the original version of system (4.24):

$$\begin{aligned} \dot{n}_A &= \tilde{\omega} \left[(N - n_A - n_B)^{1-\gamma} - n_A^{1-\gamma} \right] \\ \dot{n}_B &= \tilde{\omega} \left[n_A^{1-\gamma} - n_B^{1-\gamma} \right] \end{aligned} \quad (4.25)$$

We can leave aside the constant Δ because in the neighborhood of this fixed point there are no problems with indeterminations. We make small perturbations around the point of interest of the form: $n_A(t) = \hat{n} + \epsilon_A(t)$ and $n_B(t) = \hat{n} + \epsilon_B(t)$. We get the system:

$$\begin{aligned} \dot{\epsilon}_A &= \tilde{\omega} \left[(\hat{n} - \epsilon_A - \epsilon_B)^{1-\gamma} - (\hat{n} + \epsilon_A)^{1-\gamma} \right] \\ \dot{\epsilon}_B &= \tilde{\omega} \left[(\hat{n} + \epsilon_A)^{1-\gamma} - (\hat{n} + \epsilon_B)^{1-\gamma} \right]. \end{aligned} \quad (4.26)$$

Using again the binomial series in (4.11) and staying at first order of perturbations, we get the linear system:

$$\begin{aligned}\dot{\epsilon}_A &= \frac{\tilde{\omega}(\gamma - 1)}{\hat{n}^\gamma} \left[2\epsilon_A + \epsilon_B \right] \\ \dot{\epsilon}_B &= \frac{\tilde{\omega}(\gamma - 1)}{\hat{n}^\gamma} \left[-\epsilon_A + \epsilon_B \right]\end{aligned}\tag{4.27}$$

The eigenvalues of (4.27) are:

$$\lambda_{1,2} = \frac{\tilde{\omega}(\gamma - 1)}{2\hat{n}^\gamma} \left(3 \pm i\sqrt{3} \right).\tag{4.28}$$

This tells us that the condition for the change of stability of the fixed point at the center of the triangle is:

$$\Re(\lambda_{1,2}) \stackrel{\leq}{\geq} 0 \quad \text{if} \quad \gamma \stackrel{\leq}{\geq} 1.\tag{4.29}$$

Thus, as expected, the critical value results to be $\gamma_c = 1$. To study the stability of the seven fixed points we can calculate its stability for a particular case that simplifies the calculations, namely $\gamma = 2$. The system we have to solve is:

$$\begin{aligned}\dot{n}_A(t) &= \lim_{\Delta \rightarrow 0} \left(\frac{\tilde{\omega} (N - n_A(t) - n_B(t))}{(N - n_A(t) - n_B(t))^2 + \Delta} - \frac{\tilde{\omega} n_A(t)}{n_A^2(t) + \Delta} \right) = g_1(n_A, n_B) \\ \dot{n}_B(t) &= \lim_{\Delta \rightarrow 0} \left(\frac{\tilde{\omega} n_A(t)}{n_A^2(t) + \Delta} - \frac{\tilde{\omega} n_B(t)}{n_B^2(t) + \Delta} \right) = g_2(n_A, n_B).\end{aligned}\tag{4.30}$$

To find the fixed points, we look for the points (\hat{n}_A, \hat{n}_B) that satisfy $g_1(\hat{n}_A, \hat{n}_B) = 0$ and $g_2(\hat{n}_A, \hat{n}_B) = 0$. From the second equation in (4.30) we get the first condition:

$$0 = \left(\hat{n}_A - \hat{n}_B \right) \left(\Delta - \hat{n}_A \hat{n}_B \right).\tag{4.31}$$

This condition is satisfied in two cases:

$$\text{case 1: } \hat{n}_A = \hat{n}_B \qquad \text{case 2: } \hat{n}_A = \frac{\Delta}{\hat{n}_B}.\tag{4.32}$$

When using these two conditions in the first equation in (4.30) we get two equations to solve:

$$-6\hat{n}_A^3 + 5N\hat{n}_A^2 - (N^2 - 3\Delta)\hat{n}_A + N\Delta = 0 \quad \text{case 1} \tag{4.33}$$

$$-2\hat{n}_A^4 + 3N\hat{n}_A^3 - (N^2 + 4\Delta)\hat{n}_A^2 + 3N\Delta\hat{n}_A - 2\Delta^2 = 0 \quad \text{case 2} \tag{4.34}$$

Equations (4.33) and (4.34) give us 7 fixed points for given values of the parameters. For $\gamma = 2$, $\tilde{\omega} = 1.1$, $\Delta = 0.01$ and $N = 50$ we get the set of fixed points:

$(\hat{n}_A, \hat{n}_B) = (16.7, 16.7)$	unstable fixed point
$(\hat{n}_A, \hat{n}_B) = (0.35, 49.6)$	stable fixed point
$(\hat{n}_A, \hat{n}_B) = (49.6, 0.35)$	stable fixed point
$(\hat{n}_A, \hat{n}_B) = (0.35, 0.35)$	stable fixed point
$(\hat{n}_A, \hat{n}_B) = (24.9, 24.9)$	saddle point
$(\hat{n}_A, \hat{n}_B) = (0.35, 24.9)$	saddle point
$(\hat{n}_A, \hat{n}_B) = (24.9, 0.35)$	saddle point

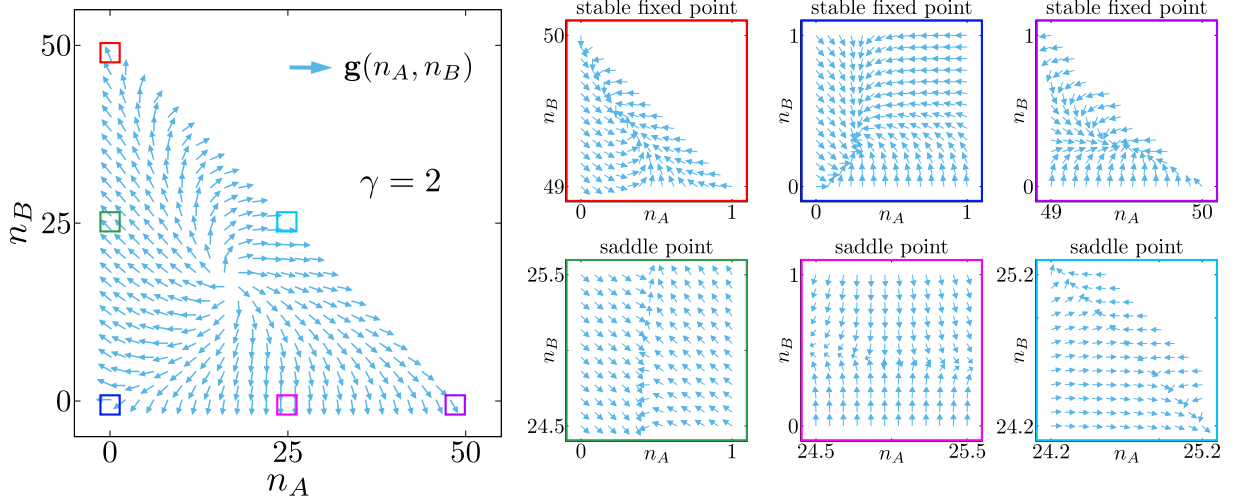


Figure 4.6 – Detailed study of the seven fixed points for the case $\gamma > \gamma_c$. The three points in the corners of the triangle result to be stable fixed points. The three points located in the middle of the edges of the triangle result to be saddle points. The fixed point located in $\hat{n}_A = \hat{n}_B = N/3$ results to be an unstable fixed point. For this plot, the used parameters are $N = 50$, $\tilde{\omega} = 1.1$, $\Delta = 0.01$ and $\gamma = 2$.

The plot of these fixed points can be found in Figure 4.6.

4.2.3 Parameter diagram using both terms

Now, we study the system using both, the recruiting and the inhibitory terms at the same time. The rates are in this case:

$$R_{i \rightarrow j}(n_i, n_j) = \lim_{\Delta \rightarrow 0} \left(\frac{n_j^\beta + \omega}{n_i^\gamma + \Delta} \right). \quad (4.35)$$

The mean field equations result to be:

$$\begin{aligned} \dot{n}_A(t) &= \left(\frac{n_A^\beta(t) + \omega}{(N - n_A(t) - n_B(t))^\gamma + \Delta} \right) (N - n_A(t) - n_B(t)) - \left(\frac{n_B^\beta(t) + \omega}{n_A^\gamma(t) + \Delta} \right) n_A(t) \\ \dot{n}_B(t) &= \left(\frac{n_B^\beta(t) + \omega}{n_A^\gamma(t) + \Delta} \right) n_A(t) - \left(\frac{(N - n_A(t) - n_B(t))^\beta + \omega}{n_B^\gamma(t) + \Delta} \right) n_B(t). \end{aligned} \quad (4.36)$$

We can use (4.36) to get the two equations we have to solve to find the fixed points (\hat{n}_A, \hat{n}_B) :

$$\begin{aligned} \left(\hat{n}_A^\beta + \omega \right) \left(N - \hat{n}_A - \hat{n}_B \right) \left(\hat{n}_A^\gamma + \Delta \right) - \left(\hat{n}_B^\beta + \omega \right) \hat{n}_A \left[\left(N - \hat{n}_A - \hat{n}_B \right)^\gamma + \Delta \right] &= 0 \\ \hat{n}_A \left(\hat{n}_B^\beta + \omega \right) \left(\hat{n}_B^\gamma + \Delta \right) - \hat{n}_B \left(\hat{n}_A^\gamma + \Delta \right) \left[\left(N - \hat{n}_A - \hat{n}_B \right)^\beta + \omega \right] &= 0. \end{aligned} \quad (4.37)$$

To find the solution of (4.37) is in general very difficult for arbitrary values of β and γ . Although we can not calculate explicitly the fixed points, we can establish the linear system we would have to solve to study their stability in order to appreciate the complexity of this case. As always, we use small perturbations around the fixed points: $n_A(t) = \hat{n}_A + \epsilon_A(t)$ and $n_B(t) = \hat{n}_B + \epsilon_B(t)$. The linear system we get is:

$$\begin{aligned} \dot{\epsilon}_A(t) &= \left[\frac{(N - \hat{n}_B)\beta\hat{n}_A^{\beta-1} - (\beta + 1)\hat{n}_A^\beta - \omega}{(N - \hat{n}_A - \hat{n}_B)^\gamma + \Delta} - \frac{\hat{n}_B^\beta + \omega}{\hat{n}_A^\gamma + \Delta} \right] \epsilon_A(t) \\ &\quad - \left[\frac{\beta\hat{n}_B^{\beta-1}\hat{n}_A}{\hat{n}_A^\gamma + \Delta} + \frac{\hat{n}_A^\beta + \omega}{(N - \hat{n}_A - \hat{n}_B)^\gamma + \Delta} \right] \epsilon_B(t), \\ \dot{\epsilon}_B(t) &= \left[\frac{\beta(N - \hat{n}_A - \hat{n}_B)^{\beta-1}\hat{n}_B}{\hat{n}_B^\gamma + \Delta} + \frac{\hat{n}_B^\beta + \omega}{\hat{n}_A^\gamma + \Delta} \right] \epsilon_A(t) \\ &\quad + \left[\frac{\beta\hat{n}_B(N - \hat{n}_A - \hat{n}_B)^{\beta-1} - \left[(N - \hat{n}_A - \hat{n}_B)^\beta + \omega \right]}{\hat{n}_B^\gamma + \Delta} + \frac{\beta\hat{n}_B^{\beta-1}\hat{n}_A}{\hat{n}_A^\gamma + \Delta} \right] \epsilon_B(t). \end{aligned} \quad (4.38)$$

Evidently it is impossible to solve (4.37) and (4.38) analitically, but we can perform numerical simulations to study the dependence of the dynamics of the system on the parameters β and γ . We integrate the mean field equations in (4.36) using a classical 4th order Runge-Kutta method. The results of the numerical simulations are shown in Figure 4.7. In this figure, we can see that there are only three possible scenarios, which are the ones we already found by studying the recruiting and inhibitory terms separately. We call them region I, region II and region III. The first possibility is to have one unstable fixed point and one stable limit circle (region I), the second one is to have only one stable fixed point (region II) and the third option is to have seven fixed points, one unstable, three stable and three saddle points (region III).

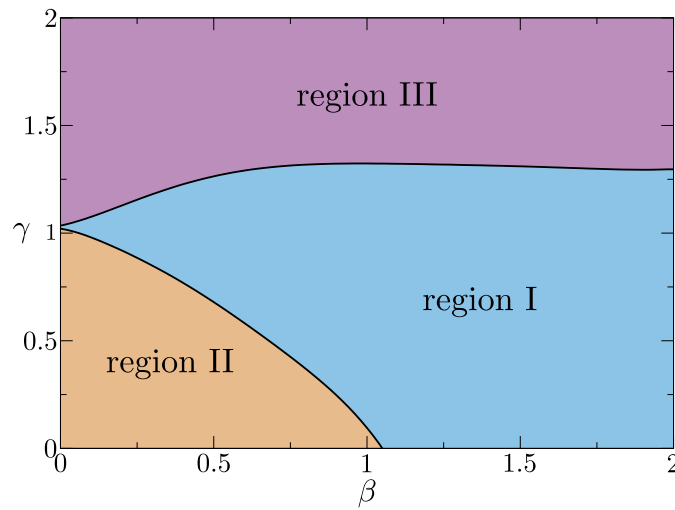


Figure 4.7 – Parameter diagram in the β vs. γ space that shows the existence of the three behaviors studied separately in the Recruiting term and the Inhibitory term. The used parameters: $\omega = 0.1$, $N = 50$ and $\Delta = 0.01$.

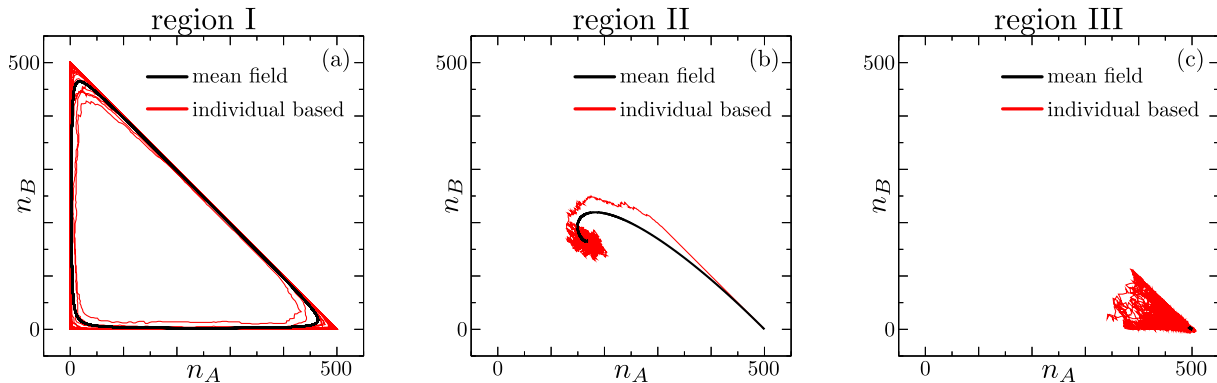


Figure 4.8 – Three plots of the mean field solution obtained by the integration of the system of equations in (4.36) (plotted in black), as well as the IBM simulations (plotted in red). We used the sets of parameters of (4.39): set 1 for (a), set 2 for (b) and set 3 for (c). The initial condition for all the cases is: $n_A(t=0) = N$, $n_B(t=0) = 0$. The system size is $N = 500$, $\omega = 0.1$ and we used the auxiliary constant value $\Delta = 0.01$ for the integration of the mean field equations.

If we use different values for ω or N , the resulting diagrams are qualitatively equal to the one presented in Figure 4.7. Two phase diagrams can be found in Appendix C for different values of ω . The parameter diagram in Figure 4.7 results to be an accurate guide that tells us what happens in the complete stochastic system. We performed IBM simulations to get the temporal evolution of a system of $N = 500$ of these particles using the transition rates in (4.2). We selected three sets of parameters, one for each region in Figure 4.7. These sets are:

set 1	$\beta = 1.1$	$\gamma = 0.0$	(region I)	
set 2	$\beta = 0.2$	$\gamma = 0.2$	(region II)	(4.39)
set 3	$\beta = 0.0$	$\gamma = 1.1$	(region III)	

We notice that although fluctuations are present in the IBM simulations, the behavior is qualitatively equal. This is not particular for the sets of parameters we selected, but it is general for the whole parameter space $\beta \in [0, 2]$ and $\gamma \in [0, 2]$. We will use all these results obtained in the mean field study as a valuable guide to understand the time dynamics in the complete stochastic system.

4.3 Stochastic system

The complete stochastic system is defined by the master equation given at the beginning of this chapter, in equation (4.3). The dynamics of each of the N particles of the system is encoded in its internal variable $q_i(t)$ that makes transitions between three states. The dynamics at the collective level is given by the variables $n_A(t)$, $n_B(t)$ and $n_C(t)$. This is depicted with a small scheme in Figure 4.9. We performed **I**ndividual **B**ased **M**odel (IBM) simulations to observe the effect of the parameters β , γ and ω on the behavior of the individual particles. To follow the dynamics of the internal variables of the particles we can plot a dicotomic signal we call $\psi_i^A(t)$ that is defined as follows:

$$\psi_i^A(t) = \delta_{q_i(t), A}, \quad (4.40)$$

where $\delta_{i,j}$ denotes the Kronecker delta function. This signal is different of zero only when the internal variable $q_i(t) = A$.

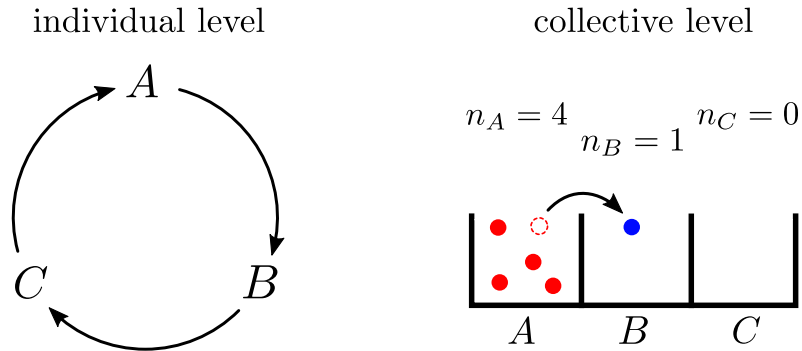


Figure 4.9 – Scheme to visualize the two levels of temporal dynamics: an individual level with transitions between states A , B , C , and a collective level via the number of particles in each state $n_A(t)$, $n_B(t)$, $n_C(t)$. In this example, the group size is $N = 5$.

We can define analogous signals for states B and C for each particle i , namely $\psi_i^B(t)$ and $\psi_i^C(t)$. These three signals satisfy the conditions:

$$\psi_i^A(t) + \psi_i^B(t) + \psi_i^C(t) = 1 \quad \forall i \in [1, \dots, N] \quad \text{and} \quad \forall t \geq 0 \quad (4.41)$$

$$\sum_{i=1}^N \psi_i^A(t) + \sum_{i=1}^N \psi_i^B(t) + \sum_{i=1}^N \psi_i^C(t) = N \quad \forall t \geq 0 \quad (4.42)$$

$$\sum_{i=1}^N \psi_i^A(t) = n_A(t), \quad \sum_{i=1}^N \psi_i^B(t) = n_B(t), \quad \sum_{i=1}^N \psi_i^C(t) = n_C(t). \quad (4.43)$$

Notice that contrary to Section 4.2 of this chapter (where the mean field dynamics was studied in detail), here the variables $n_A(t)$, $n_B(t)$ and $n_C(t)$ are stochastic variables. We show the plot of $\psi_i^A(t)$ for all individuals of a group of size $N = 4$, as well as the collective variable $n_A(t)$ in Figure 4.10 for two sets of parameters. In the case of Figure 4.10a, we can see that the system has a high synchronization between individual and collective levels. The used parameters are $\beta = 1.1$, $\gamma = 0$ and $\omega = 0.1$. On the other hand, in the case of Figure 4.10b, there is no synchronization between the individuals that leads to a very noisy collective signal. The used parameters are $\beta = 0$, $\gamma = 2$ and $\omega = 0.1$. It is important to notice that in any of the two cases, the collective signals $n_A(t)$, $n_B(t)$ and $n_C(t)$ are stochastic and periodic.

Although the system is stochastic and in general we can not give an exact expression for quantities like the average period $\langle T \rangle$ or the distribution probability of periods $P(T)$ as function of the system parameters, we can introduce a concept we call **Collective Clock Approximation (CCA)** to give analytical expressions that are going to be approximations to these observables. We introduce also a simplified version of the CCA that we refer to as **Metaparticle Clock Approximation (MCA)** that reduces substantially the complexity of the calculations. These two ideas are explained and studied in the following subsections.

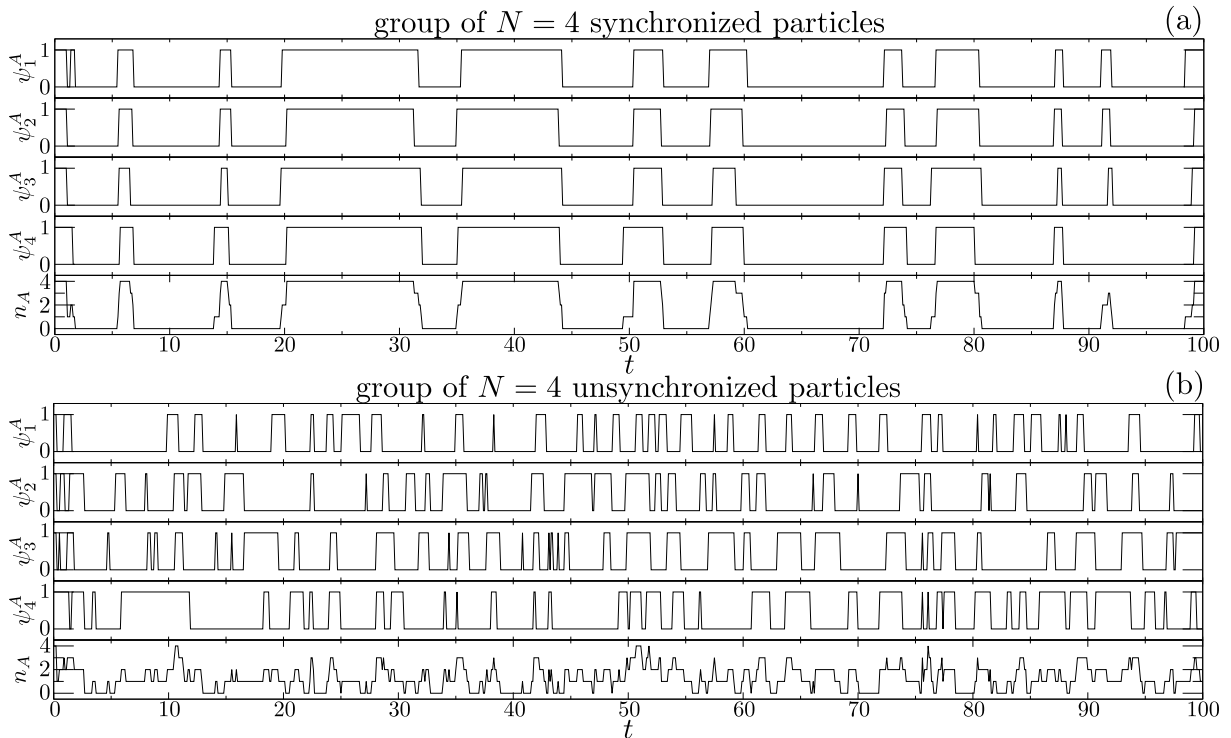


Figure 4.10 – The individual and the collective dynamics of a group of size $N = 4$ is shown. The individual dicotomic signals are given by $\psi_i^A(t)$ and the collective variable is $n_A(t) = \sum_{i=1}^N \psi_i^A(t)$. The system parameters are $\beta = 1.1$, $\gamma = 0$ and $\omega = 0.1$ for (a) and $\beta = 0$, $\gamma = 2$ and $\omega = 0.1$ for (b).

4.3.1 The Collective Clock Approximation

To use the concept of the **Collective Clock** we have to make only one main hypothesis: **the transitions of the particles between the three states are going to happen in an ordered way**. To clarify what we mean by order we use an example. Let us assume that the system is in the configuration $n_A = N$, $n_B = 0$ and $n_C = 0$. Then, in the CCA, the particles will begin to transit to state B one after the other until reaching the configuration $n_A = 0$, $n_B = N$ and $n_C = 0$. We are going to refer to this sequence of transitions as a collective cascade from state A to state B . Once the state B is populated, then a second collective cascade is going to make particles populate the state C in an analogous way until reaching the configuration $n_A = 0$, $n_B = 0$ and $n_C = N$. A third collective cascade is going to make particles move or transit collectively from state C back to state A in order to reach the initial configuration $n_A = N$, $n_B = 0$ and $n_C = 0$. The time it takes to make all the sequence of these three collective cascades described above is what we define as the period T^{cc} in the CCA. All these cascades are depicted in Figure 4.11 for the **Collective Clock** associated to a system of size $N = 2$. In this figure, we use particular labels for each one of the configurations in the **Collective Clock**. Without loss of generality, the configuration $n_A = 2$, $n_B = 0$ and $n_C = 0$ is labeled as 1^{cc} . The ordered configurations are going to be labeled increasingly. For the rest of this chapter, we will assume that in a **Collective Clock** of arbitrary size N , the first state 1^{cc} is going to be the configuration given by $n_A(t) = N$, $n_B(t) = 0$ and $n_C(t) = 0$. We can write the rates of the corresponding collective clock using the definition of the individual rates given in

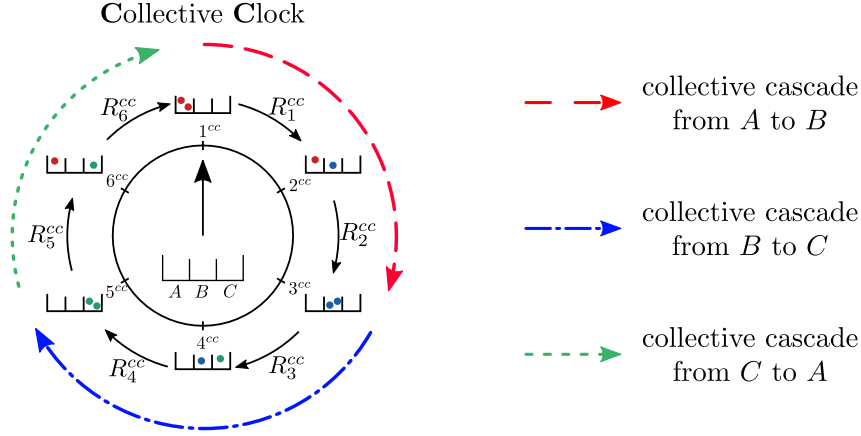


Figure 4.11 – A scheme of the **Collective Clock** for a system of size $N = 2$ is shown, as well as the three collective cascades (colored arrows) between the states A , B and C .

(4.2) as follows:

$$R_i^{cc} = \begin{cases} R_{A \rightarrow B}(N - (i - 1), i - 1) \times \begin{bmatrix} N - (i - 1) \end{bmatrix} & \text{for } 1 \leq i \leq N \\ R_{B \rightarrow C}(2N - (i - 1), i - 1) \times \begin{bmatrix} 2N - (i - 1) \end{bmatrix} & \text{for } (N + 1) \leq i \leq 2N \\ R_{C \rightarrow A}(3N - (i - 1), i - 1) \times \begin{bmatrix} 3N - (i - 1) \end{bmatrix} & \text{for } (2N + 1) \leq i \leq 3N \end{cases} \quad (4.44)$$

Notice that the **Collective Clock** has $3N$ configurations or ticks. If we want to calculate the period, we just need to calculate the first passage time to return to the initial state 1^{cc} . To do this, we need to solve the following system:

$$\begin{aligned} \partial_t P_1^{cc}(t) &= -R_1^{cc} P_1^{cc}(t), \\ \partial_t P_i^{cc}(t) &= -R_i^{cc} P_i^{cc}(t) + R_{i-1}^{cc} P_{i-1}^{cc}(t) \end{aligned} \quad \text{for } 2 \leq i \leq 3N. \quad (4.45)$$

In the system of equations (4.45) we denote by $P_i^{cc}(t)$ the probability of being in the tick i^{cc} at time t having started at tick 1^{cc} at time $t = 0$. The first passage time is calculated using the auxiliary function

$$\phi^{cc}(t) = \sum_{i=1}^{3N} P_i^{cc}(t). \quad (4.46)$$

We can write the distribution probability $P(T^{cc} = t)$ of the period T^{cc} as

$$P(T^{cc} = t) = |\partial_t \phi(t)| = R_{3N}^{cc} \cdot P_{3N}^{cc}(t). \quad (4.47)$$

One of the advantages of introducing the concept of the CCA is precisely the possibility to give an analytic expression for the solution of the system (4.45), which in the general case of a collective clock of N particles is:

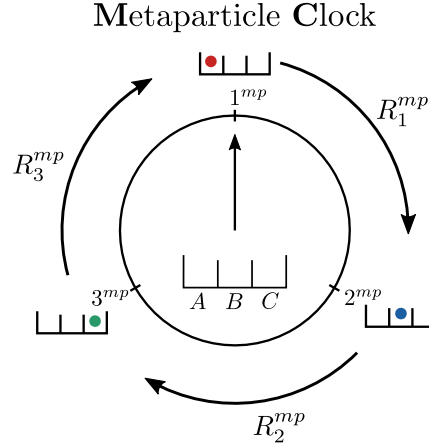


Figure 4.12 – A scheme of a **Metaparticle Clock** is shown. This scheme is valid for all group sizes.

$$P(T^{cc} = t) = \left(\prod_{i=1}^{3N} R_i^{cc} \right) \int_0^t dt_1 \int_0^{t-t_1} dt_2 \dots \int_0^{t-\tau_{3N-2}} dt_{3N-1} \exp \left[- \sum_{j=1}^{3N-1} R_j^{cc} t_j - R_{3N}^{cc} (t - \tau_{3N-1}) \right]. \quad (4.48)$$

where we make use of the auxiliary variable

$$\tau_j = \sum_{k=1}^j t_k. \quad (4.49)$$

For details on the calculation to obtain the general result given in (4.48), see Appendix C. Once having the analytical expression for $P(T^{cc})$ we can calculate the average period $\langle T^{cc} \rangle$ as follows:

$$\langle T^{cc} \rangle = \int_0^{\infty} t P(T^{cc} = t) dt. \quad (4.50)$$

4.3.2 The Metaparticle Clock Approximation

In this section we introduce the idea of **Metaparticle Clock**. For this approximation we are going to assume again that the transitions of the particles between states are going to happen in an ordered way. The second assumption is that the collective cascades are so fast that we can describe the whole system of N particles as if it was a system of only one particle (or **Metaparticle**) that makes transitions between the three states. Notice that there are only three ticks and three transition rates R_i^{mp} , with $i \in \{1, 2, 3\}$, for all group sizes, as shown in Figure 4.12. Since each transition represents a whole collective cascade, we are going to say that, in average, the time the **Metaparticle Clock** takes to make one transition is the same as the time for the corresponding cascade. Hence, we can determine the transition rates in the MPA using the transition rates from the **Collective Clock** by calculating:

$$\frac{1}{R_i^{mp}} = \sum_{j=1}^N \frac{1}{R_{(i-1)N+j}^{cc}} \quad \text{for } i = 1, 2, 3. \quad (4.51)$$

This gives as a result that $R_1^{mp} = R_2^{mp} = R_3^{mp} := R^{mp}$ for all system sizes and for all parameters β , γ and ω . In this MCA we can establish a simpler but analogous system to the one in equation (4.45):

$$\begin{aligned}\partial_t P_1^{mp}(t) &= -R^{mp} P_1^{mp}(t), \\ \partial_t P_2^{mp}(t) &= -R^{mp} P_2^{mp}(t) + R^{mp} P_1^{mp}(t), \\ \partial_t P_3^{mp}(t) &= -R^{mp} P_3^{mp}(t) + R^{mp} P_2^{mp}(t).\end{aligned}\tag{4.52}$$

Using also the auxiliary function

$$\phi^{mp}(t) = \sum_{i=1}^3 P_i^{mp}(t) = P_1^{mp}(t) + P_2^{mp}(t) + P_3^{mp}(t),\tag{4.53}$$

we can write the distribution probability $P(T^{mp} = t)$ of the period T^{mp} in the MCA as

$$P(T^{mp} = t) = |\partial_t \phi^{mp}(t)| = R^{mp} \cdot P_3^{mp}(t).\tag{4.54}$$

The system in (4.52) has been studied before in [66]. The solution of (4.52) is given by the following γ -distribution:

$$P(T^{mp} = t) = \frac{1}{2} (R^{mp})^3 t^2 e^{-R^{mp} t}\tag{4.55}$$

Once having the analytical expression for $P(T^{mp})$ we can calculate the average period $\langle T^{mp} \rangle$ as follows:

$$\langle T^{mp} \rangle = \int_0^{\infty} t P(T^{mp} = t) dt.\tag{4.56}$$

We can use the general formula:

$$\int_0^{\infty} t^a \exp^{-bt} dt = \frac{a!}{b^{a+1}},\tag{4.57}$$

with a and b two arbitrary constants. Using (4.57) we can give a final expression for the average period in the MCA, which results to be:

$$\langle T^{mp} \rangle = \frac{3}{R^{mp}}\tag{4.58}$$

Notice that expression (4.48) for $P(T^{cc} = t)$ is substancially more complicated than expression (4.55) for $P(T^{mp} = t)$. Although the analytic expressions of $P(T)$ are different in both approximations, we know that the average value of the period $\langle T \rangle$ is exactly the same for CCA and MCA.

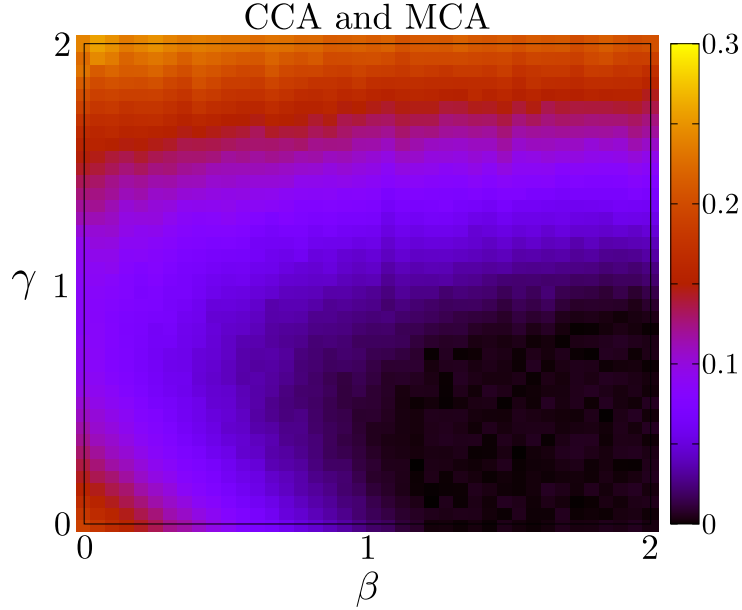


Figure 4.13 – This plot corresponds to parameter \mathcal{E}_1 for both approximations, CCA and MCA. The system parameters are $N = 50$ and $\omega = 0.1$.

4.4 Numerical comparison of CCA and MCA with IBM simulations

Once having explained how to obtain the analytical expressions for the distribution probability of the period $P(T)$ for the CCA and MCA, we can compare the accuracy of these two approximations for different parameter values. We can use a parameter we call \mathcal{E}_1 , defined as:

$$\mathcal{E}_1(\beta, \gamma) = 1 - \frac{\min \left\{ \langle T(\beta, \gamma) \rangle, \langle T(\beta, \gamma) \rangle^{ibm} \right\}}{\max \left\{ \langle T(\beta, \gamma) \rangle, \langle T(\beta, \gamma) \rangle^{ibm} \right\}}, \quad (4.59)$$

with $\langle T(\beta, \gamma) \rangle$ the value of the average period for the CCA and the MCA approximations, which is the same. We denote by $\langle T(\beta, \gamma) \rangle^{ibm}$ the value obtained from the IBM simulations. We are interested to study the same region in the parameter space that we studied in the mean field section, namely $\beta \in [0, 2]$ and $\gamma \in [0, 2]$. Due to the definition of $\mathcal{E}_1(\beta, \gamma)$ in equation (4.59), the value of this parameter is always positive. A value of $\mathcal{E}_1(\beta, \gamma) \approx 0$ for given values of β and γ is telling us that the two approximations (CCA and MCA) give accurate values that match the IBM numerical results. On the other hand, if $\mathcal{E}_1 \rightarrow 1$, the approximations are not good. Results are shown in Figure 4.13. The region of accuracy of the approximations is roughly $\beta > 1$ and $\gamma < 1$. When making the comparison with the mean field parameter diagram in Figure 4.7 we notice that the CCA and MCA give accurate results in what we called region I, associated with the existence of a limit cycle in the mean field study.

4.5 Summary & perspectives

The plot in Figure 4.13 associates the results obtained with the mean field study, the concepts of the **Collective Clock** and **Metaparticle Clock** and the IBM simulations of the complete stochastic system. We learned the following: to talk about a synchronized system (like the one shown in Figure 4.10a) is the same as to talk about a limit cycle at the mean field level. We also learned that this particular situation is well described analytically using the concepts of **Collective Clock** and **Metaparticle Clock**. The seemingly simple concepts of the CCA and the MCA introduced in this chapter will prove to serve enormously to describe the transport properties of a group of N active particles that explore the space having an **Internal Control System** (ICS) of three states. The concepts of the CCA and the MCA are general enough to be used to describe synchronized systems of particles in general scenarios and will give accurate results for the temporal dynamics of a system of N synchronized particles that make transitions between any arbitrary number M of states.

Chapter 5

Collective transport of particles with three internal states

Contents

5.1	Average transport properties	75
5.1.1	Average mean squared displacement $\langle \mathbf{x}_{cm}^2(t) \rangle$	75
5.1.2	Average dispersion around the center of mass $\langle \sigma_g^2 \rangle$	78
5.2	Discussion and results	81
5.3	Summary & perspectives	84

We want to study the spatial dynamics of a system consisting of N active particles whose internal dynamics is given by the three state model discussed in the previous chapter. The particles have an internal variable $q_i(t)$ that evolves in time as explained in the three state model, making transitions between the states A , B and C . Inspired in the experimental observations done with the small groups of gregarious animals (Chapter 2, Section 2.2), in this model the particles follow a different equation of motion depending on the value of the internal variable $q_i(t)$. The particles are going to be diffusive when the internal variable is in state A (“grazing” state S_1 in Chapter 2), they move with constant speed v_0 when $q_i(t) = B$ (“moving” state M in Chapter 2) and they feel a drift toward the center of mass of the group only when $q_i(t) = C$ (“head up” state S_2 in Chapter 2). Mathematically speaking, we express this as follows:

$$\left. \begin{aligned} \dot{\mathbf{x}}_i(t) &= \sqrt{2D_0} \boldsymbol{\xi}(t) \\ \dot{\boldsymbol{\theta}}_i(t) &= 0 \end{aligned} \right\} \text{if } q_i(t) = A, \quad (5.1)$$

$$\left. \begin{aligned} \dot{\mathbf{x}}_i(t) &= v_0 \hat{\mathbf{e}}_i(\boldsymbol{\theta}_i) + \sqrt{2D_0} \boldsymbol{\xi}(t) \\ \dot{\boldsymbol{\theta}}_i(t) &= \left\{ \begin{array}{l} \text{New direction (incidental leader)} \\ \sum_{j=1}^N \sin(\boldsymbol{\theta}_j - \boldsymbol{\theta}_i) \delta_{q_j, B} \end{array} \right\} \end{aligned} \right\} \text{if } q_i(t) = B, \quad (5.2)$$

$$\left. \begin{aligned} \dot{\mathbf{x}}_i(t) &= \Gamma_0 \sum_{|\mathbf{x}_j - \mathbf{x}_i| \leq r_0} (\mathbf{x}_j(t) - \mathbf{x}_i(t)) + \sqrt{2D_0} \boldsymbol{\xi}(t) \\ \dot{\boldsymbol{\theta}}_i(t) &= 0 \end{aligned} \right\} \text{if } q_i(t) = C. \quad (5.3)$$

The Langevin equations (5.1), (5.2) and (5.3) are valid for n dimensions. The position of the particles is given by the vector $\mathbf{x}_i(t)$ and the variable $\boldsymbol{\theta}_i$ contains the information of the orientation of the particle. Thus, $\hat{\mathbf{e}}(\boldsymbol{\theta})$ is a unitary n dimensional vector and is, for example, defined as $\hat{\mathbf{e}}(\theta) = (\cos \theta, \sin \theta)$ in $n = 2$ dimensions. The variable $\boldsymbol{\xi}(t)$ is a stochastic n dimensional variable representing white noise. The constants Γ_0 and D_0 are parameters of the model. The dynamics of the direction of motion is going to be dictated by the first particle that reaches the moving state B that was previously empty, as shown in Figure 5.1 for the one dimensional case.

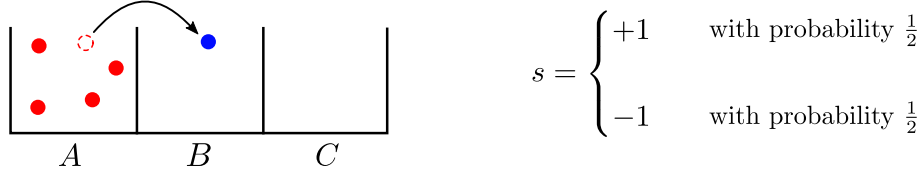


Figure 5.1 – Scheme to visualize the dynamics of the change of direction of motion $\hat{\mathbf{e}}_i(\boldsymbol{\theta}_i)$. In the one dimensional case, the first particle to reach a previously empty state B (the blue particle in the figure) will reverse its direction of motion with probability $1/2$ and continue in the same direction with probability $1/2$. In 2D, the new angle is going to be chosen randomly with equal probability $1/2\pi$.

In the n dimensional case, this particle will select a new direction of motion $\hat{\mathbf{e}}_i(\boldsymbol{\theta}_i)$ by taking a random angle in the unitary n dimensional sphere \mathcal{S}^n with probability $1/\mathcal{S}^n$. The particles that reach the moving state B after the incidental leader will move in the same direction, as expressed in equation (5.2).

We are interested in three collective physical quantities that give us information of the transport properties of the group. The first one is the center of mass, defined as:

$$\mathbf{x}_{cm}(t) = \frac{1}{N} \sum_{i=1}^N \mathbf{x}_i(t). \quad (5.4)$$

The second one is the mean squared displacement (MSD) of the center of mass defined as: $\langle (\mathbf{x}_{cm}(t) - \mathbf{x}_{cm}(0))^2 \rangle$. The third quantity is the dispersion of particles around the center of mass, defined as

$$\sigma_g^2(t) = \frac{1}{N} \sum_{i=1}^N \left(\mathbf{x}_i(t) - \mathbf{x}_{cm}(t) \right)^2. \quad (5.5)$$

These three collective observables characterize well enough the spatial motion of the group. The center of mass represents the displacement of the group, its MSD quantifies how much does the group explores the space, and $\sigma_g^2(t)$ quantifies the degree of cohesion of the group. As an example, in Figure 5.2 we present two kymographs obtained using Individual Based Model (IBM) simulations for a group of $N = 10$ particles using two sets of parameters (β and γ). Using the CCA and MCA approximations, we derive analytical expressions for the average values of these collective transport properties and compare the results with IBM simulations.

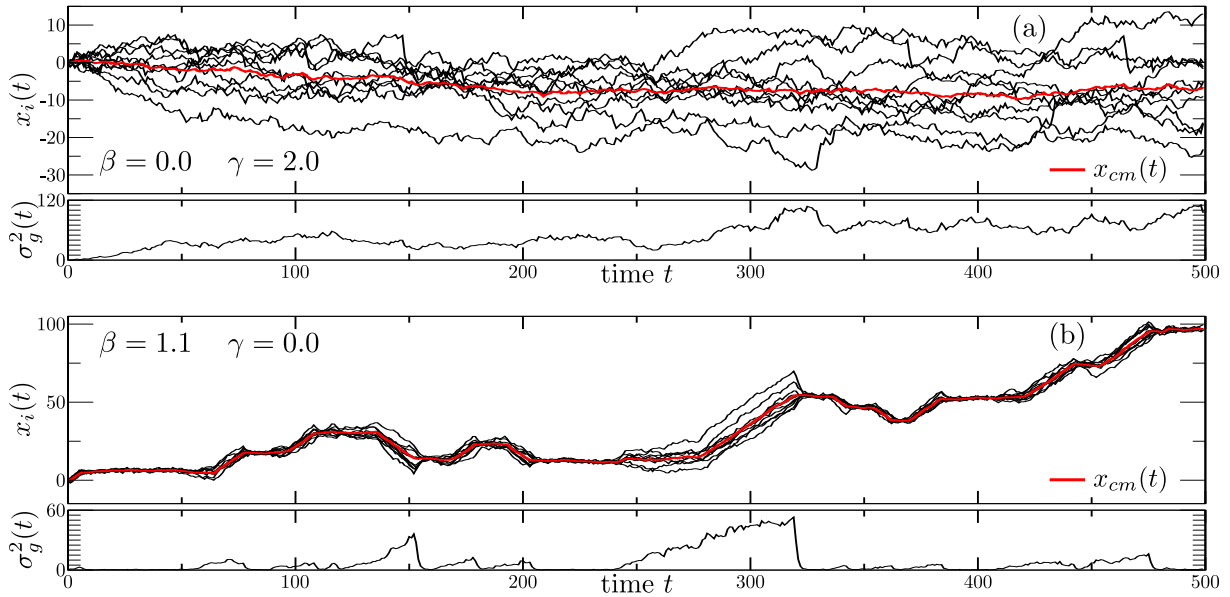


Figure 5.2 – Kymograph of two different scenarios for a system of $N = 10$ in 1 dimension. (a) Unsynchronized case using $\beta = 0.0$ and $\gamma = 2.0$. (b) Highly synchronized case using $\beta = 1.1$ and $\gamma = 0.0$. The parameters are $v_0 = 1$, $D_0 = 0.5$, $\Gamma_0 = 0.5$ and $\omega = 0.01$.

5.1 Average transport properties

In this section we explain in detail how to use the concepts of CCA and MCA to obtain analytical expressions for the average mean squared displacement (MSD) of the center of mass $\langle (\mathbf{x}_{cm}(t) - \mathbf{x}_{cm}(0))^2 \rangle$, as well as the average dispersion of particles around the center of mass $\langle \sigma_g^2 \rangle$.

5.1.1 Average mean squared displacement $\langle \mathbf{x}_{cm}^2(t) \rangle$

The Collective Clock Approximation

Our subject of study is a group of N active particles that move in space using the Langevin equations given in (5.1), (5.2) and (5.3). We want to quantify how the group explore the space and for that we use the center of mass. The equation of motion of the center of mass is:

$$\dot{\mathbf{x}}_{cm}(t) = \mathbf{v}_{cm}(t) = v_{cm}(t) \hat{\mathbf{e}}_{cm}(\boldsymbol{\theta}_{cm}), \quad (5.6)$$

with $v_{cm}(t)$ the magnitude of the velocity vector and the direction of motion of the center of mass given by the unitary vector $\hat{\mathbf{e}}_{cm}(\boldsymbol{\theta}_{cm})$ in n dimensions. Although in general the equation (5.6) is correct, it is useless since the functions $v_{cm}(t)$ and $\hat{\mathbf{e}}_{cm}(\boldsymbol{\theta}_{cm})$ are complicated. Nonetheless, we can always obtain the general expression of the average value of the mean squared displacement of the center of mass, as derived in [67]. This expression is:

$$\langle \mathbf{x}_{cm}^2(t) \rangle = \int_{\Omega} d\boldsymbol{\theta}'_{cm} \int_{\Omega} d\boldsymbol{\theta}''_{cm} \langle \mathcal{D}(\boldsymbol{\theta}''_{cm}, t) \mathcal{D}(\boldsymbol{\theta}'_{cm}, t) \rangle, \quad (5.7)$$

with $\langle \mathcal{D}(\boldsymbol{\theta}_{cm}, t) \rangle$ the average distance covered by the center of mass moving along direction $\boldsymbol{\theta}_{cm}$ since the beginning of the trajectory at $t = 0$. This average is given by

$$\langle \mathcal{D}(\boldsymbol{\theta}_{cm}, t) \rangle = \int_0^t dt' \int_0^\infty dv_{cm} v_{cm} P(\boldsymbol{\theta}_{cm}, v_{cm}, t), \quad (5.8)$$

with $P(\boldsymbol{\theta}_{cm}, v_{cm}, t)$ the probability density to find the center of mass moving in direction $\boldsymbol{\theta}_{cm}$ with speed v_{cm} at time t . Using (5.7) and (5.8) we arrive to the expression valid in any dimension n :

$$\langle \mathbf{x}_{cm}^2(t) \rangle = \int_{\Omega} d\boldsymbol{\theta}_{cm}'' \int_{\Omega} d\boldsymbol{\theta}_{cm}' \int_0^t dt'' \int_0^t dt' \int_0^\infty dv_{cm}'' \int_0^\infty dv_{cm}' \mathcal{W}(v_{cm}', v_{cm}'', d\boldsymbol{\theta}_{cm}', d\boldsymbol{\theta}_{cm}'', t', t''), \quad (5.9)$$

with

$$\mathcal{W}(v_{cm}', v_{cm}'', d\boldsymbol{\theta}_{cm}', d\boldsymbol{\theta}_{cm}'', t', t'') = v_{cm}' v_{cm}'' P(\boldsymbol{\theta}_{cm}', v_{cm}', t'; \boldsymbol{\theta}_{cm}'', v_{cm}'', t'') \hat{\mathbf{e}}(\boldsymbol{\theta}_{cm}') \cdot \hat{\mathbf{e}}(\boldsymbol{\theta}_{cm}''), \quad (5.10)$$

where $P(\boldsymbol{\theta}_{cm}', v_{cm}', t'; \boldsymbol{\theta}_{cm}'', v_{cm}'', t'')$ is the joint probability distribution of finding the center of mass with velocity v_{cm}' and direction $\boldsymbol{\theta}_{cm}'$ at time t' and velocity v_{cm}'' and direction $\boldsymbol{\theta}_{cm}''$ at time t'' . The integral over $d\boldsymbol{\theta}_{cm}$ is done over the whole surface of an unitary sphere of dimension $(n - 1)$, referred as Ω . Equation (5.9) can be recasted using the **Collective Clock Approximation (CCA)** if we realise that the velocity of the center of mass in the i^{cc} -th tick in the collective clock is given by:

$$v_i^{cc} = \begin{cases} \frac{i-1}{N} & \text{if } 1 \leq i \leq (N+1), \\ \frac{N - [i - (N+1)]}{N} & \text{if } (N+2) \leq i \leq 2N, \\ 0 & \text{if } (2N+1) \leq i \leq 3N, \end{cases} \quad (5.11)$$

where we supposed – as explained in the previous chapter – that 1^{cc} corresponds to the configuration $\mathbf{n} = (N, 0, 0)$. Using the notation of (5.11) we can express the average mean squared displacement of the center of mass in the CCA as follows:

$$\langle \mathbf{x}_{cm}^2(t) \rangle = \int_{\Omega} d\boldsymbol{\theta}_i^{cc} \int_{\Omega} d\boldsymbol{\theta}_j^{cc} \int_0^t dt'' \int_0^t dt' \sum_{i=1}^{\infty} \sum_{j=i}^{\infty} \left[v_i^{cc} v_j^{cc} P(\boldsymbol{\theta}_j^{cc}, v_j^{cc}, t'; \boldsymbol{\theta}_i^{cc}, v_i^{cc}, t'') \hat{\mathbf{e}}(\boldsymbol{\theta}_j^{cc}) \cdot \hat{\mathbf{e}}(\boldsymbol{\theta}_i^{cc}) \right], \quad (5.12)$$

where v_i^{cc} and $\boldsymbol{\theta}_i^{cc}$ are the velocity and direction of motion of the center of mass in the i^{cc} -th tick of the **Collective Clock** respectively. We can rewrite the joint probability as a conditional probability given by $P(\boldsymbol{\theta}_j^{cc}, v_j^{cc}, t'; \boldsymbol{\theta}_i^{cc}, v_i^{cc}, t'') = P(\boldsymbol{\theta}_j^{cc}, v_j^{cc}, t' | \boldsymbol{\theta}_i^{cc}, v_i^{cc}, t'') P(\boldsymbol{\theta}_i^{cc}, v_i^{cc}, t'')$. In the long-time behavior, we can approximate the probability of finding the system in the i^{cc} -th tick by:

$$\lim_{t'' \rightarrow \infty} P(\boldsymbol{\theta}_i^{cc}, v_i^{cc}, t'') = \frac{1}{R_i^{cc} \langle T^{cc} \rangle}, \quad (5.13)$$

with $\langle T^{\text{cc}} \rangle$ the average period of the Collective Clock. Equation (5.12) is going to be simplified even more due to the fact that there is a change of direction everytime that the system reaches state 1^{cc} . This means that all terms where $i \leq 3N$ and $j > 3N$ will cancel. The final result is:

$$\langle \mathbf{x}_{cm}^2(t) \rangle = \int_0^t dt'' \int_0^{t''} dt' \sum_{i=1}^{3N} \sum_{j=i}^{3N} \left[\frac{v_i^{\text{cc}} v_j^{\text{cc}}}{R_i^{\text{cc}} \langle T^{\text{cc}} \rangle} P(v_j^{\text{cc}}, t' | v_i^{\text{cc}}, t'') \right]. \quad (5.14)$$

The conditional probabilities $P(v_j^{\text{cc}}, t' | v_i^{\text{cc}}, t'')$ can be obtained calculating first passage times in a similar way as the period distribution $P(T^{\text{cc}} = t)$ in equation (4.48). The general expression of these conditional probabilities is:

$$P(v_j^{\text{cc}}, t' | v_i^{\text{cc}}, t'') = \begin{cases} R_i^{\text{cc}} \exp \left[-R_i^{\text{cc}} \mathcal{T} \right] & \text{if } j = i, \\ \left(\prod_{k=i}^j R_k^{\text{cc}} \right) \int_0^{\mathcal{T}} dt_1 \dots \int_0^{\mathcal{T}-\tau_{(j-i)-1}} dt_{(j-i)} \exp \left[-\sum_{k=i}^{j-1} R_k^{\text{cc}} t_{(k-i+1)} - R_j^{\text{cc}} \left(\mathcal{T} - \tau_{(j-i)} \right) \right] & \text{if } j \geq i+1. \end{cases} \quad (5.15)$$

where $j \geq i$ and $\mathcal{T} = t' - t'' \geq 0$. We make use again of the auxiliary variable of equation (4.49) and the convention $\tau_0 = 0$. In the case of different transition rates and 1D we notice that the conditional probabilities $P(v_j^{\text{cc}}, t' | v_i^{\text{cc}}, t'')$ depend only on the difference of times \mathcal{T} , so we can express equation (5.14) as:

$$\langle x_{cm}^2(t) \rangle = 2 \sum_{i=1}^{3N} \sum_{j=i}^{3N} \frac{v_i^{\text{cc}} v_j^{\text{cc}}}{R_i^{\text{cc}} \langle T^{\text{cc}} \rangle} \left(\prod_{k=i}^{j-1} R_k^{\text{cc}} \right) \int_0^t ds \int_0^{t-s} d\mathcal{T} \sum_{k=i}^j \lambda_{jk} e^{-R_k^{\text{cc}} \mathcal{T}}, \quad (5.16)$$

with

$$\lambda_{jk} = \begin{cases} \frac{\lambda_{j-1k}}{R_j^{\text{cc}} - R_k^{\text{cc}}} & \text{if } j < k, \\ -\sum_{j=1}^{i-1} \lambda_{i,j} & \text{if } j = k, \\ 0 & \text{if } j > k. \end{cases} \quad (5.17)$$

For the long-time behavior we get the result:

$$\lim_{t \rightarrow \infty} \langle x_{cm}^2(t) \rangle = 2 \left(\sum_{i=1}^{3N} \sum_{j=i}^{3N} \frac{v_i^{\text{cc}} v_j^{\text{cc}}}{R_i^{\text{cc}} \langle T^{\text{cc}} \rangle} \left(\prod_{k=i}^{j-1} R_k^{\text{cc}} \right) \sum_{k=i}^j \frac{\lambda_{jk}}{R_k^{\text{cc}}} \right) t = 2 D^{\text{cc}} t. \quad (5.18)$$

The Metaparticle Clock Approximation

Given that in the MCA we approximate the dynamics of the whole system as the dynamics of only one particle, we need only to calculate $\langle \mathbf{x}_{mp}^2(t) \rangle$, where $\mathbf{x}_{mp}(t)$ is the position of the Metaparticle. For the calculation, we follow a similar path like the one used in the

CCA and with the use of the general equations (5.7) and (5.8), we can write the general expression for the mean squared displacement of the Metaparticle, which is:

$$\begin{aligned} \langle \mathbf{x}_{\text{mp}}^2(t) \rangle &= \int_0^t dt'' \int_0^t dt' \sum_{i=1}^3 \sum_{j=i}^3 \left[\frac{v_i^{\text{mp}} v_j^{\text{mp}}}{R^{\text{mp}} \langle T^{\text{mp}} \rangle} P(v_j^{\text{mp}}, t' | v_i^{\text{mp}}, t'') \right] \\ &= \frac{v_0^2}{R^{\text{mp}} \langle T^{\text{mp}} \rangle} \int_0^t dt'' \int_0^t dt' P(v_2^{\text{mp}}, t' | v_2^{\text{mp}}, t''), \end{aligned} \quad (5.19)$$

where we used that the velocity of the Metaparticle is $v_i^{\text{mp}} = v_0 \delta_{i,2}$ and that $R_1^{\text{mp}} = R_2^{\text{mp}} = R_3^{\text{mp}} = R^{\text{mp}}$. Performing the time integrals in (5.19) we get the final result:

$$\langle \mathbf{x}_{\text{mp}}^2(t) \rangle = 2 \left(\frac{v_0^2}{(R_2^{\text{mp}})^2 \langle T^{\text{mp}} \rangle} \right) t = 2 D^{\text{mp}} t. \quad (5.20)$$

5.1.2 Average dispersion around the center of mass $\langle \sigma_g^2 \rangle$

Using the CCA and the MCA

To calculate the dispersion of particles around the center of mass, we are going to use the two approximations (CCA and MCA) at the same time. Since we suppose that the three collective cascades between the states A , B and C are fast, we reduce the problem to a sequence of simpler problems. The first one is a system of N independent diffusing active particles that, in average, will diffuse for a time given by

$$\tau_{\text{diff}}(\beta, \gamma) = \frac{1}{R_1^{\text{cc}}} + \frac{1}{R_{N+1}^{\text{cc}}}. \quad (5.21)$$

The second is a system of N non-interacting active particles under the effect of an attracting drift toward the center of mass of the system for an average time given by

$$\tau_{\text{drift}}(\beta, \gamma) = \frac{1}{R_{2N+1}^{\text{cc}}}. \quad (5.22)$$

In the following, we solve each one of these two problems in detail for the general case of n dimensions.

Problem 1: a system of N non-interacting diffusing active particles.

In this case the Langevin equation of each particle in n dimensions is:

$$\dot{\mathbf{x}}_i(t) = \sqrt{2D_0} \boldsymbol{\xi}_i(t). \quad (5.23)$$

This is a system of N non-interacting diffusing active particles. To calculate $\langle \sigma_g^2(t) \rangle$ we need to calculate first $\langle \mathbf{x}_{\text{cm}}^2(t) \rangle$. By definition, the center of mass is:

$$\mathbf{x}_{\text{cm}}(t) = \frac{1}{N} \sum_{i=1}^N \mathbf{x}_i(t). \quad (5.24)$$

In the one dimensional case ($n = 1$) case we have:

$$x_{cm}^2(t) = \frac{1}{N^2} \left(\sum_{i=1}^N \sqrt{2D_0} \int_0^t d\omega_i \right) \left(\sum_{j=1}^N \sqrt{2D_0} \int_0^t d\omega_j \right). \quad (5.25)$$

If we calculate the average of this equation and use the properties of the white noise, we have:

$$\langle x_{cm}^2(t) \rangle = \frac{2D_0}{N^2} \sum_{i=1}^N \sum_{j=1}^N \int_0^t \int_0^t \langle d\omega_i d\omega_j \rangle = \frac{2D_0}{N^2} Nt = \frac{2D_0}{N} t. \quad (5.26)$$

The generalization to two dimensions ($n = 2$) requires a multiplication by a factor of 2 since $\langle \mathbf{x}_{cm}^2 \rangle = \langle x_{cm}^2(t) + y_{cm}^2(t) \rangle$, with both components being independent from each other. So, the result is

$$\langle \mathbf{x}_{cm}^2(t) \rangle = \frac{4D_0}{N} t. \quad (5.27)$$

The dispersion of particles around the center of mass is defined in n dimensions as:

$$\sigma_g^2(t) = \frac{1}{N} \sum_{i=1}^N \left(\mathbf{x}_i(t) - \mathbf{x}_{cm}(t) \right)^2. \quad (5.28)$$

We can rewrite this expression in more simple terms:

$$\begin{aligned} \sigma_g^2(t) &= \frac{1}{N} \left(\sum_{i=1}^N \mathbf{x}_i^2(t) - 2 \mathbf{x}_{cm} \cdot \sum_{i=1}^N \mathbf{x}_i(t) + \mathbf{x}_{cm}^2(t) \sum_{i=0}^N 1 \right) \\ &= \frac{1}{N} \left(\sum_{i=1}^N \mathbf{x}_i^2(t) - 2N \mathbf{x}_{cm} \cdot \mathbf{x}_{cm} + N \mathbf{x}_{cm}^2(t) \right) \end{aligned} \quad (5.29)$$

Rearranging the terms and taking the average we obtain the result:

$$\langle \sigma_g^2(t) \rangle = \frac{1}{N} \sum_{i=1}^N \langle \mathbf{x}_i^2(t) \rangle - \langle \mathbf{x}_{cm}^2(t) \rangle. \quad (5.30)$$

In this expression, the only term we have not calculated yet is $\langle \mathbf{x}_i^2(t) \rangle$. This can be easily calculated as follows in $n = 1$ dimension:

$$x_i(t) = \sqrt{2D_0} \int_0^t d\omega_i(t) \quad \Rightarrow \quad x_i^2(t) = 2D_0 \int_0^t \int_0^t d\omega_i(t') d\omega_i(t'') \quad \Rightarrow \quad \langle x_i^2(t) \rangle = 2D_0 t. \quad (5.31)$$

In $n = 2$ dimensions, the result is $\langle \mathbf{x}_i^2(t) \rangle = 4 D_0 t$. Hence, we can write finally the final expression:

$$\begin{aligned} \langle \sigma_g^2(t) \rangle &= \frac{1}{N} \sum_{i=1}^N (2 D_0 t) - \frac{2 D_0 t}{N} = \left(1 - \frac{1}{N}\right) 2 D_0 t && \text{for 1D,} \\ \langle \sigma_g^2(t) \rangle &= \frac{1}{N} \sum_{i=1}^N (4 D_0 t) - \frac{4 D_0 t}{N} = \left(1 - \frac{1}{N}\right) 4 D_0 t && \text{for 2D,} \\ \langle \sigma_g^2(t) \rangle &= \left(1 - \frac{1}{N}\right) 2 n D_0 t && \text{for nD.} \end{aligned} \quad (5.32)$$

Problem 2: N independent Ornstein-Uhlenbeck processes.

In this case the Langevin equation of each particle in n dimensions is:

$$\dot{\mathbf{x}}_i(t) = \Gamma_0 \left(\mathbf{x}_{cm}(t) - \mathbf{x}_i(t) \right) + \sqrt{2 D_0} \boldsymbol{\xi}_i(t). \quad (5.33)$$

This is a system of N diffusing active particles subject to an attracting drift toward the center of mass. Since we are interested in calculating $\langle \sigma_g^2(t) \rangle$, we can approximate this problem to the problem of N non-interacting particles with the equation of motion:

$$\dot{\mathbf{x}}(t) = \Gamma_0 \left(\langle \mathbf{x}_{cm}(t) \rangle - \mathbf{x}(t) \right) + \sqrt{2 D_0} \boldsymbol{\xi}(t), \quad (5.34)$$

known as the Ornstein-Uhlenbeck process. The corresponding Fokker-Planck equation in $n = 1$ dimension is

$$\partial_t P(x, t) = \partial_x \left[\Gamma_0 \left(x - \langle x_{cm} \rangle \right) P(x, t) \right] + \partial_{xx} \left[D_0 P(x, t) \right]. \quad (5.35)$$

We use the change of variable $u = x - \langle x_{cm} \rangle$ to simplify the equation, which becomes:

$$\partial_t P(u, t) = \partial_u \left[\Gamma_0 u P(u, t) \right] + \partial_{uu} \left[D_0 P(u, t) \right]. \quad (5.36)$$

Using the Fourier Transform, defined as

$$\mathcal{F} \left\{ P(u, t) \right\} = \hat{P}(q, t) = \int_{-\infty}^{\infty} du P(u, t) e^{-iq u}, \quad (5.37)$$

then equation (5.36) simplifies to

$$\partial_t \hat{P}(q, t) = -\Gamma_0 q \partial_q \hat{P}(q, t) - q^2 D_0 \hat{P}(q, t). \quad (5.38)$$

The solution of this equation is

$$\hat{P}(q, t) = \exp \left(-i q u_0 e^{-\Gamma_0 t} + \frac{q^2 D_0}{2 \Gamma_0} \left[1 - e^{-2 \Gamma_0 t} \right] \right), \quad (5.39)$$

with u_0 the initial condition. Expression (5.39) can be inverted and the result is:

$$P(x, t|x_0, 0) = \frac{1}{\sqrt{\frac{2\pi D_0}{\Gamma_0} (1 - e^{-2\Gamma_0 t})}} \exp \left[-\frac{\left((x - \langle x_{cm} \rangle) - (x_0 - \langle x_{cm} \rangle) e^{-\Gamma_0 t} \right)^2}{\left(\frac{2\pi D_0}{\Gamma_0} \right) (1 - e^{-2\Gamma_0 t})} \right]. \quad (5.40)$$

From equation (5.40) we can read the expression for $\langle \sigma_g^2(t) \rangle$. For the whole system of N independent active particles, the result is:

$$\begin{aligned} \langle \sigma_g^2(t) \rangle &= \frac{D_0}{\Gamma_0} \left(1 - e^{-2\Gamma_0 t} \right) \left(1 - \frac{1}{N} \right) && \text{for 1D,} \\ \langle \sigma_g^2(t) \rangle &= \frac{2 D_0}{\Gamma_0} \left(1 - e^{-2\Gamma_0 t} \right) \left(1 - \frac{1}{N} \right) && \text{for 2D,} \\ \langle \sigma_g^2(t) \rangle &= \frac{n D_0}{\Gamma_0} \left(1 - e^{-2\Gamma_0 t} \right) \left(1 - \frac{1}{N} \right) && \text{for nD.} \end{aligned} \quad (5.41)$$

The result

Weighing the results of equations (5.32) and (5.41) with the corresponding times τ_{diff} and τ_{drift} we get an expression for the average dispersion of the particles around the center of mass:

$$\langle \sigma_g^2 \rangle = \langle \sigma_1^2(\tau_{\text{diff}}) \rangle \frac{\tau_{\text{diff}}}{\langle T^{\text{cc}} \rangle} + \langle \sigma_2^2(\tau_{\text{drift}}) \rangle \frac{\tau_{\text{drift}}}{\langle T^{\text{cc}} \rangle}. \quad (5.42)$$

5.2 Discussion and results

To make a systematic and quantitative study of how good or bad are the both approximations, we define two parameters:

$$\begin{aligned} \mathcal{E}_2^{\text{cc,mp}}(\beta, \gamma) &= 1 - \frac{\min \left\{ D^{\text{cc,mp}}(\beta, \gamma), D^{\text{ibm}}(\beta, \gamma) \right\}}{\max \left\{ D^{\text{cc,mp}}(\beta, \gamma), D^{\text{ibm}}(\beta, \gamma) \right\}}, \\ \mathcal{E}_3^{\text{cc}}(\beta, \gamma) &= 1 - \frac{\min \left\{ \langle \sigma_g^2(\beta, \gamma) \rangle^{\text{cc}}, \langle \sigma_g^2(\beta, \gamma) \rangle^{\text{ibm}} \right\}}{\max \left\{ \langle \sigma_g^2(\beta, \gamma) \rangle^{\text{cc}}, \langle \sigma_g^2(\beta, \gamma) \rangle^{\text{ibm}} \right\}} \end{aligned} \quad (5.43)$$

with $\langle \cdot \rangle^{\text{ibm}}$ the average observables calculated with IBM simulations of the system. These parameters are defined analogously to parameter \mathcal{E}_1 in equation (4.59) of Chapter 4. Due to the definitions of the parameters in equation (5.43), a value of $\mathcal{E}_i(\beta, \gamma) \approx 0$ for a given β and γ is telling us that the approximation (either CCA, MPA or both) is good. On the other hand, the case of $\mathcal{E}_i(\beta, \gamma) \rightarrow 1$ tells us that the approximation is not accurate. From parameter $\mathcal{E}_2(\beta, \gamma)$ we can obtain information about the exploration of the space by the whole group. A difference of parameter $\mathcal{E}_2(\beta, \gamma)$ with respect to $\mathcal{E}_1(\beta, \gamma)$ in equation (4.59)

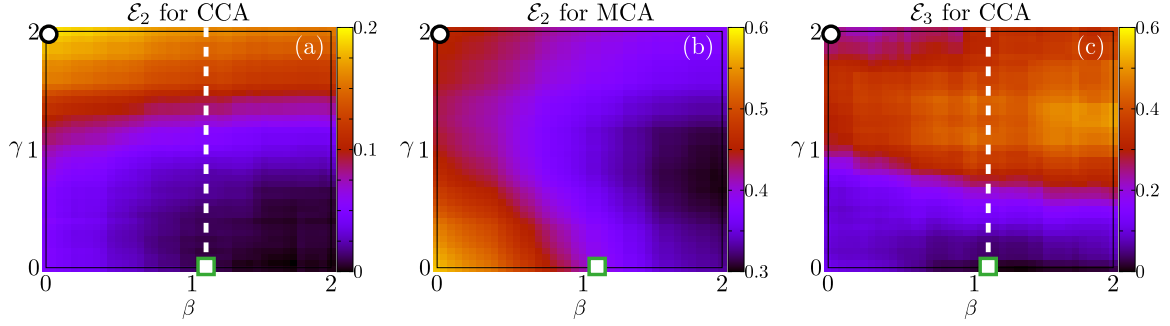


Figure 5.3 – Plots of the values of the parameters $\mathcal{E}_2(\beta, \gamma)$ and $\mathcal{E}_3(\beta, \gamma)$ in the region of interest, namely $\beta \in [0, 2]$ and $\gamma \in [0, 2]$. Plots (a) and (b) show the numerical results of parameter \mathcal{E}_2 for the CCA and the MCA respectively. We observe in plot (c) that the region for low values of \mathcal{E}_3 is smaller than the previous parameters, namely for roughly $\beta > 1$ and $\gamma < 0.35$. The parameters of the system are the same as Figure 5.2.

is that the results for the CCA and the MPA are not the same anymore. In this case we can see in Figure 5.3b that the CCA approximates in a good way the IBM simulations in roughly the same region that the parameter $\mathcal{E}_1(\beta, \gamma)$, namely $\beta > 1$ and $\gamma < 1$. This is not the case for the MPA, that globally is less accurate than the CCA. Nonetheless there is a region for $\beta > 1.5$ and $0.5 \leq \gamma \leq 1.5$ where accuracy of the MPA is not that bad. Regarding the information of the cohesion of the group, we can obtain information of the accuracy of the CCA with $\mathcal{E}_3(\beta, \gamma)$. In this case, we notice that the CCA is a good approximation in the region of high synchronization.

Hence, once again, the CCA proves to give accurate results in the region of high synchronization. To have a better idea on the accuracy of the CCA and the MCA, we compare these approximations with the IBM simulations. We use the same two sets of parameters of Figure 5.2 to compare the synchronized and the unsynchronized scenarios. In Figure 5.4a and b, we plot the average mean square displacement $\langle (\mathbf{x}_{cm}(t) - \mathbf{x}_{cm}(0))^2 \rangle$ and the average dispersion $\langle \sigma_g^2(t) \rangle$ and compare them with the predictions of the CCA and the MCA. The CCA and MCA result to be accurate in the synchronized case. In Figure 5.4c and d we compare the results of the IBM simulations with the CCA and the MCA as function of parameter γ and fixing the parameter β . This corresponds to cuts in the parameter diagrams and are depicted with white-dashed lines in Figure 5.3a and c.

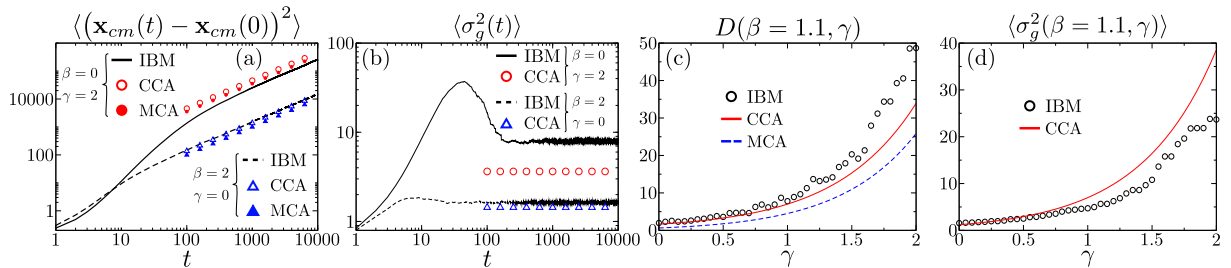


Figure 5.4 – Plots in (a) and (b) show the comparison of $\langle (\mathbf{x}_{cm}(t) - \mathbf{x}_{cm}(0))^2 \rangle$ and $\langle \sigma_g^2(t) \rangle$ with the CCA and MCA for the two sets of parameters used also in Figure 5.2. Plot (c) and (d) show the diffusion coefficient and the average dispersion of particles around the center of mass as function of parameter γ for a fixed value of $\beta = 1.1$, which correspond to the white-dashed lines of plots (a) and (c) of Figure 5.3. The system size is $N = 10$.

In this discussion, we want also to analyse the effect of introducing a radius of interaction r_0 . The main effect of using a radius is the possibility of loosing the coherence of the group. In the extreme case of using a small value for r_0 and in the long-time behavior, we would have a total incoherent group of N independent particles with internal dynamics given by constant rates. In this case, we can give expressions for the transport properties of the group. The mean squared displacement of the group results to be

$$\lim_{t \rightarrow \infty} \langle x_{cm}^2(t) \rangle = 2 \left(\frac{D_{\text{eff}}}{N} \right) t, \quad (5.44)$$

and the average dispersion of particles around the center of mass is

$$\lim_{t \rightarrow \infty} \langle \sigma_g^2(t) \rangle = 2 \left(1 - \frac{1}{N} \right) D_{\text{eff}} t, \quad (5.45)$$

with $D_{\text{eff}} = \frac{v_0^2}{3\omega} + D_0$. More details on the derivation of both quantities can be found in the Appendix D. We propose two ways to estimate numerically a sort of critical radius that tells us when a group of particles stays cohesive. A first estimation can be done using the average dispersion of particles around the center of mass,

$$(r_c^{\text{down}})^2 = \frac{1}{T_{\text{obs}}} \int_0^{T_{\text{obs}}} \sigma_g^2(t) dt, \quad (5.46)$$

which is a time average over the whole observation time. A better estimation is done using the average over realizations of the maximum value of $\sigma_g^2(t)$ in the whole observation window:

$$(r_c^{\text{up}})^2 = \langle \max\{\sigma_g^2(t) | 0 \leq t \leq T_{\text{obs}}\} \rangle_r, \quad (5.47)$$

where $\langle \cdot \rangle_r$ denotes an average over realizations. In Figure 5.5 we show the numerical results for a group size $N = 4$ and $\beta = 1.1$.

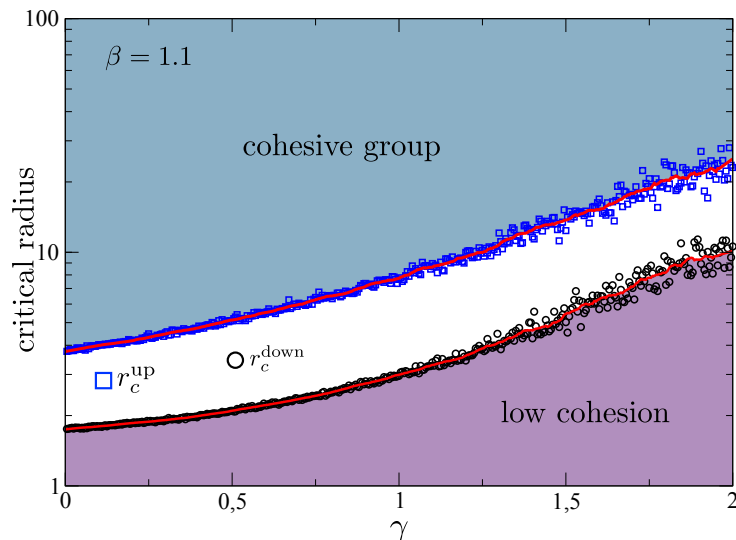


Figure 5.5 – We show the two radii r_c^{up} and r_c^{down} that are explained in the text for given parameters $\beta = 1.1$, $\omega = 0.1$ and varying $\gamma \in [0, 2]$. We notice that r_c^{up} and r_c^{down} are small in the region of high degree of synchronization and increase in the region of low degree of synchronization. The used parameters are $N = 4$, $\beta = 1.1$, $v_0 = 1$ and $\Gamma_0 = 1$.

This results suggest that using a radius $r_0 < r_c^{\text{down}}$ will most probably lead to a group with low degree of cohesion and, in the long-time behavior, to a completely incohesive group with transport properties given by (5.44) and (5.45). On the other hand, using a radius $r_0 > r_c^{\text{up}}$ will maintain the group cohesive also in the long time behavior and thus all the results explained in this chapter will hold true.

We can also study what happens to the system if we use a given value of r_0 and explore the coherence for different values of the parameters β and γ . The results will evidently depend on the value of r_0 . The resulting exploration of the parameter space using IBM simulations can be found in Figure 5.6.

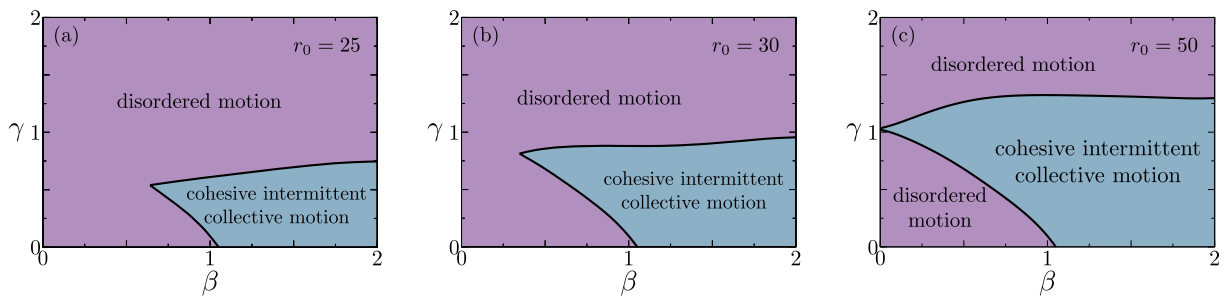


Figure 5.6 – Parameter exploration for several values of the radius r_0 . We notice two different behaviors: either cohesive intermittent collective motion or disordered motion. The IBM simulations were performed using parameters $N = 4$, $\omega = 0.1$, $v_0 = 1$ and $\Gamma_0 = 1$.

5.3 Summary & perspectives

In this chapter we studied in detail the spatial dynamics of a system of N interacting active particles with three internal states and we used the knowledge acquired in the past chapter, where we analyzed the mean field dynamics and introduced two new and general concepts: the **C**ollective **C**lock **A**pproximation (CCA) and the **M**etaparticle **C**lock **A**pproximation (MCA). We used them to give analytical expressions for the transport properties of the group and compared them with **I**ndividual **B**ased **M**odel (IBM) simulations. Once again, like in the previous chapter, the CCA and MCA result to be good approximations in the region of high synchronization. The results and concepts presented in this chapter can be easily generalized for other systems of particles that present intermittent collective behaviors with a high degree of synchronization. These results prove to be useful when studying biological systems of individuals that move in space while forming cohesive groups, like gregarious animals.

Chapter 6

Conclusions

In this thesis we introduce a theoretical framework to understand collections of active particles that operate with a finite number of discrete internal states that control the external behavior of these entities. The theoretical concepts developed in this thesis are conceived to understand the large number of existing multiagent biological systems where the individuals display distinct behavioral phases that alternate with each other. Examples of this are, among many others, the change of direction of motion in the presence of an external chemical $c(\mathbf{x})$ in bacteria – called chemotaxis – and the alternating, collective phases of rest and activity – involving collective displacements – displayed by group-living animals. Despite the fact that the phenomenology observed in the provided examples is of different nature, we show in Chapter 2 that the behavior of these biological systems is controlled by a reduced number of internal states.

By construction, the premise of our theoretical model is that an external observer has access only to the external behavior of the individuals, but not to their internal state. It is only after careful examination of the behavioral dynamics – involving experimental measurements and data analysis – that the existence of these internal states becomes evident. This analysis is key to be able to associate the experimentally observed behaviors of individuals with one or many internal states of the model. This association between states and behaviors should be done accordingly to the observations and the phenomenology displayed by the biological system that is being the subject of study. A small scheme of this is shown in Figure 6.1.

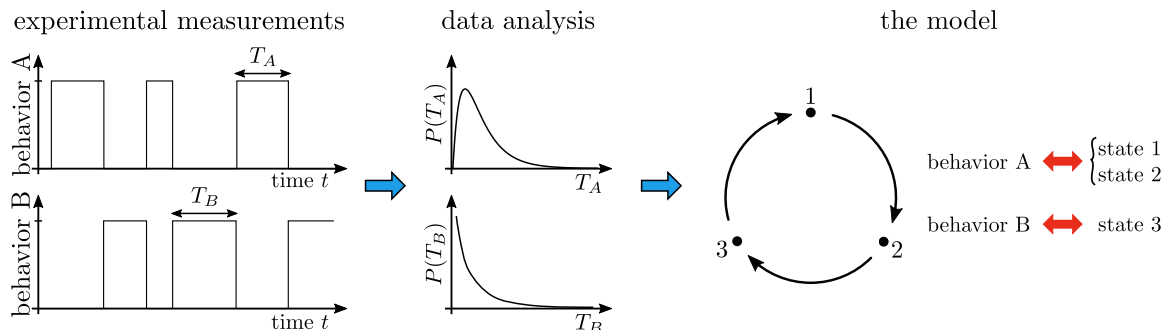


Figure 6.1 – Left: experimental measurements of the different behaviors of the individuals of the system. Center: data analysis on the experimental measurements. Right: association of the behaviors observed in experiments with the internal states of the model, done accordingly to the data analysis and the observed phenomenology of the system.

The possible scenarios that can be observed using our theoretical model are determined by the design of what we have called internal mechanism of the individuals (number of internal states, allowed transitions among these states, etc . . .). Note that by construction, it is assumed that the resulting dynamics is of Markovian nature. Furthermore, we assume that the transition rates may depend on the internal states of neighboring particles as well as external signals introducing in this way the possibility of particle-particle behavioral – e.g. social – interactions in addition to the potential presence of standard physical interaction, e.g. forces. This undoubtedly opens the door to a large spectrum of potential complex behaviors at the individual and collective level, such as adaptive chemotactic behavior or intermittent collective motion by coupling an underlying Markov chain – which controls the internal dynamics of the individuals – with a set of equations of motion that dictates the spatial dynamics of the individuals.

In Chapter 2 we provide evidence of the existence of biological systems where the observed intermittent behaviors at the individual and collective levels can be explained using simple designs of our model. In the case of the microscopic bacterial system we can conclude that the experimental measurements and spatio-temporal dynamics are consistent with a model where the individuals have two internal states and its change of direction is regulated by local external information. This corresponds to one of the simplest scenarios of our model since the particles do not interact with each other in any way. With the intention of having a better understanding of the general phenomenology contained in this case, we study in Chapter 3 the possible scenarios that can be described with this model. We demonstrate that complex behaviors like adaptive chemotaxis, detection of maxima, minima or selected values of a given external signal $c(\mathbf{x})$ are possible scenarios and are only determined by the design of the internal states of the particles. We expect that this analysis will shed light on alternative chemotactic strategies in bacteria.

In the case of the macroscopic system of the sheep, we conclude that the observations are consistent with a model where the individuals have three internal states and the change of behavior depends on the behaviors of the rest of the members of the group. This corresponds to the simplest case of our model where we can observe we have called intermittent collective motion: i.e. collective motion of a group, where motion occurs in bursts of activity, while otherwise the group remains static. Analogously to the previous case, we study in full detail the spatio-temporal dynamics of the group of N particles in Chapter 4 and Chapter 5. We put special attention to highly synchronized cases, where we develop two new theoretical concepts: the **Collective Clock** and the **Metaparticle Clock**. These two concepts prove to be useful to obtain analytical approximations for the collective transport properties of any group of active particles showing a high degree of synchronization.

In summary, all the experimental and theoretical work contained in this thesis is evidence that our model is suitable to be used to describe real-life systems showing individual or collective intermittency. We also show that the phenomenology contained in our model is determined by the design of the internal states of the individuals and can describe real-life scenarios spanning over several scales. This here-introduced new framework of active particles with internal states is still in development and we are convinced that it can potentially open new branches of research that will be able to link physics, biology, experiments and mathematics at the same time.

Appendix A

Methods and data acquisition for merino sheep and *Pseudomonas Putida*

In this appendix we detail the experimental methods and the data collection used for the small groups of merino sheep, as well as the experiments with *P. Putida*.

A.1 *Pseudomonas Putida*

P. putida KT2440 was streaked on 1.5% agar (AppliChem, Germany) containing LB medium (AppliChem, Germany) and grown at 30 °C. A single-colony isolate was used to inoculate 10 ml of M9 medium [68] supplemented with 5 mM sodium benzoate as a carbon source [62]. The culture was grown for 36 h on a rotary shaker (300 min⁻¹, 30 °C) to stationary phase. It then was diluted 1:100 into 25 ml of fresh M9 medium and grown 12 h to an OD₆₀₀ of ≈ 0.3 in exponential phase. Bacteria were washed three times by centrifugation at 1000g for 10 min and carefully resuspended in 10 ml motility buffer (1 $\times 10^{-2}$ M potassium phosphate, 6.7 $\times 10^{-2}$ M NaCl, 1 $\times 10^{-4}$ M EDTA and 0.5%w/v glucose; pH 7.0). Cells were diluted further to an OD of 0.05 before filling them into the chemotaxis device.

A.1.1 Microfluidics and imaging

We used a μ -Slide Chemotaxis 3D (ibid., Martinsried, Germany) to generate stable linear gradients of benzoate. Filling was performed as detailed in [3] with concentrations in the source and sink reservoir of 0.5 mM and 5 mM sodium benzoate, respectively. Imaging was done using an IX71 inverted microscope with a 20 \times UPLFLN-PH objective (both Olympus, Germany) in phase contrast mode with an attached Orca Flash 4.0 CMOS camera (Hamamatsu Photonics, Japan). Video data was acquired for two minutes at 20 Hz, approximately one hour after filling the channel. The gradient linearity and stationarity was checked previously [3]. The viewport and focal plane were set in the center of the channels observation region, about 35 μ m from top and bottom. Image processing and tracking was performed as previously described in [3].

A.1.2 Filtering and smoothing

To filter out damaged, non-motile cells and those swimming on very wobbly trajectories, we discarded tracks based on a number of criteria. Tracks below a mean speed of $5 \mu\text{m s}^{-1}$, longer than 20 s, above the 80th percentile of median curvature and with a total displacement below $5 \mu\text{m}$ are discarded. To further smooth these tracks, we applied a 3 point, second order Savitzky-Golay filter. Because tracks often begin or end with a reversal we cut off the first and last 0.5 s of each recorded track in order to avoid any bias in the measured run times.

A.1.3 Run-and-tumble recognition

Characterization of reversal events was performed with the algorithm of [63]. In short, this algorithm determines reversals by evaluating local extrema in the speed and turn rate time series and counting a reversal for sufficiently deep peaks and troughs in speed or height.

A.2 Merino sheep

The experiments were performed at the experimental farm of Domaine du Merle (5.74E and 48.50N) in the south of France. Data were collected in a period of 18 days. Small groups of Arles Merino sheep were used: two, three, four and, eight individuals. On each day of the experiment, the group was allocated in a visually isolated arena and left there for half an hour. The arena was a fenced square ($80\text{m} \times 80\text{m}$) in a field of native wet Crau meadow, mainly covered by graminoids, clover *Trifolium* sp. and plantain *Plantago lanceolata*. The animals had a familiarization time with their groups in a waiting area of the same pasture, after which they were introduced into the arena. Simultaneous video recording of the arena took place using a digital camcorder (Sony DCR-TRV950 E) anchored at the top of a 7m high tower and connected to a PowerBook laptop. The laptop was programmed to take a snapshot from the camcorder every second. All group size-experiments were replicated several times.

A.2.1 Data collection

Once having the images, the next step was to extract the information from them. The use of automatic tracking of individuals was not an option because of several difficulties. The fluctuations of the contrast between sheep and background are high and the recording angle of the camcorder with respect to the arena made possible that sheep frequently hide each other from the camera viewpoint. That is why we had to use manual tracking on a Cintiq interactive pen display [Cintiq 21 UX (UXGA $1,600 \times 1,200$ pixels)] using dedicated software written by J. Gautrais, academic researcher at the Centre de Recherche sur la Cognition Animale of the University of Toulouse. By manually tracking the images, we obtained the tail and head positions for each sheep inside the arena. This allowed us to have the position $\mathbf{r}_i(t)$ and heading $\mathbf{s}_i(t)$ for each individual. The instantaneous velocity $\mathbf{v}_i(t) = (\mathbf{r}_i(t + \Delta t) - \mathbf{r}_i(t))/\Delta t$ of each sheep was obtained by marking their positions in two consecutive images.

We noticed that from the experimental images, we could also obtain comportamental information of the individuals. In the software, it was also possible to mark for each image if the individual sheep had the head up or down, two comportamental states that were easy to distinguish in the images. This resulted to be very valuable information at the moment of presenting the model.

To summerize, the information we obtained for each sheep was the position $\mathbf{r}_i(t)$, the heading $\mathbf{s}_i(t)$, the velocity $\mathbf{v}_i(t)$ and the comportamental state. All this information was obtained for each second for groups of size $N = 2, 3, 4$. For groups of size $N = 8$, the tracking was made each second for one selected individual and every 60 seconds for the whole group.

Appendix B

Markovian robots

B.1 Individual-based model (IBM) simulations

IBM simulations using $N = 10^4$ robots were performed in order to check the validity of analytical approximations in the context of the reduction of the Master equation onto the Fokker-Planck dynamics. The state of a robot is characterized by three variables: its position, its direction of active motion and the internal state depending on the motif under consideration. For motif 1, for example, the internal state can take the values 1 and 2. The spatial dynamics [Eq. (3.1)] was solved by a stochastic Euler-Maruyama method [43] with a time step $\Delta t = 0.01$. The occurrence of reversal events are dictated by the internal variable as follows. We implemented the evolution of the internal state using random numbers, which are uniformly distributed between 0 and 1. In each time step and for each robot, a transition in the motif was triggered if the random number is smaller than the product of the numerical time step Δt and the respective transition rate. Only one particular transition is accompanied by reversal, depicted by a dashed red arrow in each motif in Fig. 3.1. To get the stationary density distribution $P_s(x)$, a histogram of robot positions was averaged over time. The total observation time was fixed to $t_{obs} = 20\,000$ to ensure relaxation towards the stationary state.

B.2 Numerical solution of master equations

Individual-based simulations were validated by the direct integration of the Master equations [Eqs. (3.2) and (3.10)] corresponding to the NCS motif under consideration. Furthermore, the response of MR to a dynamic field gradient was performed numerically on the basis of the respective system of Master equations, cf. Fig. 3.4. To solve those Master equations, a central finite difference discretization was employed in space and the temporal integration was performed using an explicit forward Euler algorithm [69]. In particular, the spatial discretization $\Delta x = 10^{-2}$ and temporal time step $\Delta t = 10^{-3}$ was used in the context of Fig. 3.4.

B.3 Drift-diffusion approximation in 1D

In the main text, the derivation of position-dependent drift and diffusion from the full set of master equations is briefly sketched. In this paragraph, technical details of this derivation are presented in more detail for the one-dimensional case. Along with the general discussion of the principal ideas behind this derivation, NCS motif 1 is considered as an example. Effective Langevin equations for more complicated cases follow from the same procedure in a similar way.

Starting from the full Master equation for the probabilities $P_i^\pm(x, t)$ [cf. Eqs. (3.10) for example], the change of variables $P_i(x, t) = P_i^+(x, t) + P_i^-(x, t)$ and $m_i(x, t) = P_i^+(x, t) - P_i^-(x, t)$ is performed as a first step, allowing to recast the Master equation into two subgroups for the densities $P_i(x, t)$ and the differences $m_i(x, t)$ [cf. Eqs. (3.11)]:

$$\partial_t P_i = -v_0 \partial_x m_i + D_0 \partial_x^2 P_i - \mathcal{Q}_{ij}[c] P_j, \quad (\text{B.1a})$$

$$\partial_t m_i = -v_0 \partial_x P_i + D_0 \partial_x^2 m_i - \mathcal{M}_{ij}[c] m_j. \quad (\text{B.1b})$$

Henceforward, Einsteins sum convention is used for the sake of compact notation. In the case of NCS motif 1, the local transitions between the internal states are accounted for by the following matrices:

$$\mathcal{Q}[c] = \begin{pmatrix} \alpha[c] & -\beta[c] \\ -\alpha[c] & \beta[c] \end{pmatrix}, \quad \mathcal{M}[c] = \begin{pmatrix} \alpha[c] & \beta[c] \\ -\alpha[c] & \beta[c] \end{pmatrix}. \quad (\text{B.2})$$

We begin the analysis with the dynamics of the differences $m_i(x, t)$, given by Eq. (B.1b). The terms appearing are essentially of different types: there is a $m_i(x, t)$ -independent source term proportional to the derivative of the densities $P_i(x, t)$, diffusion of $m_i(x, t)$ as well as local transitions. Now, diffusion is a slow process as compared to the exponential relaxation, which is described by the local transitions. Particularly, the real part of the eigenvalues $\lambda_{\mathcal{M}}^{(\pm)}$ of the matrix \mathcal{M} , given by

$$\lambda_{\mathcal{M}}^{(\pm)} = \frac{1}{2} \left[\alpha + \beta \pm \sqrt{\alpha^2 - 6\alpha\beta + \beta^2} \right], \quad (\text{B.3})$$

are strictly larger than zero for all positive rates. Accordingly, Eq. (B.1b) describes relaxation towards a stationary state. Assuming that this relaxation is a fast process, one may eliminate the variables $m_i(x, t)$ adiabatically via $\partial_t m_i \approx 0$. This yields the constitutive equation

$$\mathcal{M}_{ij} m_j \approx -v_0 \partial_x P_i + D_0 \partial_x^2 m_i. \quad (\text{B.4})$$

Since non of the eigenvalues of \mathcal{M} equals zero, the matrix \mathcal{M} is invertible:

$$m_i \approx -v_0 \{ \mathcal{M}^{-1} \}_{ij} \partial_x P_j + D_0 \{ \mathcal{M}^{-1} \}_{ij} \partial_x^2 m_j. \quad (\text{B.5})$$

A closed expression for $m_i(x, t)$ in terms of $P_i(x, t)$ can be found by recursive reinsertion on the right hand side. With regard to the objective of this derivation, we turn now, however, to the $P_i(x, t)$ -dynamics [Eq. (B.1a)]. Notably, we want to obtain a closed equation up to second order in spatial derivatives. The $P_i(x, t)$ -dynamics is driven by first order derivatives of $m_i(x, t)$, which is, in turn, proportional to derivatives of $P_i(x, t)$

to lowest order. Hence, it is sufficient to truncate the recursion [Eq. (B.5)] at the lowest order in spatial derivatives:

$$m_i \approx -v_0 \{ \mathcal{M}^{-1} \}_{ij} \partial_x P_j. \quad (\text{B.6})$$

Accordingly, we obtain the following expression for the dynamics of $P_i(x, t)$ as an intermediate result:

$$\partial_t P_i = \partial_x \left[\left(v_0^2 \{ \mathcal{M}^{-1} \}_{ij} + D_0 \delta_{ij} \right) \partial_x P_j \right] - \mathcal{Q}_{ij}[c] P_j. \quad (\text{B.7})$$

The dynamics is a combination of position-dependent diffusion as well as local transitions between the different internal states.

In contrast to the matrix \mathcal{M} , the matrix \mathcal{Q} possesses always one eigenvalue which equals zero. It results from the fact that the robot must be in one of its internal state. This *conservation law* implies a zero-eigenmode corresponding the slow dynamics of the total, conserved density $P(x, t) = \sum_i P_i(x, t)$. Other eigenvalues are positive implying the existence of additional fast modes (notice the minus sign in front of \mathcal{Q}_{ij} in Eq. (B.7)). The two eigenvalues of the matrix \mathcal{Q} read $\lambda_{\mathcal{Q}}^{(1)} = \alpha + \beta$ and $\lambda_{\mathcal{Q}}^{(2)} = 0$ for NCS motif 1 for example, cf. Eq. (B.2). To lowest order in spatial gradients, the adiabatic elimination of the fast mode reveals that $P_i(x, t)$ must be element of the kernel of \mathcal{Q} :

$$\mathcal{Q}_{ij} P_j \approx 0. \quad (\text{B.8})$$

Physically, this reflects the assumption of local equilibrium implying that the local transitions are much faster compared to the motion of robots such that the local distribution of robots among the different internal states is equalized. This is in line with the general scope of this work: the external signal is weakly space-dependent, i.e. the field $c(x)$ varies on scales which are much larger than the mean distance $l_b = v_0 \tau$, which a robot travels in between two reorientation events that occur at an average rate τ^{-1} ; in short, only local measurements of the external signal are feasible. Consequently, the $P_i(x, t)$ -dynamics can relax locally faster than the overall density distribution on scales larger than l_b .

There is a nontrivial solution $P_i(x, t) = P(x, t) V_i[c]$ to Eq. (B.8) since the matrix \mathcal{Q} is not invertible¹. This solution is, however, unique due to the normalization condition $P(x, t) = \sum_i P_i(x, t)$ which implies necessarily that the sum of the components of the vector $\mathbf{V}[c]$ equals one. For the example of NCS motif 1 considered above, we obtain

$$\mathbf{V}[c] = \frac{1}{\alpha[c] + \beta[c]} \begin{pmatrix} \beta[c] \\ \alpha[c] \end{pmatrix}. \quad (\text{B.9})$$

Inserting this closure into the reduced $P_i(x, t)$ -equation [Eq. (B.7)] and subsequent summation over all components yields eventually the following closed equation for the total density:

$$\partial_t P = \sum_{i,j} \partial_x \left\{ \left(v_0^2 \{ \mathcal{M}^{-1} \}_{ij} + D_0 \delta_{ij} \right) \partial_x [P(x, t) V_j[c]] \right\}. \quad (\text{B.10})$$

¹The existence of a unique, nontrivial, stationary solution for this type of Master equation, which reflects the transition dynamics in between the internal states, is ensured in general [44].

In order to read of the mean drift $f(x)$ as well as the position-dependent diffusion coefficient $D(x)$, terms have to be rearranged to meet the structure of a Fokker-Planck equation in Ito form [43]:

$$\partial_t P(x, t) = -\partial_x \left[f(x) P(x, t) \right] + \partial_x^2 \left[D(x) P(x, t) \right].$$

From this Fokker-Planck equation, which defines $f(x)$ and $D(x)$ unambiguously, we read off

$$f(x) = v_0^2 \sum_{i,j} \left(\partial_x \{ \mathcal{M}^{-1} \}_{ij} \right) V_j[c],$$

$$D(x) = D_0 + v_0^2 \sum_{i,j} \{ \mathcal{M}^{-1} \}_{ij} V_j[c].$$

Inserting the inverse of \mathcal{M} for NCS motif 1,

$$\mathcal{M}^{-1} = \frac{1}{2} \begin{pmatrix} 1/\alpha[c] & -1/\alpha[c] \\ 1/\beta[c] & 1/\beta[c] \end{pmatrix}, \quad (\text{B.11})$$

yields eventually the expressions which are given in the main text [c.f. Eqs. (3.12)].

B.4 Drift-diffusion approximation in 2D

The extension of the drift-diffusion approximation to two (or higher) spatial dimensions is straightforward on the basis of the previously described derivation of effective Langevin equations in one dimension. The conceptual basis is unchanged: at first, a closed expression for the probability densities $P_i(\mathbf{r}, t)$ to find a robot at a certain position \mathbf{r} at time t is derived by adiabatic elimination of fast order parameters and, in a second step, this set of equations is reduced to the total density assuming local equilibrium. There are two technical complications which need particular attention. In dimensions larger than one, there are two vector spaces that need to be distinguished: the physical space which robots move in as well as the space of internal states. As before, we use Latin indices to label internal states (\mathcal{P}_i) and, from now on, vectorial notation is used to indicate contractions with respect to the vector space of spatial coordinates (\mathbf{r}). Further, it turns out to be crucial to identify the correct generalizations of the central quantities of interest in one dimension, namely densities $P_i(x, t)$ and differences $m_i(x, t)$, for the two-dimensional situation.

Starting point of the derivation is the Master equation [cf. Eq. (3.21)] for the probability densities $\mathcal{P}_i(\mathbf{r}, \varphi, t)$ to find a robot in state i at position \mathbf{r} moving into the direction φ at time t . In general, the dynamics is of the form

$$\begin{aligned} \partial_t \mathcal{P}_i(\mathbf{r}, \varphi, t) = & -v_0 \hat{\mathbf{s}}[\varphi] \cdot \nabla \mathcal{P}_i + D_r \partial_\varphi^2 \mathcal{P}_i + D_0 \Delta \mathcal{P}_i \\ & - \bar{\gamma}_i[c] \mathcal{P}_i + \sum_j \sum_{k=1}^{n_c} \gamma_{ij}^{(k)}[c] \int_{-\pi}^{\pi} d\varphi' g_{ij}^{(k)}(\varphi - \varphi') \mathcal{P}_j(\mathbf{r}, \varphi', t). \end{aligned} \quad (\text{B.12})$$

The terms in the first line describe the motility of robots: active motion along the director $\hat{\mathbf{s}}[\varphi(t)] = (\cos \varphi, \sin \varphi)$, rotational diffusion due to spatial heterogeneities or fluctuations of the active force [48–51] giving rise to a diffusion term with respect to the

polar angle φ , and isotropic diffusion. Stochastic transitions from one internal state to another are accounted for by the second line. The total rate at which the state i is left is determined by the rate

$$\bar{\gamma}_i[c] = \sum_j \sum_{k=1}^{n_c} \gamma_{ji}^{(k)}[c]. \quad (\text{B.13})$$

The transition rates $\gamma_{ij}^{(k)}$ denote the probability per unit time for a transition from j to state i via the k -th channel (number of channels: n_c). The γ -matrices are the immediate mathematical representation of the NCS motif under consideration. In the case of NCS motif 1, that was used as an example before, there is only one channel for each transition such that the γ -matrix reads

$$\gamma^{(1)} = \begin{pmatrix} 0 & \beta[c] \\ \alpha[c] & 0 \end{pmatrix}. \quad (\text{B.14})$$

For NCS motif 2, in contrast, two γ -matrices have to be introduced since there are two potential transitions from state 2 to state 1, cf. Fig. 3.1, one of which is accompanied by a reorientation whereas the other one is not:

$$\gamma^{(1)} = \begin{pmatrix} 0 & \gamma[c] \\ \alpha[c] & 0 \end{pmatrix}, \quad \gamma^{(2)} = \begin{pmatrix} 0 & \beta[c] \\ 0 & 0 \end{pmatrix}. \quad (\text{B.15})$$

Reorientations in space upon transitions are accounted for by the probability distributions $g_{ij}^{(k)}(\varphi)$.

Now, drift and diffusion properties of MR in two dimensions are derived along the line of arguments which was introduced in the previous paragraph for the one-dimensional case.

By integration of Eq. (B.12) over all angles φ , we obtain the dynamics of the probability densities $P_i(\mathbf{r}, t)$ to find a robot at position \mathbf{r} at time t , independent of its direction of motion:

$$\partial_t P_i(\mathbf{r}, t) = -v_0 \nabla \cdot \mathbf{m}_i + D_0 \Delta P_i - \mathcal{Q}_{ij}[c] \cdot P_j. \quad (\text{B.16})$$

This equation is structurally equivalent to Eq. (B.1a) in one dimension. The elements of the \mathcal{Q} -matrix read in general

$$\mathcal{Q}_{ij} = - \sum_{k=1}^{n_c} \left[\gamma_{ij}^{(k)} - \delta_{ij} \sum_l \gamma_{lj}^{(k)} \right]. \quad (\text{B.17})$$

One may check easily that this definition of \mathcal{Q} yields consistently the known expression for NCS motif 1 [Eq. (B.2)], for example, if the corresponding γ -matrix [Eq. (B.14)] is inserted. Naturally, those local terms in Eq. (B.16) corresponding to the internal robot dynamics remain unchanged since they are independent of the spatial dimension. Consistently, only the terms related to transport in space are altered in two dimensions as compared to the 1D scenario.

Replacing the density differences m_i between left- and right-moving robots in state i , used to analyze the 1D scenario and determining density transport, in two dimensions we make use of the *local order parameter*

$$\mathbf{m}_i(\mathbf{r}, t) = \int d\varphi \hat{\mathbf{s}}[\varphi] \mathcal{P}_i(\mathbf{r}, \varphi, t) = \int d\varphi \begin{pmatrix} \cos \varphi \\ \sin \varphi \end{pmatrix} \mathcal{P}_i(\mathbf{r}, \varphi, t), \quad (\text{B.18})$$

which appears in Eq. (B.16) and that when multiplied by v_0 provides the flux due to active self-propulsion. It is, further, the first Fourier mode of the probability distribution function $\mathcal{P}_i(\mathbf{r}, \varphi, t)$. In general, the dynamics of the fields $\mathbf{m}_i(\mathbf{r}, t)$ is coupled to higher order Fourier modes of the probability densities $\mathcal{P}_i(\mathbf{r}, \varphi, t)$ giving rise to an infinite hierarchy. However, we can make use of the fact that the dynamics of higher order Fourier modes is fast, i.e., their dynamics is slaved [70] to the density in the long time limit thus allowing for their adiabatic elimination². Similar arguments as in the one-dimensional case apply: since we aim at a reduction of the dynamics to a drift-diffusion equation, it is sufficient to calculate the dynamics of the mean local orientations $\mathbf{m}_i(\mathbf{r}, t)$ to first order in density gradients. Accordingly, we derive the following dynamics of $\mathbf{m}_i(\mathbf{r}, t)$ by multiplication of the full Master equation with $\hat{\mathbf{s}}[\varphi]$ and subsequent integration over the polar angle φ :

$$\partial_t \mathbf{m}_i(\mathbf{r}, t) \simeq -\frac{v_0}{2} \nabla P_i + D_0 \Delta \mathbf{m}_i - \mathcal{M}_{ij}[c] \mathbf{m}_j. \quad (\text{B.19})$$

This is a straightforward generalization of Eq. (B.1b). In two dimensions, the matrix elements of the local dynamics read

$$\mathcal{M}_{ij} = D_r \delta_{ij} - \sum_{k=1}^{n_c} \left[\gamma_{ij}^{(k)} \langle \cos \varphi \rangle_{ij}^{(k)} - \delta_{ij} \sum_l \gamma_{lj}^{(k)} \right]. \quad (\text{B.20})$$

In two dimensions, they depend on the mean cosine of the reorientation distributions³

$$\langle \cos \varphi \rangle_{ij}^{(k)} = \int_{-\pi}^{\pi} d\varphi \cos \varphi g_{ij}^{(k)}(\varphi). \quad (\text{B.21})$$

In the case of reversal for NCS motif 1, $g_{12}^{(1)}(\varphi) = \delta(\varphi - \pi)$ is the only nontrivial element. It implies $\langle \cos \varphi \rangle_{12}^{(1)} = -1$. In combination with the corresponding γ -matrix [Eq. (B.14)], the matrix $\mathcal{M}[c]$ reduces again exactly to the familiar one-dimensional result, cf. Eq. (B.2).

The reduction of Eqs. (B.16) and (B.19) onto the density follows the procedure which was outline in the previous paragraph for one spatial dimension. Adiabatic elimination ($\partial_t \mathbf{m}_i \approx 0$) of the fields \mathbf{m}_i yields

$$\mathbf{m}_i \approx -\frac{v_0}{2} \{ \mathcal{M}^{-1} \}_{ij} \nabla P_j \quad (\text{B.22})$$

to lowest order in density gradients [cf. Eq. (B.6)] and, thus, one obtains the following reduced density dynamics via insertion into Eq. (B.16):

$$\partial_t P_i(\mathbf{r}, t) \simeq \nabla \cdot \left[\left(\frac{v_0^2}{2} \{ \mathcal{M}^{-1} \}_{ij} + D_0 \delta_{ij} \right) \nabla P_j \right] - \mathcal{Q}_{ij}[c] P_j. \quad (\text{B.23})$$

This is the 2D-analogue to Eq. (B.7). In the diffusive limit, the fields P_i have to lie in the kernel of the matrix $\mathcal{Q}[c]$, i.e. $\mathcal{Q}_{ij}[c] P_j = 0$. We normalize such that $P_i(x, t) = P(x, t) V_i[c]$ implying $\sum_i V_i[c] = 1$ and $\mathcal{Q}_{ij}[c] V_j = 0$. Inserting this ansatz into Eq. (B.23) yields the preliminary Fokker-Planck equation

$$\partial_t P(\mathbf{r}, t) \simeq \sum_i \nabla \cdot \left\{ \left(\frac{v_0^2}{2} \{ \mathcal{M}^{-1} \}_{ij} + D_0 \delta_{ij} \right) \nabla [P V_j[c]] \right\}. \quad (\text{B.24})$$

²For a detailed account on mode reduction in several active motion models, see [71–73].

³It was silently assumed that the reorientation distributions $g_{ij}^{(k)}(\varphi)$ are symmetric: $g_{ij}^{(k)}(-\varphi) = g_{ij}^{(k)}(\varphi)$.

We define the force $\mathbf{f}(\mathbf{r})$ and the position-dependent diffusion $D(\mathbf{r})$ analogous to the one-dimensional case [Eq. (B.11)]:

$$\partial_t P(\mathbf{r}, t) = -\nabla \cdot [\mathbf{f}(\mathbf{r})P(\mathbf{r}, t)] + \Delta [D(\mathbf{r})P(\mathbf{r}, t)]. \quad (\text{B.25})$$

The comparison to Eq. (B.24) eventually yields the final expressions for the drift and local diffusion coefficient:

$$\mathbf{f}(\mathbf{r}) = \frac{v_0^2}{2} \sum_{i,j} \left(\nabla \{ \mathcal{M}^{-1} \}_{ij} \right) V_j[c], \quad (\text{B.26a})$$

$$D(\mathbf{r}) = D_0 + \frac{v_0^2}{2} \sum_{i,j} \{ \mathcal{M}^{-1} \}_{ij} V_j[c]. \quad (\text{B.26b})$$

B.5 Drift-diffusion approximation in 3D

In this section, we briefly summarize some technical particularities of the drift-diffusion approximation in three dimensions. The general discussion follows closely the procedure outlined in Appendix B.4. Starting point is the general Master equation

$$\begin{aligned} \partial_t \mathcal{P}_i(\mathbf{r}, \hat{\mathbf{s}}, t) &= -v_0 \hat{\mathbf{s}} \cdot \nabla \mathcal{P}_i + D_r \mathcal{L}[\mathcal{P}_i] + D_0 \Delta \mathcal{P}_i \\ &- \bar{\gamma}_i[c] \mathcal{P}_i + \sum_j \sum_{k=1}^{n_c} \gamma_{ij}^{(k)}[c] \int d^3s g_{ij}^{(k)}(\hat{\mathbf{s}}|\hat{\mathbf{s}}') \mathcal{P}_j(\mathbf{r}, \hat{\mathbf{s}}', t). \end{aligned} \quad (\text{B.27})$$

The transition rates $\gamma_{ij}^{(k)}[c]$ denote, as before, the probability per unit time for a transition from state j to state i via the k -th channel. Such transitions may be accompanied by a transition from an orientation $\hat{\mathbf{s}}'$ to $\hat{\mathbf{s}}$ which is accounted for by the transition probability density $g_{ij}^{(k)}(\hat{\mathbf{s}}|\hat{\mathbf{s}}')$. The continuous, stochastic rotational dynamics of the director $\hat{\mathbf{s}}$ in three dimensions is accounted for by the operator

$$\mathcal{L}[\mathcal{P}_i] = \partial_{s_\mu} [2s_\mu \mathcal{P}_i] + \partial_{s_\mu} \partial_{s_\nu} [(\delta_{\mu\nu} - s_\mu s_\nu) \mathcal{P}_i], \quad (\text{B.28})$$

where a sum over μ and ν is implicit. This Cartesian representation of the director dynamics is simpler to handle in terms of analytical calculations as compared to a parametrization in terms of spherical coordinates (cf. Eq. (3.30) and Refs. [52, 64]).

We point out that there are two vector spaces which have to be distinguished in the following: the physical space which robots move in (three dimensional) and the space of internal states. To avoid confusion, the components of the former are denoted by Greek indices, whereas the latter are indicated by Latin indices.

The derivation of the drift-diffusion approximation starts from the temporal evolution of the densities

$$P_i(\mathbf{r}, t) = \int d^3s \mathcal{P}_i(\mathbf{r}, \hat{\mathbf{s}}, t), \quad (\text{B.29})$$

which is obtained from the Master equation (B.27) by integration over all orientations of the director yielding

$$\partial_t P_i(\mathbf{r}, t) = -v_0 \nabla \cdot \mathbf{m}_i + D_0 \Delta P_i - \mathcal{Q}_{ij}[c] \cdot P_j. \quad (\text{B.30})$$

Just as in two dimensions, the matrix elements of the matrix \mathcal{Q} are determined by

$$\mathcal{Q}_{ij} = - \sum_{k=1}^{n_c} \left[\gamma_{ij}^{(k)} - \delta_{ij} \sum_l \gamma_{lj}^{(k)} \right]. \quad (\text{B.31})$$

We keep in mind that we will assume local equilibrium throughout, i.e. the probability to find a robot in a certain internal state is determined by $P_i(\mathbf{r}, t) = V_i[c]P(\mathbf{r}, t)$ such that $\mathcal{Q}_{ij}V_j = 0$ and $\sum_i V_i = 1$.

In three dimensions, the flux is determined by the local order parameter

$$\mathbf{m}_i(\mathbf{r}, t) = \int d^3s \hat{\mathbf{s}} \mathcal{P}_i(\mathbf{r}, \hat{\mathbf{s}}, t). \quad (\text{B.32})$$

The dynamics of \mathbf{m}_i is, in turn, obtained by multiplication of the Master equation (B.27) by $\hat{\mathbf{s}}$ and subsequent integration:

$$\partial_t \mathbf{m}_i(\mathbf{r}, t) = -v_0 \nabla \cdot \mathcal{T}_i + D_0 \Delta \mathbf{m}_i - \mathcal{M}_{ij}[c] \mathbf{m}_j. \quad (\text{B.33})$$

The matrix elements

$$\mathcal{M}_{ij} = 2D_r \delta_{ij} - \sum_{k=1}^{n_c} \left[\gamma_{ij}^{(k)} \langle \cos \psi \rangle_{ij}^{(k)} - \delta_{ij} \sum_l \gamma_{lj}^{(k)} \right] \quad (\text{B.34})$$

differ from their two-dimensional counterpart [cf. Eq. (B.20)] by just a factor of two in front of the angular noise intensity. The relevant parameter which accounts for the reorientation is the mean cosine of the angle between the directors just right before and after a reorientation, defined by

$$\langle \cos \psi \rangle_{ij}^{(k)} = \int d^3s \hat{\mathbf{s}} \cdot \hat{\mathbf{s}}' g_{ij}^{(k)}(\hat{\mathbf{s}}|\hat{\mathbf{s}}'). \quad (\text{B.35})$$

Due to the Cartesian parametrization of the director dynamics, a new term involving the symmetric tensor

$$\{\mathcal{T}_i\}_{\mu\nu} = \int d^3s s_\mu s_\nu \mathcal{P}_i(\mathbf{r}, \hat{\mathbf{s}}, t) \quad (\text{B.36})$$

appears in Eq. (B.33). In order to derive an effective transport equation for the density $P(\mathbf{r}, t) = \sum_i P_i(\mathbf{r}, t)$, a closure relation for the tensors \mathcal{T}_i has to be found. Since we aim at reducing the density dynamics to a Fokker-Planck equation valid in the diffusive limit, it is possible to neglect spatial derivatives in the dynamics of \mathcal{T}_i to lowest order:

$$\partial_t \{\mathcal{T}_i\}_{\mu\nu} \approx \delta_{\mu\nu} \Omega_{ij} P_j - \{\Xi_{ij} \mathcal{T}_j\}_{\mu\nu}. \quad (\text{B.37})$$

This equation involves the matrices

$$\Omega_{ij} = 2D_r \delta_{ij} + \sum_{k=1}^{n_c} \gamma_{ij}^{(k)} [c] \cdot \frac{1 - \langle \cos^2 \psi \rangle_{ij}^{(k)}}{2} \quad (\text{B.38})$$

and

$$\Xi_{ij} = \left(6D_r + \bar{\gamma}_i[c]\right) \delta_{ij} - \sum_{k=1}^{n_c} \left[\gamma_{ij}^{(k)}[c] \cdot \frac{3\langle \cos^2 \psi \rangle_{ij}^{(k)} - 1}{2} \right]. \quad (\text{B.39})$$

The tensor \mathcal{T}_i may be expressed as a function of the densities $P_i(\mathbf{r}, t)$ via adiabatic elimination, $\partial_t \{\mathcal{T}_i\}_{\mu\nu} \approx 0$. In the state of local equilibrium, where $P_i = V_i P$ and $\mathcal{Q}_{ij} V_j = 0$, the rather complicated expressions above take a rather simple form, as can be verified via direct calculation:

$$\{\mathcal{T}_i\}_{\mu\nu} = \frac{\delta_{\mu\nu}}{3} V_i[c] P. \quad (\text{B.40})$$

Reinsertion of this solution into the dynamics of \mathbf{m}_i [Eq. (B.33)] yields the familiar equation

$$\partial_t \mathbf{m}_i(\mathbf{r}, t) \simeq -\frac{v_0}{3} \nabla P_i + D_0 \Delta \mathbf{m}_i - \mathcal{M}_{ij}[c] \mathbf{m}_j \quad (\text{B.41})$$

which is structurally identical to Eqs. (B.1b), (B.19). Only the speed has been rescaled by the spatial dimensionality.

The remaining part of the calculation follows therefore exactly the same steps as in two spatial dimensions. Accordingly, the drift and diffusion for MR in three spatial dimensions are determined by

$$\mathbf{f}(\mathbf{r}) = \frac{v_0^2}{3} \sum_{i,j} \left(\nabla \{\mathcal{M}^{-1}\}_{ij} \right) V_j[c], \quad (\text{B.42a})$$

$$D(\mathbf{r}) = D_0 + \frac{v_0^2}{3} \sum_{i,j} \{\mathcal{M}^{-1}\}_{ij} V_j[c]. \quad (\text{B.42b})$$

Note, however, that the definition of the matrix \mathcal{M} is slightly different in two and three dimensions as the rotational noise amplitude D_r is proportional to the factor $d-1$, where d is the actual spatial dimensions.

Appendix C

Intermittent Collective Behavior

C.1 Parameter diagrams using different parameter values

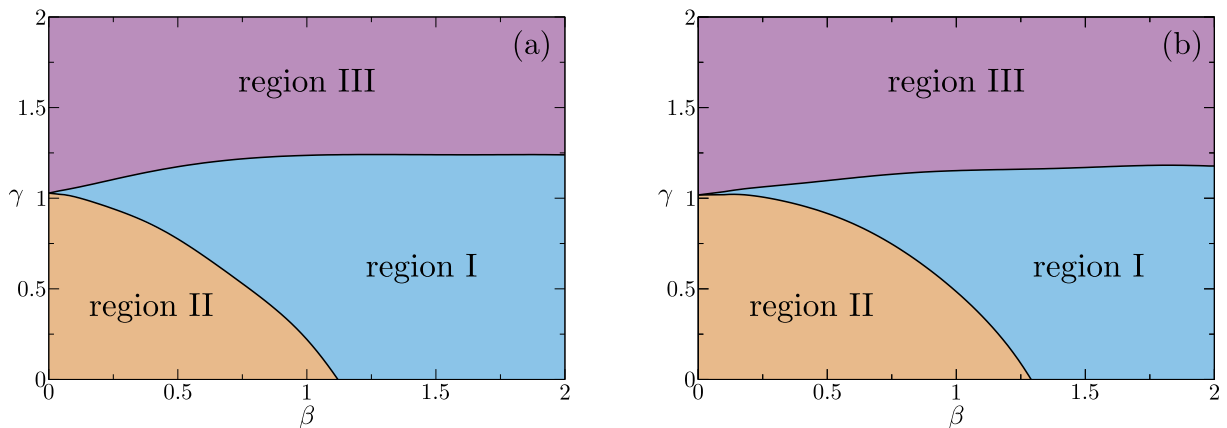


Figure C.1 – Parameter diagrams for different values of ω . In (a), we use $\omega = 2$ and in (b) we use $\omega = 10$. For both cases, the system size is $N = 50$. We notice that the regions I, II and III are slightly modified but the diagrams as a whole stay qualitatively equal to the one presented in Figure 4.7 in Chapter 4 in the main text.

C.2 General solution of the period distribution $P(T)$ for the CCA.

In this Appendix, we detail the method to obtain the solution of the distribution of the periods in the CCA. We omit the labels for the CCA variables since all the variables in this section correspond to variables of the **Collective Clock**. As said in Chapter 5, the problem is reduced to solve the following system of equations:

$$\begin{aligned} \partial_t P_1(t) &= -R_1 P_1(t), \\ \partial_t P_i(t) &= -R_i P_i(t) + R_{i-1} P_{i-1}(t) \quad \text{for } 2 \leq i \leq 3N. \end{aligned} \tag{C.1}$$

In the system of equations (C.1) we denote by $P_i(t)$ the probability of finding the system in tick i in the collective clock at time t having started at time $t = 0$ in the tick 1. This

means that the initial conditions for each $P_i(t)$ are:

$$\begin{aligned} P_1(t=0) &= 1, \\ P_i(t=0) &= 0 \end{aligned} \quad \text{for } 2 \leq i \leq 3N. \quad (\text{C.2})$$

To solve the system of equations, we use the Laplace transform, defined as

$$\mathcal{L}\left\{f(t)\right\} = \hat{f}(s) = \int_0^{\infty} dt f(t) e^{-st}, \quad (\text{C.3})$$

and two key properties, the first one being the transform of the convolution:

$$\mathcal{L}\left\{(f * g)(t)\right\} = \mathcal{L}\left\{\int_0^t f(t_1) g(t - t_1) dt_1\right\} = \hat{f}(s) \hat{g}(s), \quad (\text{C.4})$$

and the second one being:

$$\mathcal{L}\left\{t^n e^{-\alpha t}\right\} = \frac{n!}{(s + \alpha)^{n+1}}. \quad (\text{C.5})$$

We recast the system (C.1) as follows:

$$\begin{aligned} s \hat{P}_1(s) &= -R_1 \hat{P}_1(s) + 1, \\ s \hat{P}_i(s) &= -R_i \hat{P}_i(s) + R_{i-1} \hat{P}_{i-1}(s) \end{aligned} \quad \text{for } 2 \leq i \leq 3N. \quad (\text{C.6})$$

For the calculation of the distribution of periods we need to calculate $P(T = t) = R_{3N} P_{3N}(t)$ and for this, we use the system of equations (C.6) to express the Laplace transform of the solution we need in terms of multiplications of the transition rates of the collective clock as follows:

$$\hat{P}(S = s) = R_{3N} \hat{P}_{3N}(s) = \prod_{j=1}^{3N} \left(\frac{R_j}{s + R_j} \right). \quad (\text{C.7})$$

We can obtain the inverse Laplace transform and get the general solution we are looking for:

$$P(T = t) = \left(\prod_{i=1}^{3N} R_i \right) \int_0^t dt_1 \int_0^{t-t_1} dt_2 \int_0^{t-t_1-t_2} dt_3 \cdots \int_0^{t-t_1-t_2-\cdots-t_{3N-2}} dt_{3N-1} \exp \left[-\sum_{j=1}^{3N-1} R_j t_j - R_{3N} (t - \tau_{3N-1}) \right], \quad (\text{C.8})$$

where we make use of the auxiliary variable

$$\tau_j = \sum_{k=1}^j t_k. \quad (\text{C.9})$$

C.2.1 Case with different rates ($R_i \neq R_j, \forall i \neq j$).

The general solution (C.8) can be given explicitly in the case where all rates of the collective clock do not repeat, i.e: $R_i \neq R_j, \forall i \neq j$. In this case, the solution is given by:

$$P(T = t) = \left(\prod_{i=1}^{3N} R_i \right) \sum_{j=1}^{3N} \lambda_{3N,j} e^{-R_j t}, \quad (\text{C.10})$$

where $\lambda_{1,1} = 1$ and the coefficients $\lambda_{i,j}$ in general can be obtained recursively as follows:

$$\lambda_{i,j} = \begin{cases} \frac{\lambda_{i-1,j}}{R_i - R_j} & \text{if } i < j, \\ -\sum_{j=1}^{i-1} \lambda_{i,j} & \text{if } i = j, \\ 0 & \text{if } i > j. \end{cases} \quad (\text{C.11})$$

C.2.2 Case with repeating rates.

In the specific case of the main text, the collective clock is particularly simple because there are some rates that appear multiple times. More precisely, we have that

$$R_i = R_{N+i} = R_{2N+i} \quad \forall i : 1 \leq i \leq N. \quad (\text{C.12})$$

Performing a similar analysis as the previous case, we can express the solution in the Laplace space as:

$$\hat{P}(S = s) = R_{3N} \hat{P}_{3N}(s) = \prod_{j=1}^N \left(\frac{R_j}{s + R_j} \right)^3. \quad (\text{C.13})$$

The solution is obtained using (C.4) and (C.5) and is, in this case, ironically more complicated:

$$P(T = t) = \frac{\prod_{i=1}^N R_i^3}{2^N} \int_0^t dt_1 \int_0^{t-\tau_1} dt_2 \cdots \int_0^{t-\tau_{N-2}} dt_{N-1} \left(\prod_{j=1}^{N-1} t_j^2 \right) \left(t - \tau_{N-1} \right)^2 \exp \left[-\sum_{j=1}^{N-1} R_j t_j - R_N \left(t - \tau_{N-1} \right) \right], \quad (\text{C.14})$$

where we used again the auxiliary variable of equation (C.9).

Appendix D

Collective transport properties of a group of N independent particles with internal clock

In this appendix, we address the situation where we have N independent particles that have internal dynamics between states. This is a limit situation when we introduce a radius of interaction between particles to the model studied in Chapter 5. It is in fact the situation when the radius of interaction is so small that the group loses coherence. First, we solve the transport properties of one single particle and then we use the obtained results to calculate the collective transport properties of the group.

D.0.1 Transport properties of a single particle with internal clock.

Since there is only one particle, the rates of transition between the states are

$$R_{i \rightarrow j} = \omega \tag{D.1}$$

for all three transitions. The equation of motion of the particle in 1D is given by the internal variable $q(t)$ and is given by:

$$\dot{x}(t) = v_0 s(t) + \sqrt{2D_0} \xi(t) \quad \text{if } q(t) = A \text{ or } C, \tag{D.2}$$

$$\dot{x}(t) = \sqrt{2D_0} \xi(t) \quad \text{if } q(t) = B, \tag{D.3}$$

with the dynamics of $s(t)$ as explained in the main text. The average period is in this case $\langle T \rangle = \frac{1}{\omega} + \frac{1}{\omega} + \frac{1}{\omega} = \frac{3}{\omega}$, and we can also estimate the average velocity per period, namely $\bar{v} = \frac{v_0}{3}$. We can use an effective langevin equation using these estimates:

$$\dot{x}(t) = \bar{v} s(t) + \sqrt{2D_0} \xi(t), \tag{D.4}$$

where we suppose that $s(t)$ changes direction after $\langle T \rangle$. Knowing that

$$x(t) = \int_0^t dt' \left[\bar{v} s(t') + \sqrt{2D_0} \xi(t') \right], \tag{D.5}$$

we can calculate the average mean squared displacement of the particle position as follows:

$$\langle x^2(t) \rangle = \int_0^t dt' \int_0^t dt'' \left\langle \left[\bar{v} s(t') + \sqrt{2D_0} \xi(t') \right] \left[\bar{v} s(t'') + \sqrt{2D_0} \xi(t'') \right] \right\rangle. \quad (\text{D.6})$$

Knowing that the stochastic variables $s(t)$ and $\xi(t)$ are independent, we arrive to the result:

$$\langle x^2(t) \rangle = \left(\bar{v}^2 \int_0^t dt' \int_0^t dt'' \langle s(t') s(t'') \rangle \right) + \left(2D_0 \int_0^t dt' \int_0^t dt'' \langle \xi(t') \xi(t'') \rangle \right). \quad (\text{D.7})$$

For long times, we get:

$$\lim_{t \rightarrow \infty} \langle x^2(t) \rangle = 2 \left(\frac{3\bar{v}^2}{\omega} \right) t + 2D_0 t = 2D_{\text{clock}} t + 2D_{\text{noise}} t = 2D_{\text{eff}} t, \quad (\text{D.8})$$

with the effective diffusion coefficient being

$$D_{\text{eff}} = \frac{3\bar{v}^2}{\omega} + D_0. \quad (\text{D.9})$$

D.0.2 Transport properties of N independent particles with internal clock.

In this case, we have N particles, each one with the equation of motion in 1D:

$$\dot{x}_i(t) = v_0 s_i(t) + \sqrt{2D_0} \xi_i(t) \quad \text{if } q_i(t) = A \text{ or } C, \quad (\text{D.10})$$

$$\dot{x}_i(t) = \sqrt{2D_0} \xi_i(t) \quad \text{if } q_i(t) = B, \quad (\text{D.11})$$

with the dynamics of $s_i(t)$ as explained in the main text. The center of mass is calculated as follows:

$$x_{cm}(t) = \frac{1}{N} \sum_{i=1}^N x_i(t) = \frac{1}{N} \sum_{i=0}^N \int_0^t dt' \dot{x}_i(t'). \quad (\text{D.12})$$

So, the general expression of the average mean squared displacement of the center of mass is:

$$\langle x_{cm}^2(t) \rangle = \frac{1}{N^2} \sum_{i=1}^N \sum_{j=1}^N \int_0^t dt' \int_0^t dt'' \left\langle \left[\bar{v} s_i(t') + \sqrt{2D_0} \xi(t') \right] \left[\bar{v} s_j(t'') + \sqrt{2D_0} \xi(t'') \right] \right\rangle. \quad (\text{D.13})$$

Using again the fact that the stochastic variables of the direction of motion and the noise are independent, we can recast equation (D.13) as:

$$\begin{aligned}
\langle x_{cm}(t) \rangle &= \frac{1}{N^2} \sum_{i=1}^N \sum_{j=1}^N \int_0^t dt' \int_0^t dt'' \left[\bar{v}^2 \langle s_i(t') s_j(t'') \rangle + 2D_0 \langle \xi_i(t') \xi_j(t'') \rangle \right] \\
&= \frac{1}{N^2} \sum_{i=1}^N \int_0^t dt' \int_0^t dt'' \left[\bar{v}^2 \langle s_i(t') s_i(t'') \rangle + 2D_0 \langle \xi_i(t') \xi_i(t'') \rangle \right] \\
\Rightarrow \lim_{t \rightarrow \infty} \langle x_{cm}(t) \rangle &= 2 \left(\frac{3\bar{v}^2}{N\omega} \right) t + 2 \left(\frac{D_0}{N} \right) t = 2 \left(\frac{D_{\text{eff}}}{N} \right) t.
\end{aligned} \tag{D.14}$$

The second quantity that we want to study is the average dispersion of particles around the center of mass, defined as:

$$\sigma_g^2(t) = \frac{1}{N} \sum_{i=1}^N \left(x_i(t) - x_{cm}(t) \right)^2. \tag{D.15}$$

The average in the long time limits is then:

$$\begin{aligned}
\langle \sigma_g^2(t) \rangle &= \frac{1}{N} \left\langle \sum_{i=1}^N \left(x_i^2(t) - 2x_i(t) x_{cm}(t) + x_{cm}^2(t) \right) \right\rangle \\
&= \frac{1}{N} \left\langle \sum_{i=1}^N x_i^2(t) \right\rangle - \langle x_{cm}^2(t) \rangle.
\end{aligned} \tag{D.16}$$

Thus, the final result in the long-time behavior is:

$$\lim_{t \rightarrow \infty} \langle \sigma_g^2(t) \rangle = \left(1 - \frac{1}{N} \right) 2 D_{\text{eff}} t, \tag{D.17}$$

with the same effective diffusion coefficient given in (D.9).

Bibliography

- [1] S. Toulet, J. Gautrais, R. Bon, and F. Peruani, “Imitation combined with a characteristic stimulus duration results in robust collective decision-making,” *PLoS ONE*, vol. 10, p. e0140188, 10 2015.
- [2] C. S. Harwood, K. Fosnaugh, and M. Dispensa, “Flagellation of *pseudomonas putida* and analysis of its motile behavior,” *Journal of Bacteriology.*, vol. 171, no. 7, pp. 4063–4066, 1989.
- [3] O. Pohl, M. Hintsche, Z. Alirezaeizanjani, M. Seyrich, C. Beta, and H. Stark, “Inferring the chemotactic strategy of *p. putida* and *e. coli* using modified kramers-moyal coefficients,” *PLoS Comput. Biol.*, vol. 13, no. 1, p. e1005329, 2017.
- [4] M. Theves, J. Taktikos, V. Zaburdaev, H. Stark, and C. Beta, “Random walk patterns of a soil bacterium in open and confined environments,” *Europhys. Lett.*, vol. 109, no. 2, p. 28007, 2015.
- [5] H. C. Berg and D. A. Brown, “Chemotaxis in *escherichia coli* analysed by three-dimensional tracking,” *Nature*, vol. 239, no. 5374, pp. 500–504, 1972.
- [6] T. Nutsch, W. Marwan, D. Oesterhelt, and E. D. Gilles, “Signal processing and flagellar motor switching during phototaxis of *halobacterium salinarum.*,” *Genome Research*, vol. 13 11, pp. 2406–12, 2003.
- [7] E. P. Ipiña, S. Otte, R. Pontier-Bres, D. Czerucka, and F. Peruani, “Enterohemorrhagic *escherichia coli* stops to diffuse faster near surfaces,” *Submitted in Nature Physics*, 2017.
- [8] M. Hintsche, V. Waljor, R. Großmann, M. J. Kühn, K. M. Thormann, F. Peruani, and C. Beta, “A polar bundle of flagella can drive bacterial swimming by pushing, pulling, or coiling around the cell body,” *Scientific Reports*, vol. 7, 2017.
- [9] H. C. Berg, *E. coli in Motion*. Springer Science & Business Media, 2008.
- [10] E. Korobkova, T. Emone, J. M. Vilar, T. S. Shimizu, and P. Cluzel, “From molecular noise to behavioural variability in a single bacterium,” *Nature*, vol. 428, pp. 574–578, 2004.
- [11] Y. Tu and G. Grinstein, “How white noise generates power-law switching in bacterial flagellar motors,” *Phys. Rev. Lett.*, vol. 94, p. 208101, May 2005.

- [12] M. J. Tindall, E. A. Gaffney, P. K. Maini, and J. P. Armitage, “Theoretical insights into bacterial chemotaxis,” *WIREs Syst. Biol. Med.*, vol. 4, no. 3, pp. 247–259, 2012.
- [13] A. Celani and M. Vergassola, “Bacterial strategies for chemotaxis response,” *Proc. Natl. Acad. Sci. USA*, vol. 107, no. 4, pp. 1391–1396, 2010.
- [14] M. J. Schnitzer, “Theory of continuum random walks and application to chemotaxis,” *Phys. Rev. E*, vol. 48, pp. 2553–2568, 1993.
- [15] M. Cates, “Diffusive transport without detailed balance in motile bacteria: does microbiology need statistical physics?,” *Rep. Prog. Phys.*, vol. 75, no. 4, p. 042601, 2012.
- [16] M. Flores, T. S. Shimizu, P. R. ten Wolde, and F. Tostevin, “Signaling noise enhances chemotactic drift of *E. coli*,” *Phys. Rev. Lett.*, vol. 109, p. 148101, 2012.
- [17] Y. Wu, A. D. Kaiser, Y. Jiang, and M. S. Alber, “Periodic reversal of direction allows myxobacteria to swarm,” *Proc. Natl. Acad. Sci. USA*, vol. 106, no. 4, pp. 1222–1227, 2009.
- [18] A. Be’er, S. K. Strain, R. A. Hernández, E. Ben-Jacob, and E.-L. Florin, “Periodic reversals in *paenibacillus dendritiformis* swarming,” *J. Bacteriol.*, vol. 195, no. 12, pp. 2709–2717, 2013.
- [19] J. K. Parrish and L. Edelstein-Keshet, “Complexity, pattern, and evolutionary trade-offs in animal aggregation,” *Science*, vol. 284, no. 5411, pp. 99–101, 1999.
- [20] M. Ballerini, N. Cabibbo, R. Candelier, A. Cavagna, E. Cisbani, I. Giardina, V. Lecomte, A. Orlandi, G. Parisi, A. Procaccini, M. Viale, and V. Zdravkovic, “Interaction ruling animal collective behavior depends on topological rather than metric distance: Evidence from a field study,” *Proceedings of the National Academy of Sciences*, vol. 105, pp. 1232–1237, Jan. 2008.
- [21] L. G. Nava, R. Bon, and F. Peruani, “Intermittent collective behavior in small groups of gregarious animals,” *available upon request*, 2018.
- [22] W. Bialek, A. Cavagna, I. Giardina, T. Mora, O. Pohl, E. Silvestri, M. Viale, and A. M. Walczak, “Social interactions dominate speed control in poising natural flocks near criticality,” *Proceedings of the National Academy of Sciences*, vol. 111, no. 20, pp. 7212–7217, 2014.
- [23] A. Cavagna, S. Melillo, L. Parisi, and F. Ricci-Tersenghi, “Sparta - tracking across occlusions via global partitioning of 3d clouds of points,” *CoRR*, vol. abs/1802.05878, 2018.
- [24] H. J. Mönck, A. Jörg, T. von Falkenhausen, J. Tanke, B. Wild, D. Dormagen, J. Piotrowski, C. Winklmayr, D. Bierbach, and T. Landgraf, “Biotracker: An open-source computer vision framework for visual animal tracking,” *CoRR*, vol. abs/1803.07985, 2018.

- [25] F. Ginelli, F. Peruani, M.-H. Pillot, H. Chaté, G. Theraulaz, and R. Bon, “Intermittent collective dynamics emerge from conflicting imperatives in sheep herds,” *Proc. Natl. Acad. Sci.*, vol. 112, no. 41, pp. 12729–12734, 2015.
- [26] L. G. Nava, R. Großmann, and F. Peruani, “Markovian robots: Minimal navigation strategies for active particles,” *Phys. Rev. E*, vol. 97, p. 042604, Apr 2018.
- [27] R. P. Feynman, “There’s plenty of room at the bottom,” *Engineering and Science*, vol. 23, no. 5, pp. 22–36, 1960.
- [28] H. Bayley and P. S. Cremer, “Stochastic sensors inspired by biology,” *Nature*, vol. 413, pp. 226–230, 2001.
- [29] H. Hess and J. L. Ross, “Non-equilibrium assembly of microtubules: from molecules to autonomous chemical robots,” *Chem. Soc. Rev.*, vol. 46, pp. 5570–5587, 2017.
- [30] S. Sanchez and M. Pumera, “Nanorobots: The ultimate wireless self-propelled sensing and actuating devices,” *Chem. – Asian J.*, vol. 4, no. 9, pp. 1402–1410, 2009.
- [31] A. A. Solovev, W. Xi, D. H. Gracias, S. M. Harazim, C. Deneke, S. Sanchez, and O. G. Schmidt, “Self-propelled nanotools,” *ACS Nano*, vol. 6, no. 2, pp. 1751–1756, 2012.
- [32] T. Patino, R. Mestre, and S. Sanchez, “Miniaturized soft bio-hybrid robotics: a step forward into healthcare applications,” *Lab. Chip*, vol. 16, p. 3636, 2016.
- [33] X. Ma and S. Sanchez, “Self-propelling micro-nanorobots: challenges and future perspectives in nanomedicine,” *Nanomedicine*, vol. 12, no. 12, pp. 1363–1367, 2017.
- [34] A. Joseph, C. Contini, D. Cecchin, S. Nyberg, L. Ruiz-Perez, J. Gaitzsch, G. Fullstone, X. Tian, J. Azizi, J. Preston, G. Volpe, and G. Battaglia, “Chemotactic synthetic vesicles: Design and applications in blood-brain barrier crossing,” *Science Advances*, vol. 3, no. 8, 2017.
- [35] W. A. Churaman, L. J. Currano, C. J. Morris, J. E. Rajkowski, and S. Bergbreiter, “The first launch of an autonomous thrust-driven microrobot using nanoporous energetic silicon,” *J. Microelectromech. S.*, vol. 21, no. 1, pp. 198–205, 2012.
- [36] M. Kim, A. A. Julius, and U. K. Cheang, eds., *Microbiorobotics: Biologically Inspired Microscale Robotic Systems*. Elsevier, 2 ed., 2017.
- [37] E. M. Purcell, “Life at low reynolds number,” *Am. J. Phys.*, vol. 45, no. 1, pp. 3–11, 1977.
- [38] S. Chatterjee, R. A. da Silveira, and Y. Kafri, “Chemotaxis when bacteria remember: drift versus diffusion,” *PLoS Comput. Biol.*, vol. 7, no. 12, p. e1002283, 2011.
- [39] J. E. Segall, S. M. Block, and H. C. Berg, “Temporal comparisons in bacterial chemotaxis,” *Proc. Natl. Acad. Sci. USA*, vol. 83, no. 23, pp. 8987–8991, 1986.
- [40] P.-G. de Gennes, “Chemotaxis: the role of internal delays,” *Eur. Biophys. J.*, vol. 33, pp. 691–693, Dec 2004.

- [41] Y. Tu, “Quantitative modeling of bacterial chemotaxis: Signal amplification and accurate adaptation,” *Annual Review of Biophysics*, vol. 42, no. 8, pp. 337–359, 2013.
- [42] D. A. Clark and L. C. Grant, “The bacterial chemotactic response reflects a compromise between transient and steady-state behavior,” *Proc. Natl. Acad. Sci. USA*, vol. 102, no. 26, pp. 9150–9155, 2005.
- [43] C. Gardiner, *Stochastic Methods: A Handbook for the Natural and Social Sciences*. Springer Series in Synergetics, Springer, 2009.
- [44] N. Van Kampen, *Stochastic Processes in Physics and Chemistry*. North-Holland Personal Library, Elsevier Science, 2011.
- [45] H. Risken, *The Fokker-Planck equation: Methods of solution and applications*. Springer Verlag, 1996.
- [46] R. Großmann, F. Peruani, and M. Bär, “Diffusion properties of active particles with directional reversal,” *New J. Phys.*, vol. 18, no. 4, p. 043009, 2016.
- [47] Z. Li, Q. Cai, X. Zhang, G. Si, Q. Ouyang, C. Luo, and Y. Tu, “Barrier crossing in escherichia coli chemotaxis,” *Phys. Rev. Lett.*, vol. 118, p. 098101, 2017.
- [48] A. Mikhailov and D. Meinköhn, “Self-motion in physico-chemical systems far from thermal equilibrium,” in *Stochastic Dynamics* (L. Schimansky-Geier and T. Pöschel, eds.), vol. 484 of *Lecture Notes in Physics*, pp. 334–345, Springer Berlin Heidelberg, 1997.
- [49] F. Peruani and L. G. Morelli, “Self-propelled particles with fluctuating speed and direction of motion in two dimensions,” *Phys. Rev. Lett.*, vol. 99, p. 010602, Jul 2007.
- [50] P. Romanczuk and L. Schimansky-Geier, “Brownian motion with active fluctuations,” *Phys. Rev. Lett.*, vol. 106, p. 230601, Jun 2011.
- [51] O. Chepizhko and F. Peruani, “Diffusion, subdiffusion, and trapping of active particles in heterogeneous media,” *Phys. Rev. Lett.*, vol. 111, p. 160604, 2013.
- [52] R. Großmann, F. Peruani, and M. Bär, “A geometric approach to self-propelled motion in isotropic & anisotropic environments,” *Eur. Phys. J.: Spec. Top.*, vol. 224, no. 7, pp. 1377–1394, 2015.
- [53] M. F. Perrin, *Étude Mathématique du Mouvement Brownien de Rotation*. Gauthier-Villars et Cie. Éditeurs, 1928.
- [54] K. Yosida, “Brownian motion on the surface of the 3-sphere,” *Ann. Math. Statist.*, vol. 20, pp. 292–296, 06 1949.
- [55] N. Saitô, K. Takahashi, and Y. Yunoki, “The statistical mechanical theory of stiff chains,” *J. Phys. Soc. Jpn.*, vol. 22, no. 1, pp. 219–226, 1967.

- [56] D. R. Brillinger, “A particle migrating randomly on a sphere,” *J. Theor. Probab.*, vol. 10, pp. 429–443, Apr 1997.
- [57] B. M. Friedrich and F. Jülicher, “Steering chiral swimmers along noisy helical paths,” *Phys. Rev. Lett.*, vol. 103, p. 068102, Aug 2009.
- [58] D. Freedman, R. Pisani, and R. Purves, *Statistics*. W.W. Norton & Company, 1997.
- [59] H. Akaike, *Information Theory and an Extension of the Maximum Likelihood Principle*, pp. 199–213. New York, NY: Springer New York, 1998.
- [60] P. L. Meyer, *Introductory probability and statistical applications*. Addison Wesley, 1965.
- [61] T. Nutsch, W. Marwan, D. Oesterhelt, and E. D. Gilles, “Signal processing and flagellar motor switching during phototaxis of halobacterium salinarum,” *Genome Res.*, vol. 13, no. 11, pp. 2406–2412, 2003.
- [62] C. S. Harwood, R. E. Parales, and M. Dispensa, “Chemotaxis of pseudomonas putida toward chlorinated benzoates,” *Appl. Environ. Microb.*, vol. 56, no. 5, pp. 1501–1503, 1990.
- [63] M. Theves, J. Taktikos, V. Zaburdaev, H. Stark, and C. Beta, “A bacterial swimmer with two alternating speeds of propagation,” *Biophys. J.*, vol. 105, no. 8, pp. 1915–1924, 2013.
- [64] M. Hintsche, V. Waljor, R. Großmann, M. J. Kühn, K. M. Thormann, F. Peruani, and C. Beta, “A polar bundle of flagella can drive bacterial swimming by pushing, pulling, or coiling around the cell body,” *Sci. Rep.*, vol. 7, no. 1, p. 16771, 2017.
- [65] M. Mijalkov, A. McDaniel, J. Wehr, and G. Volpe, “Engineering sensorial delay to control phototaxis and emergent collective behaviors,” *Phys. Rev. X*, vol. 6, p. 011008, 2016.
- [66] R. Großmann, F. Peruani, and M. Bär, “Diffusion properties of active particles with directional reversal,” *New Journal of Physics*, vol. 18, no. 4, p. 043009, 2016.
- [67] F. Peruani and L. G. Morelli, “Self-propelled particles with fluctuating speed and direction of motion in two dimensions,” *Phys. Rev. Lett.*, vol. 99, p. 010602, Jul 2007.
- [68] J. Sambrook and D. Russell, *Molecular Cloning: A Laboratory Manual*. Cold Spring Harbor: Cold Spring Harbor Laboratory Press, 2001.
- [69] W. H. Press, S. A. Teukolsky, W. T. Vetterling, and B. P. Flannery, *Numerical recipes – The Art of Scientific Computing*. Cambridge University Press, 3rd ed., 2007.
- [70] H. Haken, *Synergetics: Introduction and Advanced Topics*. Springer, 2004.
- [71] E. Bertin, M. Droz, and G. Grégoire, “Boltzmann and hydrodynamic description for self-propelled particles,” *Phys. Rev. E*, vol. 74, p. 022101, Aug 2006.

- [72] R. Großmann, L. Schimansky-Geier, and P. Romanczuk, “Self-propelled particles with selective attraction-repulsion interaction: from microscopic dynamics to coarse-grained theories,” *New J. Phys.*, vol. 15, no. 8, p. 085014, 2013.
- [73] F. Peruani, “Hydrodynamic equations for flocking models without velocity alignment,” *J. Phys. Soc. Jpn.*, vol. 86, no. 10, p. 101010, 2017.